

Monte Carlo Simulation of Mixed Neutron-Gamma Radiation Fields and Dosimetry Devices

Zur Erlangung des akademischen Grades eines

DOKTOR-INGENIEURS

von der Fakultät für
Elektrotechnik und Informationstechnik
des Karlsruher Instituts für Technologie (KIT)

genehmigte

DISSERTATION

von

M.Sc. Guoqing Zhang
geb. in Dalian, China

Tag der mündlichen Prüfung: 22. Dezember 2011
Hauptreferent: Prof. Dr. Ing. Manfred Urban¹
Korreferent: Prof. Dr. Ing. Uwe Kiencke²

¹Wiederaufarbeitungsanlage Karlsruhe GmbH

²Institut für industrielle Informationstechnik

Author's email: zhang.gq@hotmail.com

Betreuer: Dr. rer. nat. Frank Becker¹
Kobetreuer: Prof. Yiren Xuan²

¹Karlsruher Institut für Technologie - Karlsruhe Institute of Technology

²China Institut für Strahlenschutz - China Institute for Radiation Protection

Erklärung

Ich versichere wahrheitsgemäß, die Dissertation bis auf die dort angegebene Hilfe selbständig angefertigt, alle benutzten Hilfsmittel vollständig und genau angegeben und alles kenntlich gemacht zu haben, was aus Arbeiten anderer und eigenen Veröffentlichungen unverändert oder mit Änderungen entnommen wurde.

Karlsruhe, den 10.10.2011

Acknowledgement

My first words of thanks are for my advisors, Prof. Dr. Manfred Urban, Dr. Frank Becker and Prof. Yiren Xuan. Over the last three years, they have provided me with lots of valuable suggestions and efficient supervisions. I was also benefited a great deal from their visionary views on science and their positive attitudes to work. Without their guidance, support and constant feedback this work would not go this far. Thanks are also to Prof. Dr. Uwe Kiencke for reviewing this thesis as the second examiner.

Furthermore, I would like to extend my thanks to Rick Fritschek from Hochschule Furtwangen University for working together with me at KIT during his bachelor thesis. It was a great pleasure to work with him, and I have learnt a lot from him.

I am also very grateful to Dr. Debora Leone, Christoph Blunck, Dr. Olaf Mazzocchi, Dr. Lars Hegenbart¹, Dr. Bastian Breustedt and Andreas Benzler at INE-ASF² for many very helpful discussions on Monte Carlo calculations and for helping me to solve many other problems. Specially to Dr. Debora Leone for many correction suggestions to improve this thesis.

I extend my appreciation to Annette Schwandner, Melanie Schaller, Isabella Swillus and Christian Naber at the KIT³ - Safety Management (KSM). They allowed me to use their equipments and helped me solving many problems concerning their equipments and software system I have met during the experiments. I really appreciate their patience with answering my thousands of questions, and I would like to apologize for all the disturbs as well.

Thanks also to Klemens Hummelsheim and Ulrich Hesse et al. of the Society for Plant Safety and Reactor (GRS⁴ Garching) for providing the source information of spent fuels inside the Castor V/19.

I would like to present my thanks to Sabine Mayer and Markus Fürstner at the Paul Scherrer Institute. The accurate experimental results were obtained by them with our detectors using their radioactive source and equipments. That is a very important part for me to verify the results of simulations. The cooperation was successful and cheerful.

I also would like to acknowledge the financial support of the "Helmholtz-CSC⁵ Scholarship

¹Present address: Wiederaufarbeitungsanlage Karlsruhe (WAK)

²German: Institut für Nukleare Entsorgung (INE) Abteilung Strahlenschutzforschung (ASF)

³Karlsruhe Institute of Technology

⁴German: SafetyGesellschaft für Anlagen und Reaktorsicherheit

⁵China Scholarship Council

Application” program for making this PhD possible.

Special thanks to my parents. Their love, help and continuous support accompany me throughout the whole time. I couldn’t have done it without them.

Last but not least, I would like to thank Guoyun Cai at the Central Decontamination Department (HDB⁶) for all his help during my stay in Germany. Living and studying in another country is certainly not easy. Without his help things would be much tougher.

⁶German: Hauptabteilung Dekontaminationsbetriebe

Abstract

Monte Carlo methods based on random sampling are widely used in different fields for the capability of solving problems with a large number of coupled degrees of freedom. In this work, Monte Carlo methods are successfully applied for the simulation of the mixed neutron-gamma field in an interim storage facility and neutron dosimeters of different types. Details are discussed in two parts:

In the first part, the method of simulating an interim storage facility loaded with CASTORs⁷ is presented. The size of a CASTOR is rather large (several meters) and the CASTOR wall is very thick (tens of centimeters). Obtaining the results of dose rates outside a CASTOR with reasonable errors costs usually hours or even days. For the simulation of a large amount of CASTORs in an interim storage facility, it needs weeks or even months to finish a calculation. Variance reduction techniques were used to reduce the calculation time and to achieve reasonable relative errors. Source clones were applied to avoid unnecessary repeated calculations. In addition, the simulations were performed on a cluster system. With the calculation techniques discussed above, the efficiencies of calculations can be improved evidently.

In the second part, the methods of simulating the response of neutron dosimeters are presented. An Alnor albedo dosimeter was modelled in MCNP, and it has been simulated in the facility to calculate the calibration factor to get the evaluated response to a Cf-252 source. The angular response of Makrofol detectors to fast neutrons has also been investigated. As a kind of SSNTD⁸, Makrofol can detect fast neutrons by recording the neutron induced heavy charged recoils. To obtain the information of charged recoils, general-purpose Monte Carlo codes were used for transporting incident neutrons. The response of Makrofol to fast neutrons is dependent on several factors. Based on the parameters which affect the track revealing, the formation of visible tracks was determined. For different incident angles of neutrons, the responses were calculated. To correct the track overlapping effect for high track densities, density correction factors are computed with the Monte Carlo method. A computer code has been developed to handle all the calculations with different parameters. To verify the simulation results, experiments were performed.

⁷Casks for Storage and Transport of Radioactive Materials

⁸Solid State Nuclear Track Detector

Contents

Acknowledgement	iii
Abstract	v
1 Introduction	1
1.1 Challenges of Dosimetry in Mixed Neutron-Gamma Fields	2
1.2 Scope of This Work	3
1.2.1 Mixed Neutron-Gamma Field	3
1.2.1.1 Interim Storage Facilities	3
1.2.2 Dosimeters	3
1.2.2.1 Albedo Dosimeter	4
1.2.2.2 SSNTD	4
1.2.3 Goal of This Work	5
2 Fundamentals	7
2.1 External Dosimetry	7
2.1.1 Concepts, Quantities and Units	7
2.1.2 Objective	10
2.2 Monte Carlo Methods	10
2.2.1 Basic Description	11
2.2.2 Random Number	11
2.2.3 Performance	12
2.2.4 Monte Carlo Method in External Dosimetry	12
3 Materials and Methods	15
3.1 Monte Carlo Codes	15
3.1.1 MCNP	16
3.1.2 MCNPX	18
3.1.3 Geant4	19
3.1.4 SRIM	23
3.2 Parallel Computing	24
3.2.1 MPI	24
3.3 Dose Calculation	24
3.4 Radiation Field in an Interim Storage Facility	26
3.4.1 On-site Interim Storage Facility in Philippsburg	26
3.4.2 CASTOR V/19	26
3.4.3 Modelling in MCNP	28
3.4.4 SCC Cluster	29
3.4.5 Compiling MCNP5 1.51	31

3.4.6	Gamma and Neutron Source	32
3.4.7	Weight Windows	32
3.4.8	Surface Source	35
3.5	Dosimeters	36
3.5.1	Albedo TLD Dosimeter	36
3.5.1.1	Dosimeter Geometry	36
3.5.1.2	Simulations	38
3.5.2	SSNTD	40
3.5.2.1	Makrofol	40
3.5.2.2	Track Etching	40
3.5.2.3	Track Formation Mechanisms	41
3.5.2.4	Monte Carlo Simulation	44
3.5.2.5	Experiments	54
4	Results and Discussion	61
4.1	Radiation Field in the Interim Storage Facility	61
4.1.1	Surface Source Spectra	61
4.1.2	Characteristics of the Radiation Field	61
4.1.2.1	Dose Rate Outside a CASTOR	61
4.1.2.2	Distribution of Dose Rates in the Facility	61
4.1.3	Performance of Calculations	68
4.1.3.1	Performance of Different Methods	68
4.1.3.2	Parallel Computing with Surface Sources	68
4.2	Dosimeters	71
4.2.1	Albedo Dosimeter	71
4.2.1.1	Calculated Reaction Rate	71
4.2.1.2	Scattering Effect	72
4.2.1.3	Response in the Interim Storage Facility	75
4.2.2	SSNTD	76
4.2.2.1	Thickness of Etched Layer	76
4.2.2.2	Tracks at Different Angles	77
4.2.2.3	Restricted Energy Loss	79
4.2.2.4	Density Corrections	79
4.2.2.5	Comparison of Monte Carlo Codes	81
4.2.2.6	Angular Response	81
4.2.2.7	Angular Responses of Detectors of Different Shapes	86
5	Conclusions and Perspectives	93
5.1	Presentation of Problems	93
5.2	Solutions	94
5.3	Summary	94
5.4	Perspectives	95
A	MCNP Input Files for CASTOR V/19 and Mesh Geometry	97
A.1	CASTOR V/19 Input File	97
A.2	Mesh Input	99
B	Instruction on Using the SCC Cluster	101
C	Scripts for MCNP5/MCNPX	103

D	MCNP Input File for an Alnor Albedo Dosimeter	105
E	MCNPX Patch for SSNTD	107
F	MCNPX and HTAPE3X Input Files for SSNTD	109
	F.1 MCNPX Input File	109
	F.2 HTAPE3X Input File	110
G	Neutron Physics in Geant4	111
H	Algorithm for Track Density Correction	113
I	SSNTDKIT Manual	115
	I.1 User Interface	115
	I.1.1 Menus	116
	I.1.2 Working Area	116
	I.1.3 Setting Dialog	117
	I.2 Functions	118
	I.2.1 Track Counting	118
	I.2.2 Plotting Round Tracks	118
	I.2.3 Calculation of Density Factors	118
	I.3 Help Information	121
J	Experimental Data and Two-Step ECE Protocol	123
	Bibliography	129
	Publications During my PhD Study at KIT	135
	List of Abbreviations	138

Chapter 1

Introduction

Mixed radiation fields, which comprise different radiation components, are very common in various facilities and sites. According to the International Commission on Radiological Protection (ICRP, 1991) the absorbed dose, as the fundamental dosimetric quantity in radiation protection, is connected to the equivalent dose as the product of the radiation weighting factors and the absorbed dose. Concerning mixed radiation fields each radiation component must be considered separately with their individual weighting factors according to their type and energy. Hence each radiation component with a different weighting factor has to be determined independently. This requires specific dosimeters with the capability to analyse for each important radiation component of the mixed field.

This work contributes to the field of neutrons and accompanying photons, which are penetrating radiations. According to the International Commission on Radiation Units and Measurements (ICRU, 1993), ambient dose equivalent, $H^*(10)$, and personal dose equivalent, $H_p(10)$, (see Section 2.1.1) are recommended to be used for workplace monitoring and individual monitoring in mixed neutron-gamma fields.

Except the tissue equivalent proportional counter (Qashua *et al.*, 2010), neutron and gamma doses are normally measured with different dosimeters. In personnel dosimetry, semiconductor dosimeters, thermoluminescence dosimeters (TLDs), etc. are used to detect gammas, while albedo dosimeters, nuclear track dosimeters, Bonner spheres (Bramblett *et al.*, 1960) and so on are used to measure neutrons.

Considering the complexity of neutron dosimetry (see Section 1.1), neutron dosimeters are calibrated for each radiation field in order to match the neutron spectrum. The relative response to a reference neutron source, e.g. Cf-252, is determined. For different fields, calibration factors can be used to correct for the reading and to obtain the dose equivalent.

For the measurement of the dose equivalent, difficulties arise due to the different responses of dosimeters to radiations. Different measurement conditions need to take the appropriate quality factors (see Section 2.1.1) into account. For neutron personal dosimetry it is difficult to find a detector material which has an energy response to correct for the dose equivalent in the whole energy range of the field. In order to get a satisfactory response, frequently

dosimeters are restricted to a certain neutron energy range. For example, albedo dosimeters detect mainly the body-backscattered thermal neutrons instead of field neutrons while nuclear track detectors measure fast neutrons.

The dosimetry of mixed neutron-photon fields shows frequent problems concerning the measurement/discrimination of dose contribution of different radiation components. To overcome the difficulties of the measurements, numerical simulations with e.g. Monte Carlo codes would allow a detailed analysis of each component of mixed fields with the aim to compensate the lack of the measurement's precision. The simulations can be verified with measurement results of different dosimeters according to their individual response.

This work is focus on such an investigation, where detailed properties of a mixed neutron-gamma field are compared to those of an albedo dosimeter and solid state nuclear track detectors.

1.1 Challenges of Dosimetry in Mixed Neutron-Gamma Fields

Mixed neutron-gamma fields still present a challenge for the external dosimetry, in particular with respect to the determination of the neutron dose. Despite many years of development, neutron dosimeters are not capable of measuring the dose with the same accuracy as for photons. The fact that the interaction of neutrons with matter is more complex than for photons, leads in general to more pronounced energy and angular dependences.

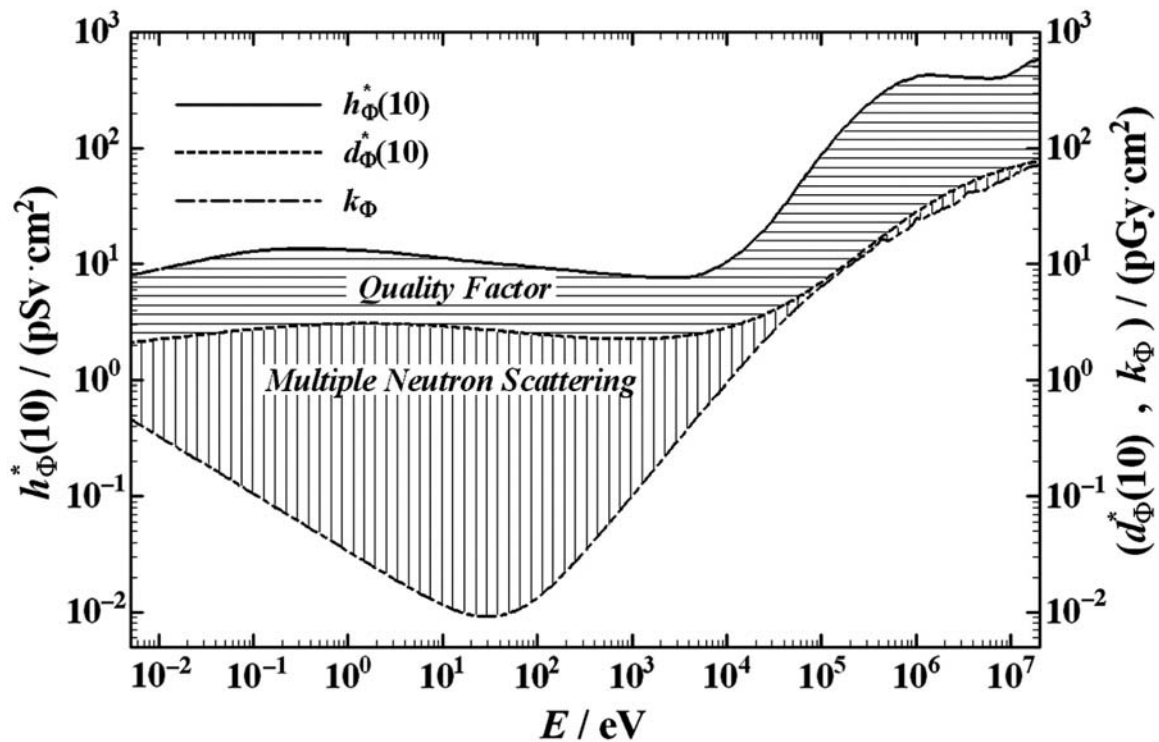


Figure 1.1: Conversion coefficients from neutron fluence to tissue kerma, k_{Φ} , absorbed dose at 10-mm depth in a phantom, d_{Φ}^* and to ambient dose equivalent, h_{Φ}^* , as a function of the energy of incident neutrons (ICRU, 2001).

Neutron dosimeters should be built in such a way that their energy and angular response curve approaches that one of the neutron dose. The complexity of neutron interactions with tissue, dosimeter and ambient materials together with a wide range of the neutron energy (see Figure 1.1) observed at workplaces shows that this approximation is hard to achieve. Figure 1.1 shows that the conversion coefficient from neutron fluence to ambient dose equivalent varies by a factor of about 50 over the entire energy range. However, the strong dose differences depending on the spectral distributions of the neutrons require different calibration factors, which should be determined as accurate as possible.

1.2 Scope of This Work

1.2.1 Mixed Neutron-Gamma Field

In this work, an interim storage facility has been used as an example. With the help of the Monte Carlo method, the flux distributions of neutrons and gammas of the field could be estimated. With fluence to dose conversion coefficients (see Section 3.3), dose rate distributions can be easily obtained. However, for the inhomogeneous neutron-gamma field such as the field in interim storage facilities, normally Monte Carlo simulations are very time-consuming to get reliable results, because it needs to handle complex geometries and radiation sources. The simulation method should be improved to get a better performance.

1.2.1.1 Interim Storage Facilities

In Germany, spent fuels are stored in interim storage facilities before being transported to the final disposal site which is not yet available (Thomauske, 2002). Interim storage facilities are built on site of nuclear power plants. Casks for storage and transport of radioactive materials (CASTORs) loaded with spent fuels from pressurized water reactors or boiling water reactors are placed in the facilities.

For radiation protection purpose, detailed knowledge of the radiation field in the interim storage facilities is important. The Monte Carlo code MCNP5 has been used to calculate the radiation field, spectra and dose rates. Different calculation techniques have been applied to improve the calculation efficiency.

1.2.2 Dosimeters

Neutron personnel dosimetry devices usually detect thermal and fast neutrons, such as albedo dosimeters and track detectors, respectively. Since intermediate-energy neutrons can be moderated down to thermal neutrons, in general dosimeters usually register the corresponding thermal neutron part. The Monte Carlo method has been applied to simulated the response of different dosimeters including albedo dosimeters and photon-insensitive track detectors for neutrons of different energy ranges. An advantage of the Monte Carlo method is that the

complete neutron spectrum can be revealed directly without the indirect way via moderated neutrons.

1.2.2.1 Albedo Dosimeter

Incident neutrons can be moderated and backscattered by the human body. Those neutrons moderated and scattered back are so-called albedo neutrons. Albedo neutron dosimeters, which are worn close to the human body, estimate the dose equivalent in the body by measuring mainly albedo neutrons instead of field neutrons.

Various types of albedo dosimeters have been designed with different structures and materials by researchers (Piesch *et al.*, 1984; Piesch and Burgkhardt, 1985).

The usual procedure to determine calibration factors for a dosimeter is to scale the dosimeter reading as determined in a reference radiation field. But this may lead to unsatisfactory results for mixed neutron-photon radiation fields, if the spectrum of the source (e.g. Cf-252) differs from that of the neutron spectrum in the workplace field. Hence for improved accuracy the knowledge of the radiation field is needed. This can be achieved by measurements and/or simulations. Concerning the measurements the employment of Bonner spheres (Bramblett *et al.*, 1960) yields an almost isotropic response and covers a neutron energy range from thermal to tens of MeV. However, the measurement can be very time-consuming and in some cases difficult or not possible. In this case Monte Carlo simulations could help to determine the radiation field in detail and to establish a correct correlation between the response of dosimeters in a given radiation field. Key measurements to validate the simulation would reduce the experimental effort to a minimum.

An Alnor albedo dosimeter (see Section 3.5.1.1) has been modelled and simulated in the neutron field of an interim storage facility. The relative response of the dosimeter to a Cf-252 reference field was also calculated to get the calibration factor (Piesch and Burgkhardt, 1988a).

1.2.2.2 SSNTD

In 1958, it was first discovered that the paths of charged particles can be revealed after treatment of a chemical reagent (Young, 1998). Based on the phenomenon, solid state nuclear track detectors (SSNTDs) have been developed to detect heavy charged particles and particles which can produce charged particles in the material. Nowadays, SSNTDs are widely applied in many fields such as dosimetry, fission and nuclear physics, space physics, cosmic rays, particle accelerators, reactors.

Many materials, such as inorganic crystals, glasses and plastics, have been applied to detect heavy charged particles, fission fragments and fast neutrons (see ref. (Kalsi *et al.*, 2011) for more materials and applications). Among polycarbonate detectors, CR-39 and Makrofol are very promising materials to measure in mixed radiation field because they are insensitive to photons and can be of small size.

An etching procedure can be applied to reveal latent tracks left by particles via the rapider

dissolution of the track core than the bulk material. During the past decades, several etching methods and procedures were proposed by different scientists and researchers. Based on the different etching rates along track pits and bulk material, chemical etching (CE) was the first method used for fixing and enlarging latent tracks. Later on, electrochemical etching (ECE) was introduced by Tommasino (Tommasino, 1970). The combination of pre-etching and ECE was investigated by Hassib *et al.* (Hassib, 1978; Hassib *et al.*, 1979) to reduce the background and improve the reproducibility. The optimization of the ECE was investigated by El-Fiki *et al.* (El-Fiki *et al.*, 1986). A two-step ECE procedure was recommended by Tommasino (Tommasino *et al.*, 1984) for CR-39 to improve the energy response to neutrons. After that, the two-step ECE procedure has been also successfully applied for Makrofol (Piesch *et al.*, 1991).

Many theories were developed to describe the mechanisms of track formation in materials (Fleischer *et al.*, 2008). For example, primary ionization and restricted energy loss (REL) are well known by researchers. Using different models, the formation of etchable tracks is determined by parameters such as charge, mass and energy of incident particles.

At the Karlsruhe Institute of Technology (KIT) Makrofol detectors are used for radon and fast neutron monitoring (Urban, 1986; Józefowicz and Piesch, 1990). An optimized two-step ECE procedure (see Section 3.5.2.5) is applied to reveal latent tracks generated by charged particles. An auto-analyzing system (see Section 3.5.2.5) has been applied to count the number of tracks.

The Monte Carlo method is very helpful for the investigation of SSNTDs. Through the Monte Carlo simulation, the responses of SSTNDs to different radiation sources in various scenarios can be predicted. This could help to improve the response of dosimeters.

As a result of the earlier application of CR-39, many simulation works have been done. Using general-purpose Monte Carlo codes (Hermsdorf *et al.*, 1999; Zaki-Dizaji *et al.*, 2008) or own developed program (Khan *et al.*, 2001), the response of CR-39 to different sources was simulated.

Unlike CR-39, protons do not form visible tracks in Makrofol, and the registration of α particles is limited to a small energy range (Józefowicz and Piesch, 1990), detailed experiences and data are not available for Makrofol.

In this work, based on the REL model, the response of Makrofol detectors to Cf-252 neutrons is calculated using energy thresholds and critical angles. The information of neutron induced heavy recoils in Makrofol is obtained by the transport of neutrons in detectors with the general purpose Monte Carlo codes MCNPX (Pelowitz, 2008) and Geant4 (Agostinelli *et al.*, 2003). The simulations were verified with experiments.

1.2.3 Goal of This Work

This work is dedicated to investigate dosimeters in mixed neutron-gamma radiation fields with the help of Monte Carlo methods. Exemplary, the simulations of the radiation field in

an interim storage facility, a proper calibration of an albedo dosimeter in the corresponding radiation field, as well as simulations and experiments of the response of Makrofol detectors to fast neutrons are expected to be accomplished in this work. Following information should be provided in this work:

- The spectrum and dose rate distribution in the storage facility, a method to improve the simulation efficiency of the complex mixed neutron-gamma fields of the facility
- To determine an accurate calibration factor for the albedo dosimeter in the mixed neutron-gamma field of the facility
- A calculation/simulation method which can be used to simulate the response of Makrofol detectors to fast neutrons

Chapter 2

Fundamentals

Basic knowledges of external dosimetry and the Monte Carlo method are presented in this chapter. Relevant concepts, theories and methods could help to get a better understanding of this work.

2.1 External Dosimetry

Radiation dosimetry focuses on the determination of personal and ambient dosimetry caused by ionizing radiations. The value of the dose can be used to assess the risk of the exposure. Generally, exposures can result from radioactive sources (or other radiation sources) outside the organism, or radioactive materials inside the organism. External dosimetry is aimed on external exposures.

2.1.1 Concepts, Quantities and Units

In the external dosimetry many quantities are defined for protection or measurement purpose by the International Commission on Radiation Units and Measurements (ICRU). Important quantities and units, which are used or related to this work, are presented in the following according to ICRU reports (ICRU, 1993, 1998).

Activity*

The activity, A , of an amount of a radionuclide in a particular energy state at a given time, is the quotient of dN by dt , where dN is the number of nuclear transformations from that energy state in the time interval dt , thus

$$A = \frac{dN}{dt} \quad (2.1)$$

The unit is s^{-1} and the special name is becquerel (Bq).

*The original text can be found in ICRU reports (ICRU, 1993, 1998)

Fluence*

The fluence, Φ , is the quotient of dN by da , where dN is the number of particles incident upon a small sphere of cross-sectional area da , thus

$$\Phi = \frac{dN}{da} \quad (2.2)$$

The unit of the particle fluence is cm^{-2} .

In dosimetric calculations, fluence is frequently expressed in terms of the lengths of the particle trajectories. It can be shown that Φ is given by

$$\Phi = \frac{dl}{dV} \quad (2.3)$$

where dl is the sum of the particle trajectory lengths in the volume dV .

Absorbed Dose*

The absorbed dose, D , is defined as the quotient of mean energy, $d\bar{\epsilon}$, imparted by ionizing radiation in a volume element of mass dm , that is

$$D = \frac{d\bar{\epsilon}}{dm} \quad (2.4)$$

The unit is $J \cdot kg^{-1}$ and the special name is gray (Gy).

Linear Energy Transfer*

The linear energy transfer or restricted linear electronic stopping power, L_{Δ} , of a material, for charged particles, is the quotient of dE_{Δ} by dl , where dE_{Δ} is the energy lost by a charged particle due to electronic collisions in traversing a distance dl , minus the sum of the kinetic energies of all the electrons released with kinetic energies in excess of Δ , thus

$$L_{\Delta} = \frac{dE_{\Delta}}{dl} \quad (2.5)$$

The unit is $J \cdot kg^{-1}$.

Quality Factor The quality factor, Q , is used for weighting the relative biological effectiveness of the radiation. Q is defined as a function of the unrestricted linear energy transfer L_{∞} .

Dose Equivalent*

The dose equivalent, H , is the product of Q and D at a point in tissue, where D is the

*The original text can be found in ICRU reports (ICRU, 1993, 1998)

absorbed dose and Q is the quality factor at that point, thus

$$H = Q \cdot D \quad (2.6)$$

The unit is $J \cdot kg^{-1}$ and the special name is sievert (Sv).

ICRU¹ Sphere

A sphere of 30 cm diameter made of tissue equivalent material with a density of 1 g/cm^3 and a mass composition of 76.2% oxygen, 11.1% carbon, 10.1% hydrogen and 2.6% nitrogen is used as a reference phantom in defining dose equivalent quantities.

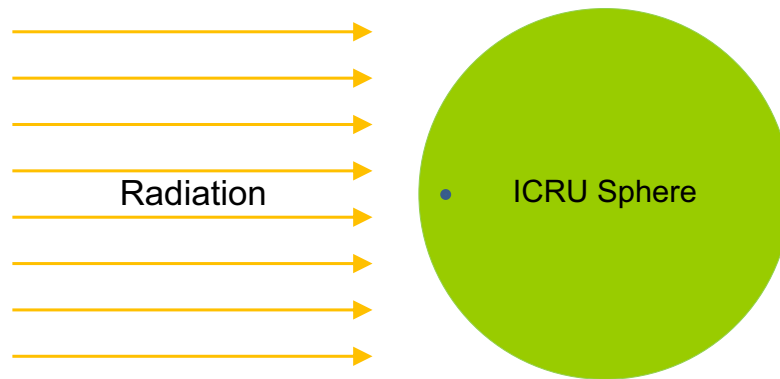


Figure 2.1: Ambient dose equivalent, $H^*(d)$. Blue point: point of measurement at depth d from the surface of the ICRU sphere.

Ambient Dose Equivalent*

The ambient dose equivalent, $H^*(d)$, at a point in a radiation field, is the dose equivalent that would be produced by the corresponding expanded and aligned field, in the ICRU sphere at a depth, d , on the radius opposing the direction of the aligned field

The unit is $J \cdot kg^{-1}$ and the special name is sievert (Sv).

The recommended reference depths are 10 mm for strongly penetrating radiations and 0.07 mm for weakly penetrating radiations, respectively. The quantities denote $H^*(10)$ and $H^*(0.07)$.

Ambient Dose Equivalent Rate*

The ambient dose equivalent rate, $\dot{H}^*(d)$, is the quotient of $dH^*(d)$ by dt , where $dH^*(d)$ is the increment of ambient dose equivalent in the time interval dt , thus

$$\dot{H}^*(d) = \frac{dH^*(d)}{dt} \quad (2.7)$$

The unit is $J \cdot kg^{-1} \cdot s^{-1}$ and the special name is sievert per second ($\text{Sv} \cdot \text{s}^{-1}$).

¹International Commission on Radiation Units and Measurements

*The original text can be found in ICRU reports (ICRU, 1993, 1998)

Personal Dose Equivalent*

The personal dose equivalent, $H_p(d)$, is the dose equivalent in soft tissue, at an appropriate depth, d , below a specified point on the body.

The unit is $J \cdot kg^{-1}$ and the special name is sievert (Sv).

Similar to the ambient dose equivalent, $d = 10$ mm is used for strongly penetrating radiations, and $d = 0.07$ mm for weakly penetrating radiations.

Personal Dose Equivalent Rate*

The personal dose equivalent rate, $\dot{H}_p(d)$, is the quotient of $dH_p(d)$ by dt , where $dH_p(d)$ is the increment of ambient dose equivalent in the time interval dt , thus

$$\dot{H}_p(d) = \frac{dH_p(d)}{dt} \quad (2.8)$$

The unit is $J \cdot kg^{-1} \cdot s^{-1}$ and the special name is sievert per second ($Sv \cdot s^{-1}$).

2.1.2 Objective

There are three fundamental principles of radiation protection recommended by ICRP² (ICRP, 1971, 1991, 2007), namely:

- Justification of practices
- Optimization of protection
- Dose limits to individuals

”The objective of external dosimetry is the assessment of personnel exposure to external radiation in terms of the operational and protection dosimetric quantities used to measure and limit personnel dose” (Rathbone, 2011).

2.2 Monte Carlo Methods

Monte Carlo methods are computational algorithms based on random sampling to get results. In 1940s, Monte Carlo method was first introduced for the nuclear weapon project, Manhattan-Project (Badash, 2011). Now Monte Carlo methods are widely used in many fields such as nuclear physics, dosimetry, economics, chemistry, telecommunications, computer games and so on. With the developing of computer techniques, Monte Carlo methods become more and more popular in many fields of applications to calculate problems which can be hardly solved with classic analytic methods.

*The original text can be found in ICRU reports (ICRU, 1993, 1998)

²International Commission on Radiological Protection

2.2.1 Basic Description

If a problem is to calculate the mathematical expectation of a stochastic variable, the probability of a random event or other relevant quantities, the result can be obtained by random experiments. Each experiment gives a sample of the problem. The average value of all events will be an approximate solution of the problem.

Many problems can be simplified with a suitable probabilistic model. For example, particles interact with matter. The reaction type between the projectile particle and target atom follows a probabilistic distribution. So, the interactions of particles can be sampled with a set of random reactions based on the distribution.

To get an accurate approximation of the solution, the number of random experiments should be large enough. Therefore, the work cannot be done manually as the Buffon's Needle (Reese, 2011) in most cases. The advent of the computer provides a good way to perform Monte Carlo simulations, and a large amount of random experiments can be done automatically by computers with the help of random number generators.

2.2.2 Random Number

Random numbers are essential in Monte Carlo simulations, because quantities are sampled with random numbers according to their probability distribution.

Normally, the random sequence used in Monte Carlo simulations is sampled from the uniform distribution in $[0, 1]$, whose probability density function is:

$$f(x) = \begin{cases} 1 & 0 \leq x \leq 1 \\ 0 & \textit{otherwise} \end{cases} \quad (2.9)$$

The distribution function is:

$$F(x) = \int_{-\infty}^x f(x)dx \begin{cases} 0 & x < 0 \\ x & 0 \leq x \leq 1 \\ 1 & x > 1 \end{cases} \quad (2.10)$$

In computers, the sequence of random numbers is generated with the random number generator, which namely is an algorithm. Given a set of initial values, the generator produces the sequence of random numbers. Since the whole sequence is determined by the initial values, it is not a set of real random numbers but an approximation. Therefore, the random number generated by the algorithm is normally called as pseudo-random number, and the algorithm is called pseudo-random number generator.

A good pseudo-random number generator should have the following features (Pang, 2006):

- Uniform distribution. This is essential, otherwise the sequence of random numbers is not qualified.

- Best randomness. The correlation among all numbers should be very small to approximate the real random numbers.
- Long period. A Monte Carlo calculation normally needs a large number of unrepeated random numbers. The random number sequence should not repeat in a simulation.
- Run very fast. The algorithm is called very frequently in a calculation. A low speed algorithm would seriously slow down the calculation.

Many pseudo-random number generators are available. For example, the open source Mersenne Twister generator is a very well-known algorithm. It is developed in 1997 by Makoto Matsumoto and Takuji Nishimura (Matsumoto and Nishimura, 1998), has a period of $2^{19937} - 1$ (about 4×10^{6001}), and runs faster than many other generators (Wagner, 2011).

2.2.3 Performance

The figure of merit (FOM, see Equation 2.11) is usually used to measure the calculation efficiency of Monte Carlo simulations. The larger value of the FOM indicates the better performance of a calculation.

$$FOM = \frac{1}{R^2 T} \quad (2.11)$$

where R is the relative error of the calculated value and T is the calculation time.

In a Monte Carlo simulation, R^2 is approximately proportional to the inverse of the number of source events while T is proportional to the number of source events. Therefore, the product of R^2 and T should be approximately constant in a simulation with different number of source events as well as the FOM. Therefore, FOM can be used to measure the performance of different calculation methods and programs.

2.2.4 Monte Carlo Method in External Dosimetry

The Monte Carlo method is a very useful tool in the external dosimetry. Unlike the analytical method, the Monte Carlo method can make a more realistic approximation of problems in both physics and geometries. All parameters, which affect the results, can be included in the calculation.

In the external dosimetry, the Monte Carlo method can be applied for different applications, such as:

- Calculating dose distribution. For a specific problem, the distribution of dose rate can be calculated with simulations.
- Estimating personnel dose. The dose incurred by a worker can be estimated before an operation.

- Simulating the response of dosimeters. Every dosimeter shows a characteristic response to different sources. For example, the angular and energy response of a dosimeter to a source can be simulated with Monte Carlo codes.
- Designing new dosimetry devices. With the Monte Carlo method, various structures and materials can be tested without actually constructing a dosimeter; time and costs can be saved. The simulations could give the information if a dosimeter is suited in a certain radiation field. Furthermore, optimized dosimeters can be designed.

In the past, series of measurements were performed to investigate the dosimeter while simulations can reduce the effort to "key experiments". For example, the response of albedo dosimeters in an interim storage facility, which was determined with experiments, now can be done with Monte Carlo simulations.

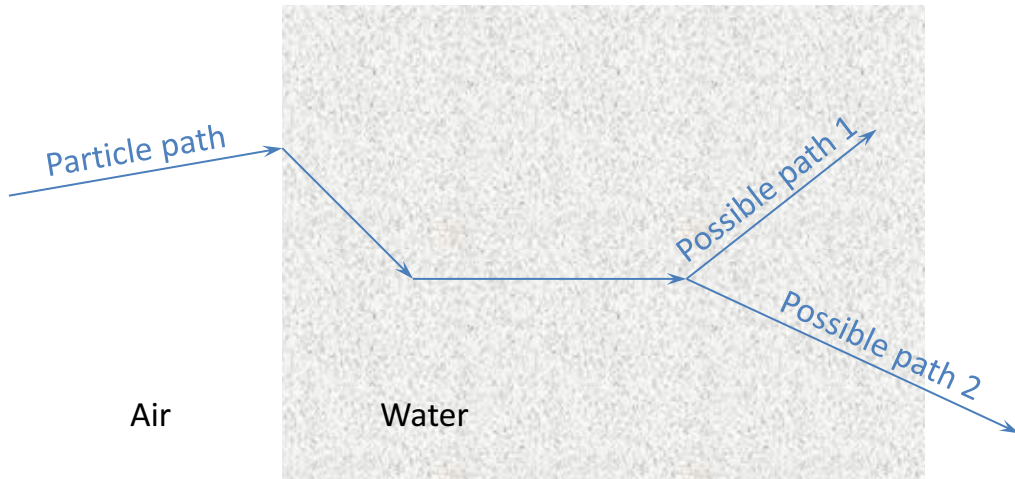


Figure 2.2: Transport of particles in matter with two possible paths.

In order to carry out a Monte Carlo simulation, following steps need to be done:

1. Modelling the geometry of the system. All information of the geometry and materials which affect the results should be described in detail or with appropriate simplifications.
2. Adding physics processes. Different problems and particles need different physics. Correct physics processes are necessary to get reliable results.
3. Defining source. The information of the source including direction, position and energy should be assigned.
4. Retrieving information. Quantities of interest should be extracted from a calculation.

Based on the information given above, Monte Carlo codes perform the transport of source particles and secondary particles until they are "killed" by interactions, have an energy below a limit or leave the geometry of the system (see Figure 2.2).

Chapter 3

Materials and Methods

Monte Carlo Methods have been applied to simulate the radiation field in an interim storage building loaded with CASTORs which are filled with spent fuels, the calibration of an albedo dosimeters, and the response of Makrofol nuclear track detectors.

Information related to this work, which includes data, methods and tools will be described in detail in this chapter.

3.1 Monte Carlo Codes

In the fields of nuclear and particle physics several general purpose Monte Carlo codes have been developed. Hundreds of people have spent tens of years to work on it. As a result of their fruitful works, several excellent Monte Carlo codes are available to users working in different fields.

For example, the following Monte Carlo codes are well-known in the field of nuclear and particle physics:

MCNP – A General Monte Carlo N-Particle Transport Code developed at LANL¹

MCNPX – An extended version of MCNP developed also at LANL

Geant4 – A toolkit for the simulation of the passage of particles through matter, developed by the Geant4 collaboration

SRIM – A collection of software packages which calculate the features of the transport of ions in matter

FLUKA – A general purpose tool for calculations of particle transport and interactions with matter, developed at INFN² and CERN³

¹Los Alamos National Laboratory

²Istituto Nazionale di Fisica Nucleare - National Institute for Nuclear Physics

³Conseil Européen pour la Recherche Nucléaire - European Organization for Nuclear Research

PENELOPE – A Monte Carlo code for coupled transport of photons and electrons for a wide energy range, from a few hundred eV to about 1 GeV (Salvat *et al.*, 2008)

EGS – A simulation code for coupled transport of electrons and photons, developed at SLAC⁴

EGSnrc – An extended and improved version of the EGS4 package, developed at NRC⁵

BEAMnrc – A Monte Carlo code system for modelling radiotherapy sources, developed at NRC

Among the Monte Carlo codes, only those related to this work, namely MCNP(X), Geant4 and SRIM, will be described in detail in this section.

3.1.1 MCNP

MCNP stands for Monte Carlo N-Particle code which is a general-purpose Monte Carlo code that can be used for neutron, photon, electron, or coupled neutron/photon/electron transport. The latest available version of MCNP in early 2010 is MCNP5 1.51, which can be obtained from the Radiation Safety Information Computational Center (RSICC). According to the introduction on its homepage (LANL, 2011), MCNP's "specific areas of application include, but are not limited to, radiation protection and dosimetry, radiation shielding, radiography, medical physics, nuclear criticality safety, detector design and analysis, nuclear oil well logging, accelerator target design, fission and fusion reactor design, decontamination and decommissioning."

Taking advantage of the powerful ability to process geometries, MCNP can simulate very complex systems. In MCNP, cells are bounded by surfaces, which can be planes, spheres, cylinders, cones, hyperboloid, circular torus and so on. A complex geometry can be split into many small parts with different combinations of surfaces. To help users setting up the geometry correctly, MCNP has integrated a plotter, which can plot the geometry in a 2-D view. One of the plotter functions is to detect geometry errors. When overlapping cells or gaps between cells are found, they will be displayed in dotted lines. A software called MCNP Visual Editor is available to plot the geometry in an easy way, and it supports 3-D views.

MCNP contains many useful built-in tallies, which specify what type of information the user wants to gain from the Monte Carlo calculation. Normally, a tally could be surface current, surface fluence, volume fluence (track length), point and ring fluence detectors, particle heating, fission heating, pulse height and so on. The new version of MCNP also supports mesh tallies, which can give the spacial distribution of different tally results in a designated zone.

Compared to other Monte Carlo codes, an advantageous features of MCNP is that no programming skill is required. To perform a simulation, only a rather simple input file, which

⁴Stanford Linear Accelerator Center

⁵National Research Council Canada

consists of MCNP-style predefined commands, is needed. From the input file, MCNP can read the information of sources, geometry, tallies, etc. to carry out a simulation.

As a general-purpose Monte Carlo code, MCNP has integrated methods to define radiation sources. Generally, three types of sources are available in MCNP, which are general source, criticality source, and surface source. With the general source, sources of different energy spectra, shapes, directions, positions, type of particles and so on can be defined. The criticality source is dedicated for criticality calculations. The surface source can read the source information from an external file, which is produced by a previous calculation of MCNP, and use it as a source on relevant surfaces.

In MCNP an input option is called a card. Based on their different functions, input cards are placed in the following four card blocks:

Message Block is an optional block, which can be used to set execution line parameters or environment variables for MCNP.

Cell Card Block constructs the geometry of a physical system on the basis of surfaces defined in the surface card block.

Surface Card Block defines surfaces used in a problem.

Data Card Block sets nearly all other information of a problem except the geometry. Basically, the information of materials, source, tallies, number of histories are needed. In addition, physics parameters, cut energies, cell weights and other specific options can be assigned as needed.

In a MCNP input file, two neighboring blocks are delimited by a blank line. The order of blocks should not be out of sequence. Otherwise, the input file cannot be recognized by MCNP.

Normally, a binary file (default name RUNTPE) and a text file (default name OUTP) will be created after a simulation is finished. The binary file contains the runtime information while the text file contains the simulation results and other useful information.

MCNP allows users to restart a previously terminated job from where it stopped. The status of a calculation can be retrieved from the RUNTPE file, and new calculation conditions can be given in the continue-run input file, which has the CONTINUE keyword in it.

A rich collection of variance reduction techniques are available in MCNP (Shultis and Faw, 2010; Booth, 1985). For example:

Russian roulette and splitting are basic variance reduction techniques. MCNP allows to use Russian roulette and splitting in geometry and energy or both. For example, cells are assigned with different importances. When a particle travels from a cell of lower importance to a cell of higher importance, it will be split to several particles, assigned new weights totalling the original weights. If a particle moves in the opposite direction, Russian roulette will be played to increase the weight of the particle or to kill

the particle with a certain probability, which is related to the ratio of the weights of the two cells. Thereby, MCNP spends more time sampling in important parts of geometry or energy than in the unimportant ones.

Weight windows are similar to Russian roulette and splitting, but more functional. In each cell (or energy region), a lower weight bound and an upper bound are specified (weight window). If a particle entering a cell or created in the cell has a weight above the upper bound, the particle will be split to two or more particles with weights within the weight window. If the weight of a particle is below the lower bound, Russian roulette is used to keep the weight of the particle in the range of the weight window. In MCNP, weight windows can be automatically generated with the weight-window generator.

Source biasing applies a normalized weight distribution to the source. This technique can set source particles with enhanced weights, preferred moving direction, energies and so on. Neglecting the calculation parts which do not contribute to the result of interest, the efficiency of simulation would be increased.

Point and ring detectors in MCNP use partially the deterministic method to calculate the contribution of each step to the tally. A particle can contribute to a tally, even if it does not reach the detector region.

MCNP fully supports parallel computing, which can be based on the Parallel Virtual Machine (PVM) or the Message Passing Interface (MPI), and runs on Windows, Linux and UNIX systems. With the help of parallel implementations, MCNP can also run on cluster systems.

In this work, MCNP5 1.51 has been used to calculate the radiation field of an on-site interim storage facility loaded with CASTORs.

3.1.2 MCNPX

MCNPX is the abbreviation for Monte Carlo N-Particle eXtended, which is a superset of MCNP. MCNPX was first originated from the merge of MCNP4B and LAHET 2.8 (Prael and Lichtenstein, 1989). After that, physics models and new capabilities have been adding to MCNPX. Now, MCNPX 2.6.0 can transport 34 particle types (nucleons and light ions) and more than 2000 heavy ions at nearly all energies by mixing and matching of nuclear data table and model physics.

As an extension of MCNP, MCNPX is compatible with MCNP5. The input file formats are basically the same; only a few input cards have different names. Other than particles which MCNP5 does not support, an input file is valid for both MCNP5 and MCNPX in most cases.

MCNPX 2.6.0 and MCNP5 1.51 are released together. They share the same libraries which include standard neutron, photo-atomic, photo-nuclear and electron data.

Released together with MCNPX, the HTAPE3X program can process the medium- and high-energy collision data written in a history file by MCNPX. Similar to MCNPX, HTAPE3X needs an input file of its own. Information including flux, track length, recoil energy and so on can be retrieved.

In this work, MCNPX has been used to simulate neutrons interacting with Makrofol detectors and to record the information of heavy recoils in a file. HTAPE3X reads the file generated by MCNPX and retrieves the information of interest for further analysis.

3.1.3 Geant4

Geant4, which stands for GEometry ANd Tracking version 4, is a toolkit for the simulation of the passage of particles through matter. Unlike the other Monte Carlo codes, Geant4 is not an executable program but a set of C++ class libraries which contain predefined C++ classes. To make a simulation with Geant4, users have to write their own C++ codes and compile them to generate an executable file.

The objective of Geant4 was to write a detector simulation program which can meet the requirements of high-energy physics experiments. With the cooperation of physicist programmers and software engineers, Geant4 becomes a powerful Monte Carlo tool which far exceeds the original goal. Now, Geant4 is widely used in many fields, such as:

- Space science and astrophysics
- Medical physics, nuclear medicine
- Radiation protection
- Dosimetry
- Accelerator physics
- Detector design
- Food irradiation
- Security, etc.

A large international collaboration of researchers from institutes in Europe, Japan, Canada and the United States, is contributing to the code and expanding its functionalities. More and more people are participating in developing and employing Geant4.

Written in C++, Geant4 takes advantage of object-oriented technology to construct the whole code system. As can be seen from Figure 3.1, Geant4 consists of a class tree. Each class is in charge of a task like constructing geometry, defining source, registering physics processes, tracking particles and so on. Different classes are connected to each other through internal interfaces.

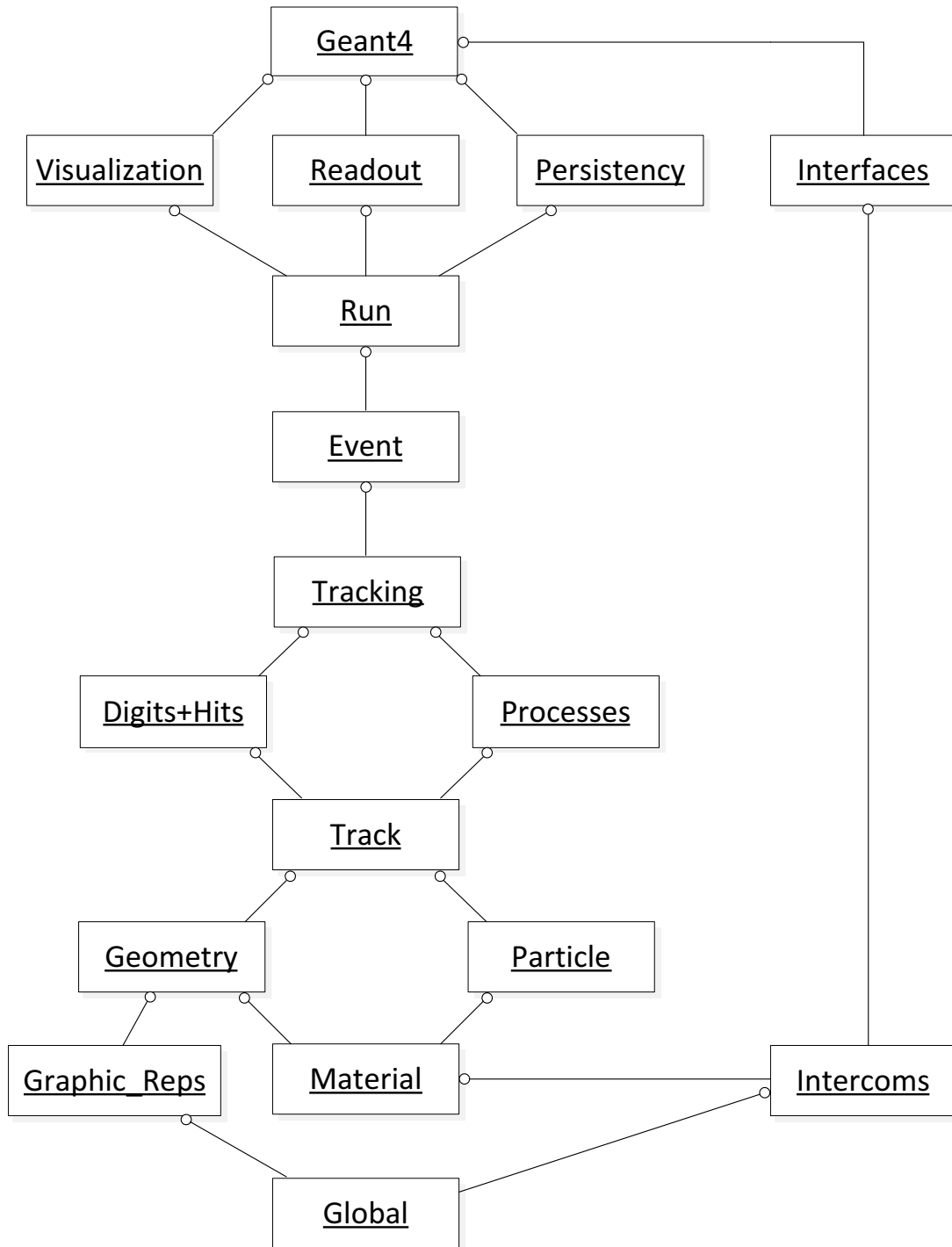


Figure 3.1: Geant4 class categories (Geant4 Collaboration, 2011).

In order to perform a simulation with Geant4, much more work needs to be done than with MCNP(X). Geant4-style C++ codes, which include a main function and subclasses of three mandatory interface classes, namely `G4VUserDetectorConstruction`, `G4VUserPhysicsList`, `G4VUserPrimaryGeneratorAction`, have to be reimplemented. The `G4VUserDetectorConstruction` class defines the problem geometry, material, position, magnetic field and so on; the `G4VUserPhysicsList` class registers all particle types and physics processes related to the problem, and assigns cross section data and models for each process; the `G4VUserPrimaryGeneratorAction` class produces source particles with assigned energy, type, direction, position, weights, etc. In the main function, an instance of a `G4RunManager` class is defined. Mandatory classes need to register themselves to the `G4RunManager` class, which initializes all classes and sets calculation conditions and starts a simulation. When the source codes are ready, the user needs to compile them usually with a Geant4-style makefile which is available in the examples in the Geant4 package. After a successful compiling, an executable file will be generated. With the support of Geant4 libraries, the executable program can run on UNIX-like systems, or on a Windows system with a Cygwin Linux-like environment.

Geant4 provides a visualization system, which is based on graphics libraries, such as OpenGL and Qt. The system can visualize geometries, particle trajectories, and volume overlapping errors in 2D or 3D view. Derived classes of relevant interface classes can be implemented in the main function to make the visualization. In addition, there are also some other plotting applications available, such as HepRApp or DAWN.

To make a simulation with Geant4, a user needs not only necessary physics background but also basic knowledge of C++. Physics processes should be added manually through Geant4-based C++ programming. Therefore the user should be fully aware of which processes should be included. Although Geant4 needs more effort compared to MCNP(X), it provides considerable flexibility. Processes, cross section data and physics models can be mixed and matched with each other as needed for different problems. The information of interest can be retrieved according to the needs through integrated interfaces.

A Geant4 application, which is implemented with mandatory classes, does not give standard information produced in a simulation. All information of interest should be extracted manually. Fortunately, volumes can be set "sensitive" if a detector class is assigned in Geant4. User defined detector or built-in detector can be applied. If a user defined detector is used, the information of interest needs to be extract manually. The built-in detector allows using Geant4 primitive scores, which are built-in classes for record different physical quantities, to retrieve useful information, like number of particles crossing a surface, average track length over a cell, average fluence over a surface, total energy deposition in a cell, etc.

Normally, predefined detector classes can be used to provide standard informations. To get more information or retrieve data in a different way, following classes and functions can be employed:

- `G4UserRunAction`

- BeginOfRunAction method is invoked at the beginning of a run
- EndOfRunAction method is invoked at the end of a run
- For example, they can be used to book or store histograms at the beginning or the end of a run (certain number of particles), respectively
- G4UserEventAction
 - BeginOfEventAction method is invoked at the beginning of a particle event
 - EndOfEventAction method is invoked at the end of a particle event
 - For example, one can select information to be stored at the beginning of an event, and process the information at the end of an event
- G4UserStackingAction
 - ClassifyNewTrack method is invoked whenever a new particle track object is pushed onto a stack
 - PrepareNewEvent method is invoked at the beginning of each event before calling BeginOfRunAction method of G4UserEventAction class
 - For example, they can be used to define the priority of a track or to stop the transport of a track
- G4UserTrackingAction
 - PreUserTrackingAction method is invoked at the beginning of each track
 - PostUserTrackingAction method is invoked at the end of each track
 - For example, they can be used to decide if a trajectory should be stored
- G4UserSteppingAction
 - UserSteppingAction method is invoked at the end of a particle track step
 - For example, it can be used to retrieve the energy deposition between two collision points

By applying the member methods of relevant interface classes, almost all information of a simulation, such as energy, charge, position, direction, mass of a particle, and other quantities related to the problem, can be obtained with internal pointers. Based on the data extracted, users can create their own tallies and outputs.

Furthermore, Geant4 can be installed on Windows with Microsoft Visual C++ compiler and a Cygwin environment, on Linux and Mac OS X with a gcc compiler. Interfaces based on the Task Oriented Parallel C/C++ (TOP-C), the DIstributed ANalysis Environment (DIANE) and the MPI are provided for parallel computing. Only a few changes need to be

made in the main function to parallelize a Geant4 application. The interface classes will handle the communications in the background.

In this work, Geant4 has been used as an alternative code to simulate neutrons interacting with Makrofol detectors.

3.1.4 SRIM

SRIM (the Stopping and Range of Ions in Matter) is a group of software packages which calculate the interaction of ions with matter (Ziegler, 2011).



Figure 3.2: SRIM user interface.

Functions of the SRIM package include mainly three parts:

”**Stopping Range Tables**” calculates stopping powers and ranges of particles in different targets. Users can define ion type, target material and energy range for the calculation (see Figure 3.2). A table covering the energy range will be given in a new window. The results are based on the interpolation of experimental data.

”**TRIM Calculation**” (Transport of Ions in Matter) is the most comprehensive program in the SRIM package. On the basis of Monte Carlo simulation, TRIM can simulate ions travelling in complex targets. Compound materials and up to eight layers are supported.

The final 3D distribution of ions and all process associated with the ion's energy loss, such as target damage, sputtering, ionization and photon production can be simulated.

"Experimental Stopping Powers" plots experimental stopping powers for ions in elemental targets.

In this work Stopping Range Tables have been used to calculate the restricted energy loss (see Section 3.5.2.3) and the range of neutron induced heavy recoils in Makrofol for SSNTD simulations.

3.2 Parallel Computing

Scientific calculations are normally very time-consuming to get accurate results. With the developing of computer technology, multi-core or multi-processor computers are becoming more and more popular. If the processors cannot all be used for calculation, it is not only a wasting of computer resource, but also results in a low performance. Parallel computing is a way to split a calculation to several parts running on different processors or computers at the same time. Since each processor is only in charge of one piece of the work, the performance could be improved significantly.

3.2.1 MPI

Parallel computing needs the supports of both hardware and software. Processors and computers need to communicate with each other to distribute and to gather calculation parts. Both Message Passing Interface (MPI) and Parallel Virtual Machine (PVM) provide a standard way for the communication. There are many implementations and free libraries available.

Since MCNP(X) and Geant4 support MPI, and MPI libraries are already installed on the SCC cluster (see Section 3.4.4), MPI has been chosen in this work for parallel computing.

3.3 Dose Calculation

In the field of dosimetry, the dose equivalent is a very important quantity either for area or individual monitoring. The Monte Carlo transport cannot calculate the dose equivalent directly. The way to calculate the dose equivalent is first to calculate the fluence, then to multiply it with a dose function, namely fluence to dose conversion factors. The dose function is given as discrete values of energy and corresponding factor. A continuous energy function can be obtained with an interpolation of the discrete values.

To calculate the ambient dose equivalent of photons and neutrons, the conversion factors in Table 3.1 and Table 3.2 have been used, respectively. More conversion factors can be found in ref. (ICRP, 1997).

Table 3.1: Fluence to Dose Conversion Factors for Photons (ICRP, 1997).

Energy (MeV)	Factor (pSv cm ²)	Energy (MeV)	Factor (pSv cm ²)
0.01	0.061	0.5	2.93
0.015	0.83	0.6	3.44
0.02	1.05	0.8	4.38
0.03	0.81	1	5.20
0.04	0.64	1.5	6.90
0.05	0.55	2	8.60
0.06	0.51	3	11.1
0.08	0.53	4	13.4
0.1	0.61	5	15.5
0.15	0.89	6	17.6
0.2	1.20	8	21.6
0.3	1.80	10	25.6
0.4	2.38		

Table 3.2: Fluence to Dose Conversion Factors for Neutrons (ICRP, 1997).

Energy (MeV)	Factor (pSv cm ²)	Energy (MeV)	Factor (pSv cm ²)
1.00e-9	6.60	7.00e-1	375
1.00e-8	9.00	9.00e-1	400
2.53e-8	10.6	1.00e0	416
1.00e-7	12.9	1.20e0	425
2.00e-7	13.5	2.00e0	420
5.00e-7	13.6	3.00e0	412
1.00e-6	13.3	4.00e0	408
2.00e-6	12.9	5.00e0	405
5.00e-6	12.0	6.00e0	400
1.00e-5	11.3	7.00e0	405
2.00e-5	10.6	8.00e0	409
5.00e-5	9.90	9.00e0	420
1.00e-4	9.40	1.00e1	440
2.00e-4	8.90	1.20e1	480
5.00e-4	8.30	1.40e1	520
1.00e-3	7.90	1.50e1	540
2.00e-3	7.70	1.60e1	555
5.00e-3	8.00	1.80e1	570
1.00e-2	10.5	2.00e1	600
2.00e-2	16.6	3.00e1	515
3.00e-2	23.7	5.00e1	400
5.00e-2	41.1	7.50e1	330
7.00e-2	60.0	1.00e2	285
1.00e-1	88.0	1.25e2	260
1.50e-1	132	1.50e2	245
2.00e-1	170	1.75e2	250
3.00e-1	233	2.01e2	260
5.00e-1	322		

3.4 Radiation Field in an Interim Storage Facility

Normally the simulation of a CASTOR is very time-consuming. By applying weight windows and surface sources, the efficiency of the simulation can be increased significantly. In this work a CASTOR V/19 and the on-site interim storage facility in the Philippsburg Nuclear Power Plant were chosen as an example, the detail calculation method including the usage of weight windows and the generation of surface source is discussed in this section.

As a part of this work, weight windows and surface sources have been employed during the bachelor thesis of Rick Frischek (Fritschek, 2009) in collaboration with the KIT and the Hochschule Furtwangen University (HFU).

3.4.1 On-site Interim Storage Facility in Philippsburg

In the Philippsburg Nuclear Power Plant, an on-site interim storage facility has been licensed in 2001. According to ref. (EnBW Kraftwerke AG, 2001), the interim storage building is 92 meters long, 37 meters wide and 18 meters high (see Figure 3.3 and Figure 3.4). CASTOR V/52 and CASTOR V/19 (see Section 3.4.2) loaded with spent fuels come from pressurized water reactors (PWR) and boiling water reactors are stored in the building before being transported to a final disposal site. Up to a maximum of 152 CASTORs can be stored in the storage building.

The building consists of three parts, two storage rooms (see Figure 3.3) and a loading region (see the left part of Figure 3.4). The size and material information of the walls of the building is as follows (EnBW Kraftwerke AG, 2001):

- Outside wall - 70 cm ferro-concrete
- Roof - 55 cm ferro-concrete
- Wall between the two storage rooms - 30 cm concrete
- Wall between the loading region and the storage rooms - 80 cm concrete

3.4.2 CASTOR V/19

In the interim storage facility of the Philippsburg Nuclear Power Plant, CASTOR V/19 (for 19 PWR fuel assemblies, see Figure 3.5 (a) and Figure 3.5 (b)) or CASTOR V/52 (for 52 fuel elements from boiling water reactors) is used (EnBW Kraftwerke AG, 2011). In the simulations, only the CASTOR V/19 has been calculated as an example.

CASTOR V/19 is a cylindrical type of cask, which is mainly made of spheroidal-graphite cast iron. Neutron moderator rods are filled in the holes along the wall, so that not only gammas but also neutrons are shielded.

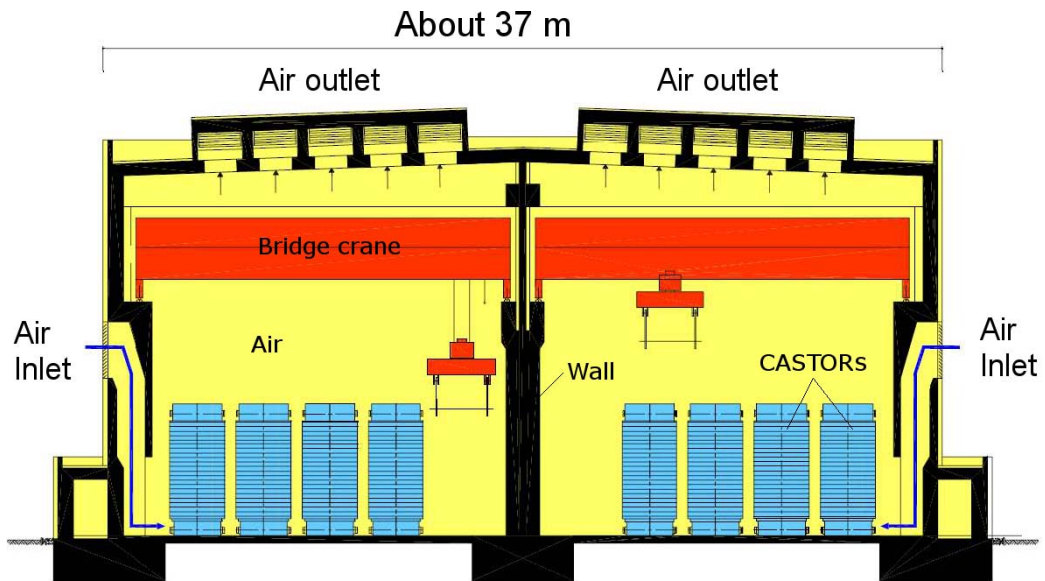


Figure 3.3: Sketch of the front view of the interim storage facility in the Philippsburg Nuclear Power Plant (EnBW Kraftwerke AG, 2001).

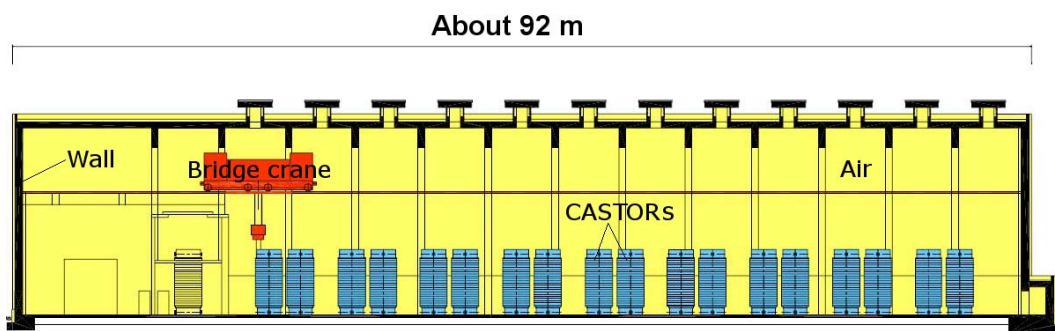


Figure 3.4: Sketch of the side view of the interim storage facility in the Philippsburg Nuclear Power Plant (EnBW Kraftwerke AG, 2001).

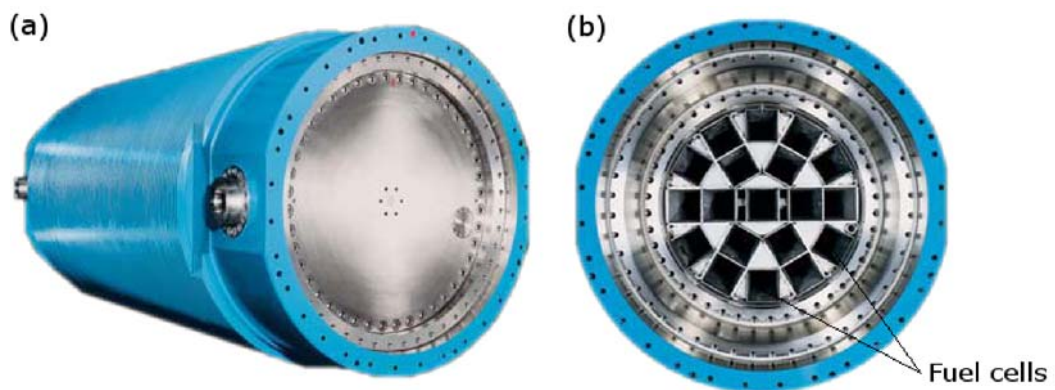


Figure 3.5: Pictures of CASTOR V/19 container (E.ON Kernkraft, 2011). (a) Side view; (b) cross section.

3.4.3 Modelling in MCNP

In order to perform Monte Carlo simulations, a geometry model of the CASTOR and the storage building should be implemented in MCNP. This model should include the actual size and material information of the CASTOR.

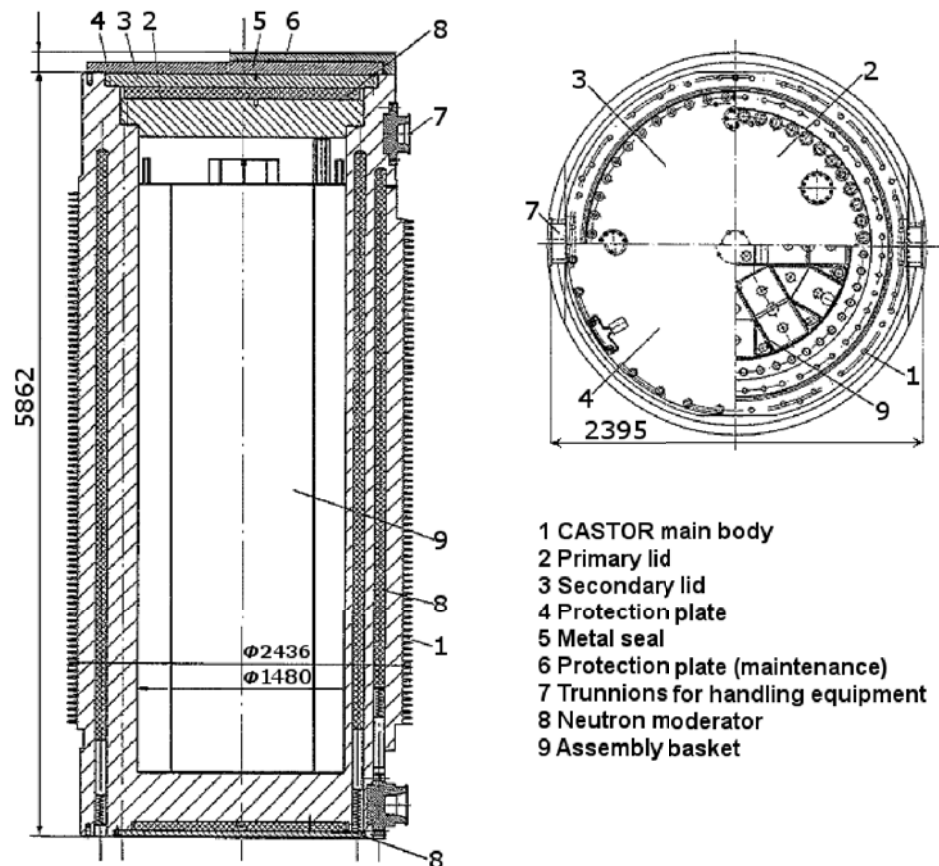


Figure 3.6: Sketch of CASTOR V/19 (Börst *et al.*, 2000).

Based on the dimension information in Figure 3.6, a simplified model was built in MCNP (the input file can be found in Appendix A.1) which consists of the spent fuel zone, steel wall and neutron moderators (see Figure 3.7). The model is 586.2 cm high, has inner diameter of 140.4 cm and outer diameter of 239.6 cm. The neutron moderator sticks are replaced with an equivalent layer of the moderator with a thickness of 11 cm. Two additional moderator layers of 9 cm are placed on the top and the bottom of the CASTOR, respectively. Since several simplifications, such as the cooling rip at the CASTOR surface was neglected, were made the size of the model is not exactly the same with the size in Figure 3.6.

A 18 m wide, 18 m high and 60 cm long room was created in MCNP5 as a model of one of the two storage rooms. The information of the wall thickness can be found in Section 3.4.1.

The composition of the material of the CASTOR wall is GGG-40, which is a kind of spheroidal-graphite cast iron. According to the information of ref. (Herzbach *et al.*, 2011), the atomic composition used for the calculations is as follows:

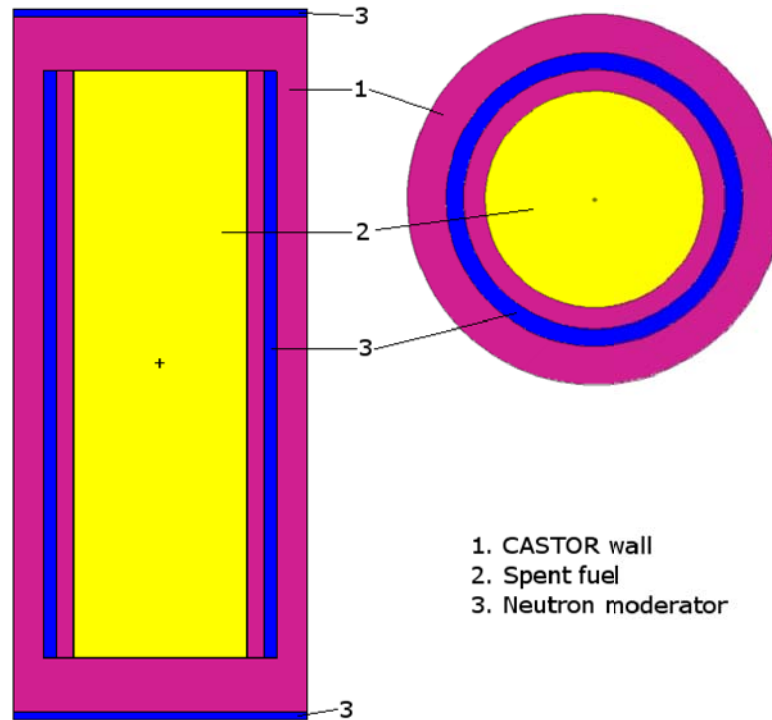


Figure 3.7: CASTOR V/19 model in MCNP5.

- Carbon — 3.65 %
- Silicon — 2.5 %
- Manganese — 0.4 %
- Phosphorus — 0.1 %
- Sulphur — 0.01 %
- Magnesium — 0.09 %
- Iron — 93.25 %

Normally, the density of GGG-40 ranges from 7.1 g/cm^3 to 7.3 g/cm^3 . 7.2 g/cm^3 has been chosen for the simulations.

Further material information is given in Table 3.3.

3.4.4 SCC Cluster

At the Steinbuch Centre for Computing (SCC) of the KIT, cluster systems are available for scientific computations. A Linux-Cluster called Opus-Cluster which consists of Opteron⁶ and Xeon⁷ nodes has been used in this work.

⁶AMD's x86 server and workstation processor

⁷Brand of multiprocessing- or multi-socket-capable x86 microprocessors from Intel Corporation

Table 3.3: Materials used for modelling the CASTOR V/19, taken from ref. (Williams III *et al.*, 2006) except the spent fuel which is taken from ref. (Hummelsheim and Hesse, 2009).

Material	Composition		density (g/cm^3)
	Element	wt. %	
Polyethylene	Hydrogen	14.3716	0.93
	Carbon	85.6284	
Concrete	Hydrogen	2.2100	2.3
	Carbon	0.2484	
	Oxygen	57.4930	
	Sodium	1.5208	
	Magnesium	0.1266	
	Aluminium	1.9953	
	Silicon	30.4627	
	Potassium	1.0045	
	Calcium	4.2951	
	Iron	0.6435	
Spent fuel	Carbon	0.0022	2.4
	Oxygen	9.403	
	Aluminium	0.0044	
	Silicon	0.0176	
	Chromium	0.5066	
	Manganese	0.0351	
	Iron	1.455	
	Nickel	0.6527	
	Zirconium	19.7135	
	Niobium	0.0486	
	Molybdenum	0.0265	
	Tin	0.2716	
	Barium-138	1.9899	
	Uranium-235	0.3642	
	Uranium-236	0.3772	
	Uranium-238	64.1826	
Plutonium-238	0.026		
Plutonium-239	0.4292		
Plutonium-240	0.2341		
Plutonium-241	0.2601		

The Opus-Cluster is based on the x86_64 processor architecture. The high-bandwidth low-latency InfiniBand communication link is used which is well suited for communication-intensive scientific applications using MPI. The cluster system provides a bandwidth of up to 20 GB⁸/s for access to remote disk systems. Many processors on the cluster are available for scientific calculations. For example, there are 98 Xeon nodes with 8 processors on each.

MCNP5 1.51 was compiled on the SCC cluster with MPI support (see Section 3.4.5). The simulations have been performed using parallel computing on the cluster.

The IBM LoadLeveler Workload Scheduler running on a Scientific Linux 4.x is used to allocate the available computer resource to different tasks. The LoadLeveler can provide the best match for different job requirements. To perform a calculation, a short script is needed, which tells the LoadLeveler what program should be launched, how many processors are required, and how long the calculation would last and so on.

A brief instruction for the use of the SCC cluster can be found in Appendix B. Example scripts are available in Appendix C.

3.4.5 Compiling MCNP5 1.51

MCNP5 1.51 has been used for the simulation for its improvement of sending surface source files via message passing. In MCNPX and the old version of MCNP5, the master process always sends the surface source file to the slave processors. Normally the size of the surface source is very large, which results in a long time to distribute the source data before starting the simulation.

One of the new features of MCNP5 1.51 is that it checks if the slave processes can read the surface source file directly. MCNP5 1.51 only sends the surface source when slaves can not read the file from the file system (Booth *et al.*, 2008). Taking advantage of this new feature, unnecessary time can be saved.

On the SCC cluster MCNP5 1.51 is neither pre-installed nor compiled, therefore compiling the source files has to be carried out. The steps to patch⁹ and compile the source files are given below:

1. Uncompress the MCNP5 1.50 source file
2. Download the patch "patch-MCNP5_RSICC_1.50_to_1.51" from RSICC website and save it to the MCNP5 directory
3. Change to the MCNP5 directory and apply the patch with the following command

```
$ patch -p1 < patch-MCNP5_RSICC_1.50_to_1.51
```
4. Create a script "compl.cmd" for compiling (see Appendix C)

⁸Gigabytes

⁹To fix software bugs or to add new features

5. Submit the script

```
$ llsubmit compl.cmd
```

3.4.6 Gamma and Neutron Source

The source data used in the simulations, which are taken from ref. (Hummelsheim and Hesse, 2009), are from the spent fuel with a decay time of 5 years and a burn-up of 55 GWd (Gigawatt-days).

The histogram spectra of gammas and neutrons can be found in Figure 3.8 and Figure 3.9. The source is considered as a homogeneous distribution of the fuel. The intensities are 1.534×10^{10} neutrons/s and 2.244×10^{17} photons/s, respectively.

3.4.7 Weight Windows

For a Monte Carlo simulation, it is necessary to have enough number of particle events. A high amount of events could lower the error of the result in the simulation. In many cases, the source particles inside the CASTOR can hardly reach the tally region, which influences the uncertainties. To solve this problem, a simple way is to increase the number of source particles. However, it also increases the calculation time. Since the relative error can be estimated to be proportional to the square root of the number of source particles, increasing the number of particles is generally not a good choice as it cannot improve the simulation efficiency.

A low efficiency of a simulation could be caused by inefficient sampling of space, energy or particle weights. Variance reduction techniques are very useful to increase the efficiency. In MCNP5 many variance reduction techniques are available like importance sampling, weight windows, source biasing, etc. Considering the thick wall of a CASTOR, the importance function is difficult to be specified manually. Fortunately, MCNP5's weight-window generator provides an automatic way to calculate the importance function. Therefore, the use of weight windows was chosen in our calculations.

In MCNP5 weight windows can be cell¹⁰-based or mesh¹¹-based. The mesh is a parallel geometry, which is independent of the geometry of a system. If mesh-based weight windows are used, no modification of the geometry is required in the input file, but only an additional mesh card is needed. The details of using weight windows can be found in ref. (Booth, 2004).

To generate the mesh-based weight windows for photons and neutrons (see Figure 3.10 and Appendix A.2), the density of the CASTOR wall was reduced at first to get enough events. Then the weight windows produced in the first run will be used as an input in the second run with the actual density (Booth, 2004). This process was carried out repeatedly to get the appropriate distribution of particle weights.

For both gamma and neutron sources, the mesh-based weight windows were generated for a track length tally in a cell which wholly covers the CASTOR V/19.

¹⁰Geometry spaces separated by surfaces

¹¹Parallel geometries which do not change the geometry space but the particle distribution

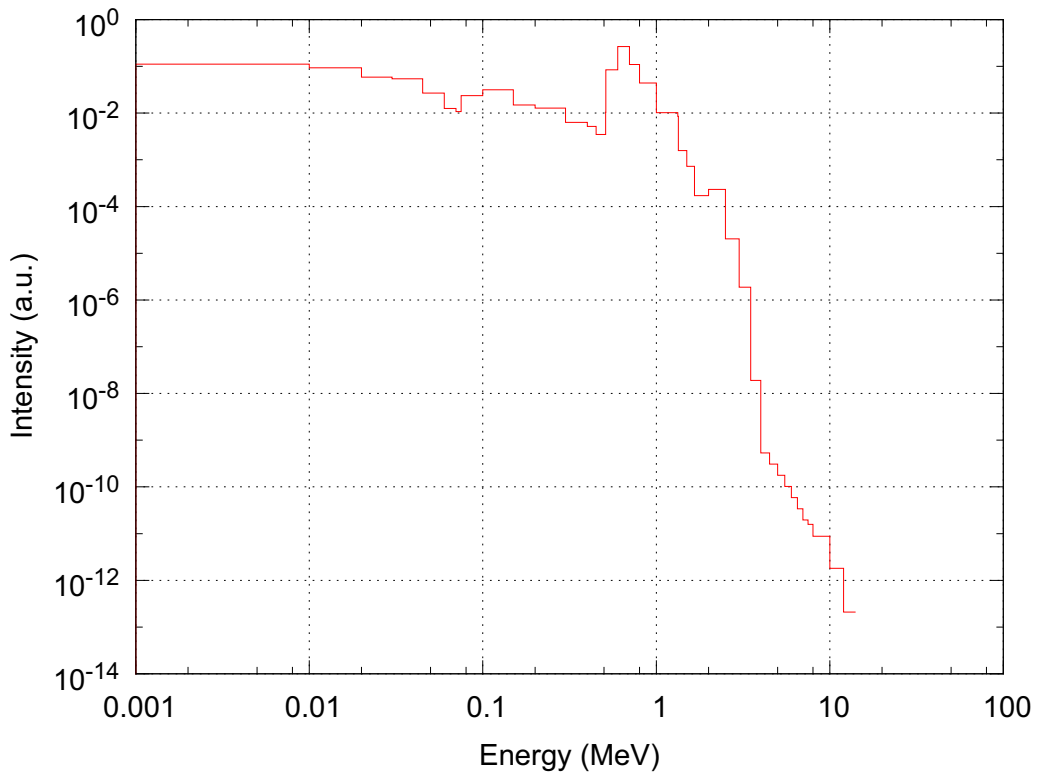


Figure 3.8: Gamma source spectrum of spent fuels inside a CASTOR V/19 (Hummelsheim and Hesse, 2009).

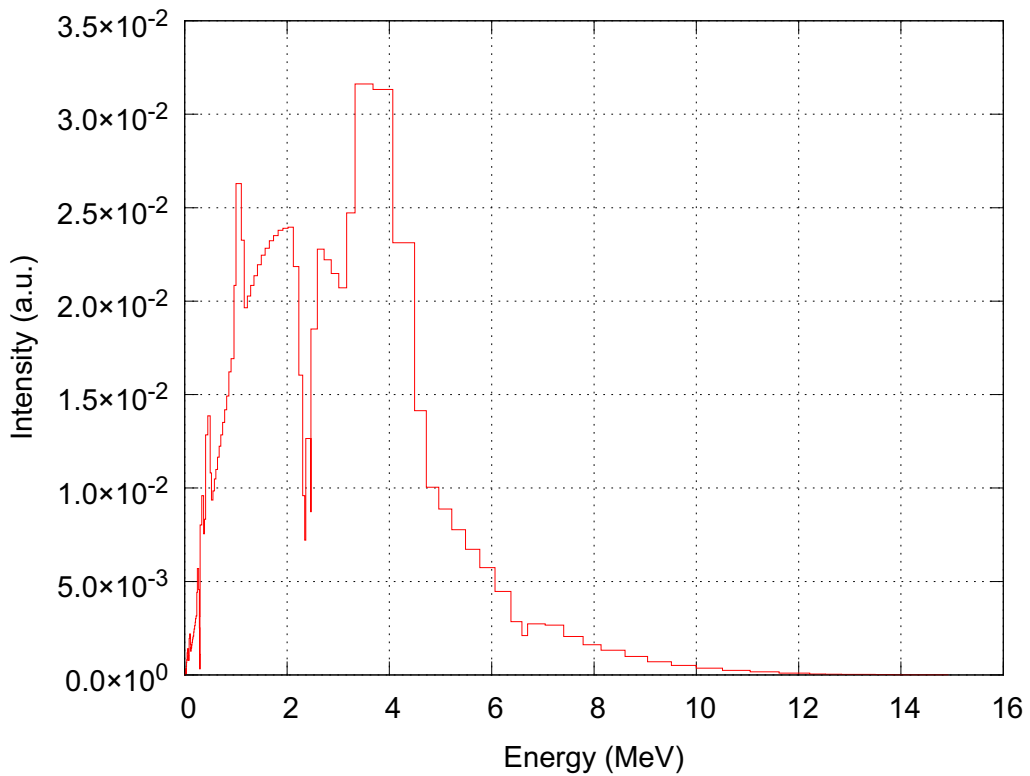


Figure 3.9: Neutron source spectrum of spent fuels inside a CASTOR V/19 (Hummelsheim and Hesse, 2009).

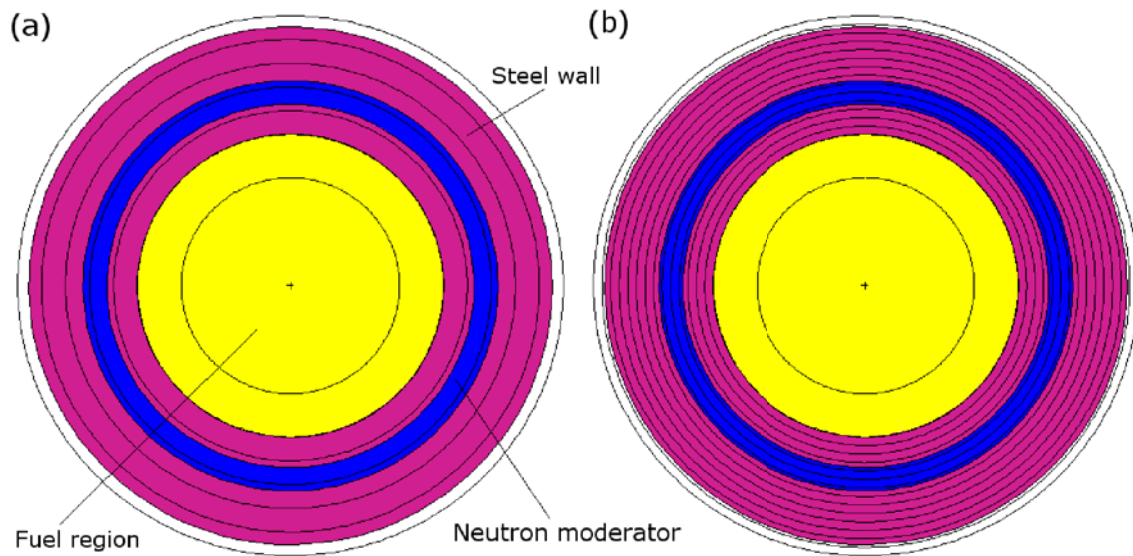


Figure 3.10: Mesh geometry (black lines) on the cross section of the CASTOR. (a) Mesh for the transport of gamma particles inside the CASTOR. (b) Mesh for the transport of neutron particles inside the CASTOR.

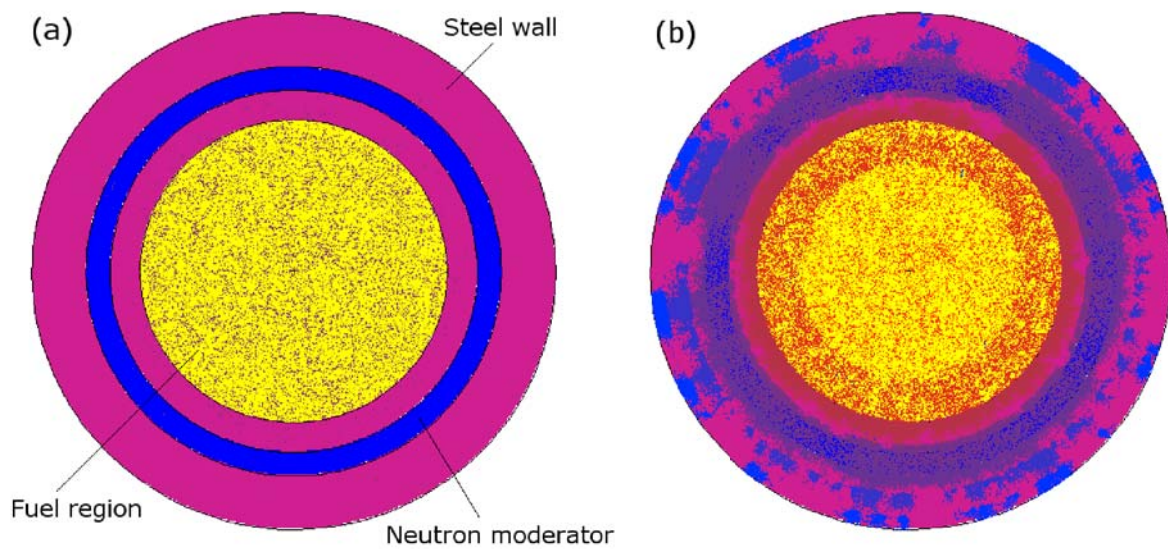


Figure 3.11: Particle distribution (points) on the cross section of a CASTOR with different calculation methods. (a) Analog simulation; (b) weight windows.

Figure 3.11 shows the effect of mesh-based weight windows. For the investigated geometry, when weight windows are not used, almost no particles come out of the wall of the CASTOR (see Figure 3.11 (a)). When weight windows are used, for the same number of source events many particles go through the wall (see Figure 3.11 (b)).

3.4.8 Surface Source

In our simulation, several tens of CASTORs were placed in the interim facility. It is very time consuming to perform calculations for the very complex geometry and large dimensions. Many calculation resources are used for the transport of source particle inside every CASTORs. For the CASTORs of same type and same source data, the transport of source particles inside the castor is not necessary to be repeated.

The idea is that only one of the CASTORs is calculated, and the information of all particles which cross the outer surface of the CASTOR would be saved to a file. This file can be used as a surface source in a new simulation, while translations can be applied to other CASTORs of the same type and same source. In this way the calculation resources needed for the transport calculation inside the CASTORs are saved.

Using the generated weight window files (see Section 3.4.7), 4×10^8 source particles for neutrons and 7.5×10^8 for photons were calculated to produce the surface sources on the outer surface of a CASTOR V/19. Eventually, a file of about 22 GB was generated for the neutron surface source; and a file of about 25 GB was created for the photon surface source.

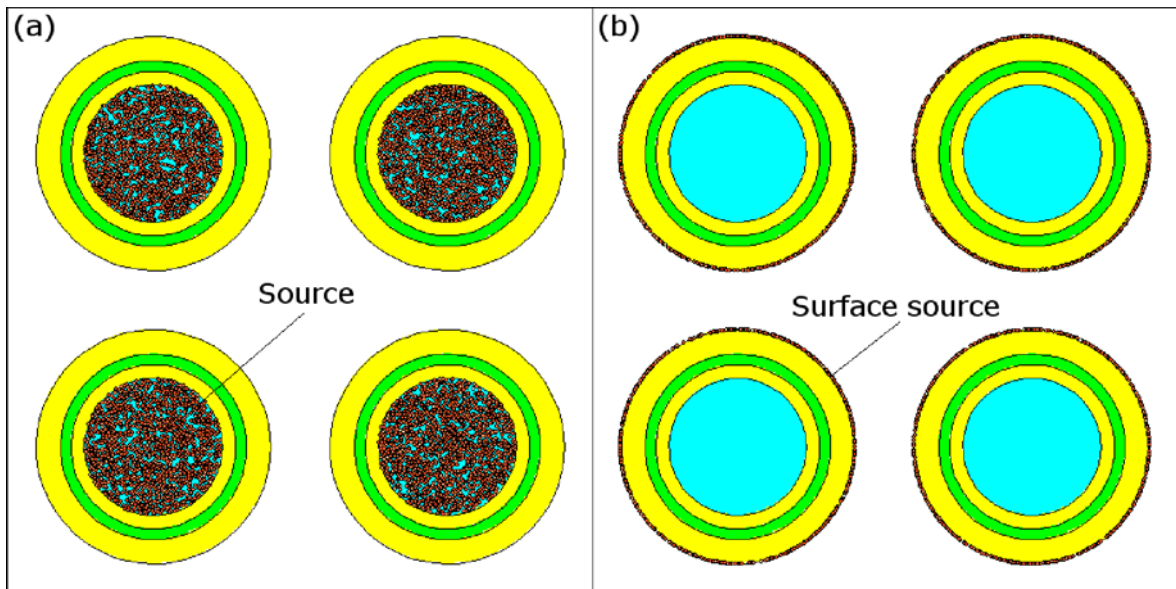


Figure 3.12: Source distribution (dark-red points) with different methods. (a) Analog simulation; (b) clones and translations of surface source.

In MCNP5 the idea can be easily implemented with the SSW (surface source write) and the SSR (surface source read) card. With a SSW card, based on the condition of the surface number, particle type and moving direction, the information of any particle of interest can

be recorded and saved to a file. Using weight windows and the SSW card, the information of particles which cross the outer surface of a CASTOR can be stored with an appropriate number of events. With the SSR card, the file saved by the SSW card can be imported as a source. The SSR card allows to make copies and translations of the source to other CASTORs.

As can be seen from Figure 3.12, unlike the original source (Figure 3.12 (a)), when surface sources are used, source particles distribute on the outer surface of the CASTOR (Figure 3.12 (b)).

3.5 Dosimeters

3.5.1 Albedo TLD¹² dosimeter

Li-6 and Li-7 both respond to beta and gamma radiation. In addition Li-6 also responds to neutrons via the ${}^6\text{Li}(n,\alpha){}^3\text{H}$ reaction. TLD dosimeters are often made of TLD-600 and TLD-700 (Horowitz *et al.*, 1979), which are composed of Li-6 fluoride and Li-7 fluoride, respectively.

Universal albedo neutron dosimeters (Piesch and Burgkhardt, 1985) have been developed and applied at the Karlsruhe Institute of Technology to measure the personnel dose. A universal albedo dosimeter consists of two pair of TLD-600/TLD-700 detectors and a boron-loaded plastic capsule which is a neutron absorber. There is a field neutron window on the front side of the capsule and an albedo neutron window on the rear side. One TLD-600/TLD-700 pair behind the field neutron window measures mainly thermal neutrons, while another pair behind the albedo neutron window measures albedo neutrons.

3.5.1.1 Dosimeter Geometry

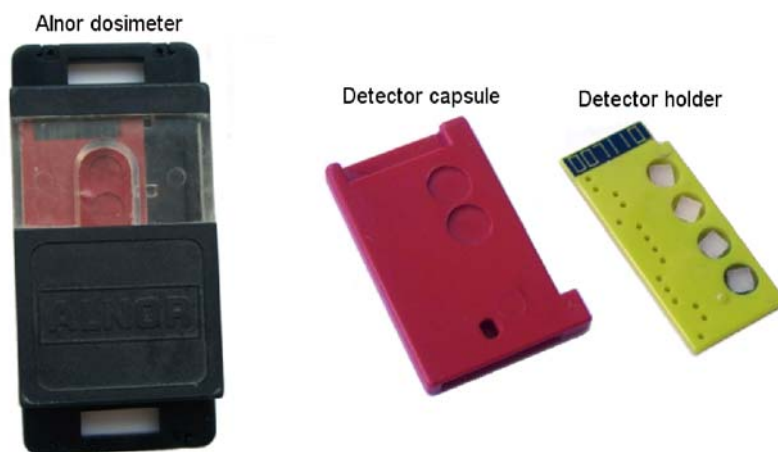


Figure 3.13: Alnor albedo neutron dosimeter.

Albedo-type dosimeters (see Figure 3.13) are still in use at KIT. As a kind of universal albedo dosimeter, it has the basic components and nuclear track detectors to detect fast

¹²Thermoluminescent Dosimeter

neutrons. The exploded view of an Alnor dosimeter can be found in Figure 3.14. Two TLD-600 (position 1 and 4) and two TLD-700 (position 2 and 3) are placed in a row. The detector capsule containing 4 detectors, which are fixed by the detector holder, is placed into the dosimeter capsule. The dosimeter capsule is made of boron-loaded plastic to absorb thermal neutrons. The detectors at position 1 and 2 face the field neutron window and the detectors at position 3 and 4 face the albedo neutron window.

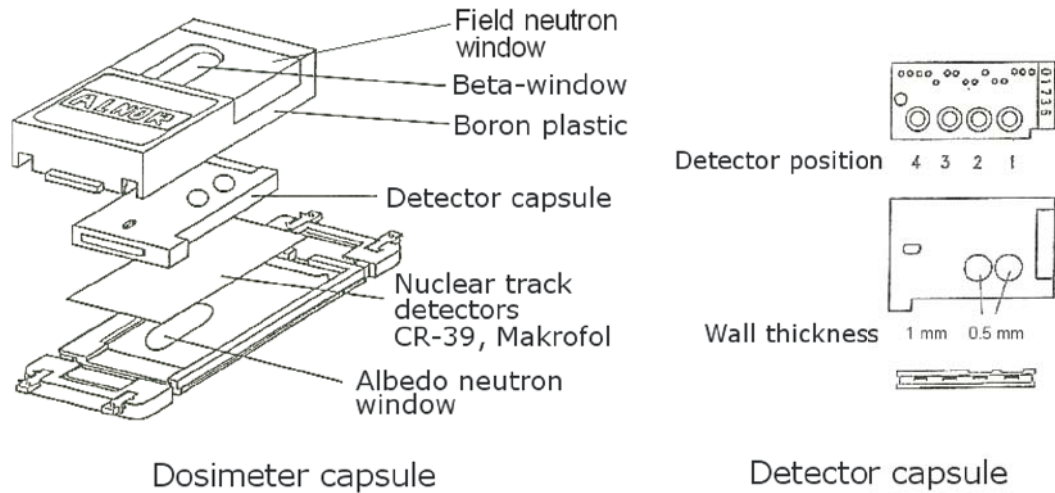


Figure 3.14: Exploded view of Alnor dosimeter (Burgkhardt *et al.*, 2000).

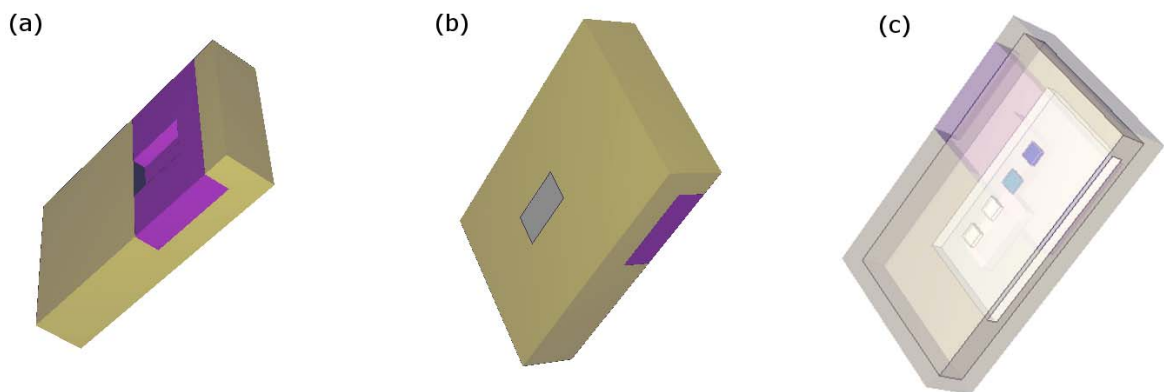


Figure 3.15: MCNP model of an Alnor albedo dosimeter. (a) Front view; (b) back view; (c) perspective view.

In MCNP an Alnor dosimeter has been modelled (see Figure 3.15 and Appendix D). The model is based on the real size of the dosimeter (see Figure 3.13). The materials of each component can be found in Table 3.4.

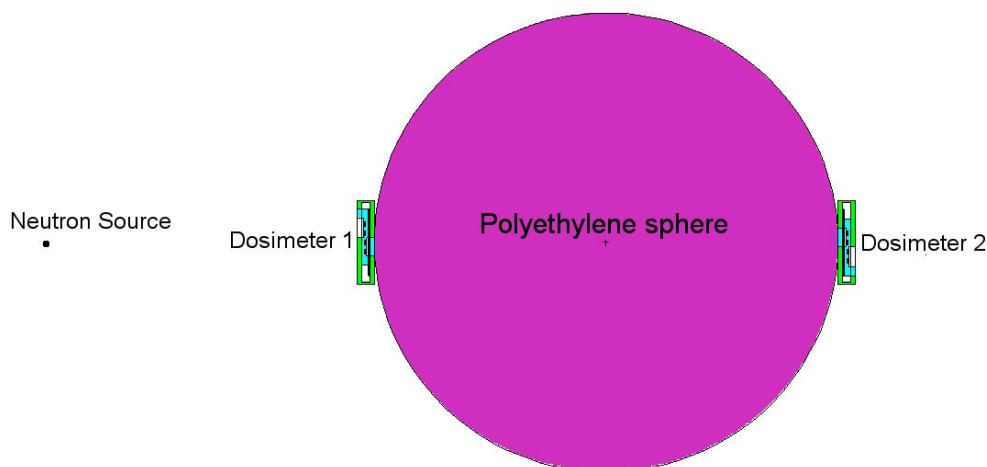
Table 3.4: Material information of an Alnor albedo dosimeter.

Component	Material	Dimension (mm^3)	Density (g/cm^3)
Detector TLD 600	$^6LiF:Mg, Ti$	$3 \times 3 \times 0.9$	2.6
Detector TLD 700	$^7LiF:Mg, Ti$	$3 \times 3 \times 0.9$	2.6
Detector capsule	Plastic	$35 \times 20 \times 4$	1.0
Field neutron window	Plastic	$34 \times 19 \times 5.5$	1.0
Dosimeter capsule	Plastic and 50 wt% B_4C	$55 \times 34 \times 11$	1.59

3.5.1.2 Simulations

The number of (n,α) reactions in Li-6, which is approximately proportional to the TLD reading, was used to calculate the response of dosimeters with the MCNP code.

Using the geometry of the field calibration technique described in the work of Burgkhardt and Piesch (Burgkhardt and Piesch, 1988), two Alnor albedo dosimeters are placed on the surface of a polyethylene sphere of 30 cm (an approximation to the ICRU sphere) in diametrically opposed positions (see Figure 3.16). The readings of two dosimeters are added together to reduce the angular dependence. The reading ratios of field neutrons to albedo neutrons were calculated for different mono-energetic incident neutrons.

**Figure 3.16:** Two Alnor dosimeters on a polythene sphere of 30 cm.

Burgkhardt's and Piesch's work (Burgkhardt and Piesch, 1988) shows that various neutron fields can be classified into four typical categories. Within each type of neutron fields, a constant calibration factor is used. In this work, the response of the detectors in the radiation field of the interim storage building relative to the Cf-252 neutron was calculated in order to investigate which type of neutron fields and correction factor should be used for the calibration.

As a result of small volumes of the TLD detectors inside the albedo dosimeter, the statistics of tally results are rather low. Mesh-based weight windows were used to reduce the relative error. Since most of particles can not reach the regions where the detectors locate, the

semi-deterministic F5 tally (fluence at a point detector), and a "fake" source which covers the whole geometry were used to generate the meshed-based weight windows (see ref. (Booth, 2004) for the generation of weight windows). The F5 point detector was placed in the center of the dosimeter, in which the response of the detectors is calculated. Using the generated weight windows (see Figure 3.17), the real source distribution of spent fuels and tallies to calculate the TLD readings were used to get results.

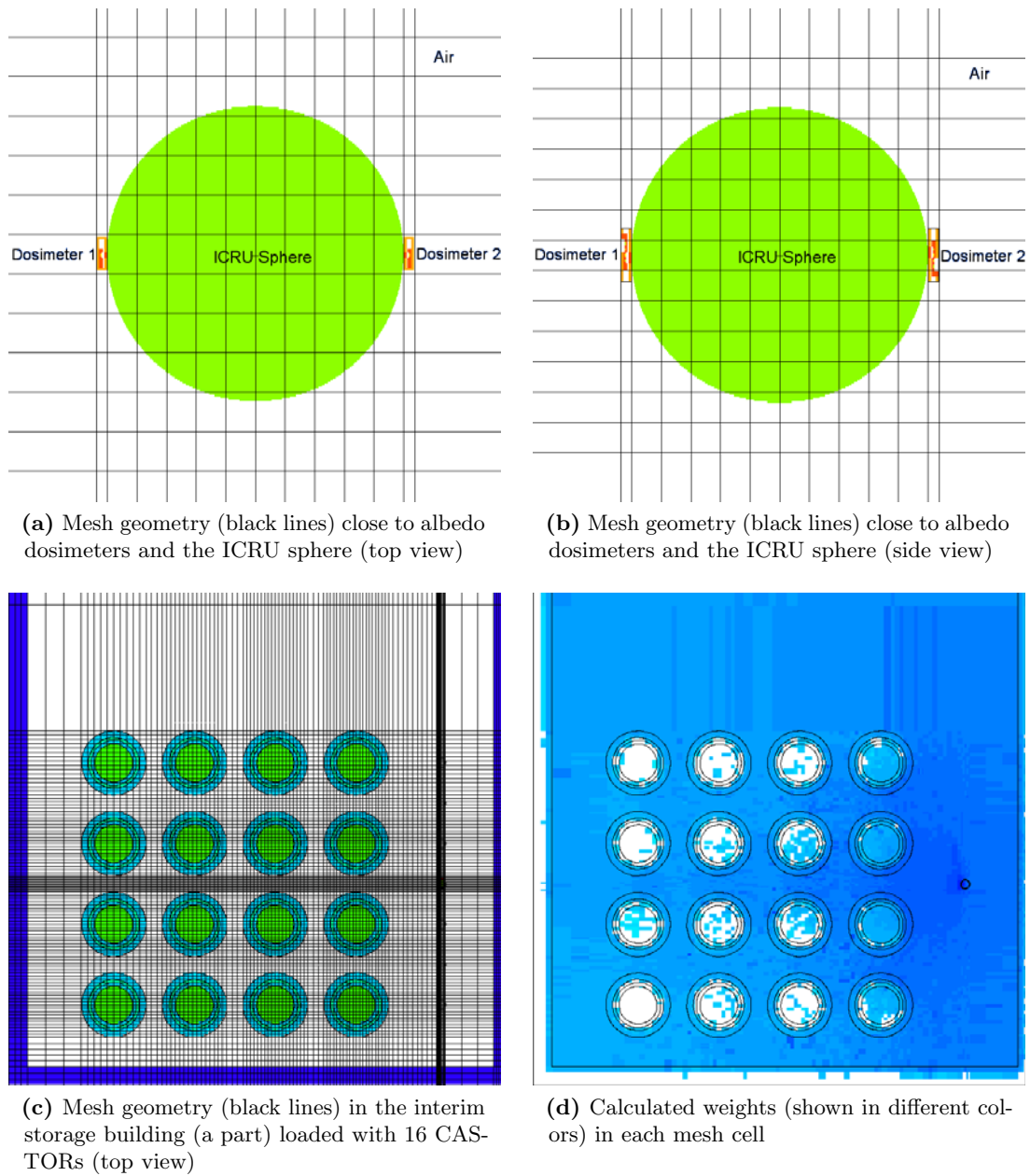


Figure 3.17: Mesh and weight windows for TLD simulation.

3.5.2 SSNTD

In this work, the response of Makrofol detecting fast neutron induced recoils as SSNTDs has been investigated with Monte Carlo particle transport codes. By applying several criteria of track formation, the response of Makrofol with respect to the track density was calculated. Response curves were calculated and verified with experimental results for different angles of incident neutrons.

3.5.2.1 Makrofol

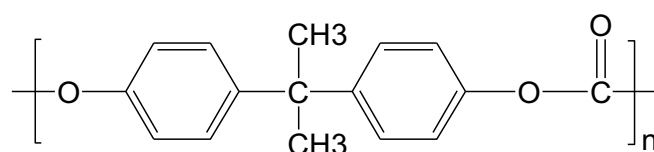


Figure 3.18: The structure of Makrofol polycarbonate (Singh and Prasher, 2006).

Makrofol (chemical composition $C_{16}H_{14}O_3$, density 1.2 g/cm^3) is the brand name for the polycarbonate manufactured by Bayer MaterialScience (Bayer Films Americas, 2011) in Germany (see Figure 3.18 for its structure).

Makrofol is widely applied in many fields of application including instrument panels, ID cards, medical equipment, dosimeters and so on. In the fields of radiation detection and dosimetry, Makrofol foils are usually used for detecting charged particles such as alphas, fission fragments and neutron induced recoils.

Due to the advantages of low cost, low background and good reproducibility, Makrofol detectors are used for radon survey and fast neutron measuring at KIT (Urban, 1986; Józefowicz and Piesch, 1990). The track detectors can also be integrated into albedo dosimeters (Piesch *et al.*, 1984).

3.5.2.2 Track Etching

The latent damage trail in the SSNTDs can not be observed directly because of their very small diameter (several tens to hundreds of Å). To make the latent tracks visible, an etching procedure should be applied to fix and enlarge them. Because the etching takes place in the region of the track core much faster than in the undamaged bulk material, latent tracks will become observable track pits after a period of the etching (see Figure 3.19).

An optimised two-step ECE etching procedure has been applied in the KIT solid state dosimetry laboratory, which is described in section 3.5.2.5, and a digital image analysis system is used to read the track densities.

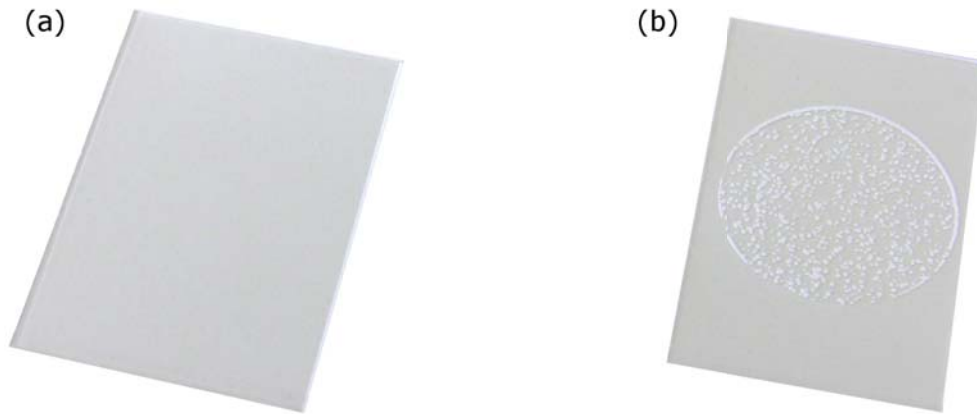


Figure 3.19: Pictures of (a) unetched and (b) etched Makrofol detectors.

3.5.2.3 Track Formation Mechanisms

Not all latent tracks will be revealed after an etching procedure. Many tracks are not revealed due to their short ranges, moving directions or other reasons. For example, recoil protons do not form etchable tracks in Makrofol (Józefowicz, 1971).

Many factors affect the track revealing. Various etchant compositions, voltages, temperatures and other parameters will yield different results. To simulate the response of Makrofol nuclear track detectors, these factors should be considered carefully.

In this section several important parameters will be described.

Energy Threshold

Some researchers have found that there is an energy threshold for an ion to form a visible track. Heavy charged particles with energies below the energy threshold do not form visible tracks after etching.

In the work of Katz and Kobetich (Katz and Kobetich, 1968), the critical dosage of ionization energy to form etchable tracks were calculated. Ions need enough energy to induce ionization at a certain distance from their path to form etched tracks. Based on the curve calculated for Lexan (polycarbonate like Makrofol), the minimum energies are 0.32-0.35 MeV for carbon ions and 0.37-0.40 MeV for oxygen ions. Józefowicz (Józefowicz, 1971) observed tracks in 1.2 MeV neutron irradiated Makrofol E foils. As the maximum energy transfer ratio is about 0.284 for neutron-carbon collision, the related energy of carbon is about 0.34 MeV.

Later on, tracks from carbon ions of 240 keV and oxygen ions of 320 keV in Makrofol E were reported by Saint-Martin et al. (Saint-Martin *et al.*, 1996). In fact, the energy threshold varies with different materials and etching procedures.

In this work, for the simulations of SSNTDs, thresholds of 240 keV for carbon and 320 keV for oxygen have been adopted as an approximation to Makrofol DE 1-4 material and the two-step ECE etching procedure.

Restricted Energy Loss

Various criteria of track formation, which are related to different parameters were suggest by different researchers. In this section, the restricted energy loss, REL (Beton and Nix, 1969), is discussed.

The REL is simply the energy loss rate of incident particle in the stopping material due to the collisions with electrons. The collisions results in the ejection of electrons of a certain energy. Only the part of energy loss less than a predetermined value T_{cut} is assumed to be relevant to the track formation.

The REL can be computed using the Bethe-Bloch equation (see Eq. 3.1 and ref. (Bichsel *et al.*, 2006)) or the SRIM code (Ziegler *et al.*, 2008) for different energy regions, respectively (Cecchini *et al.*, 2008).

$$-\frac{dE}{dx} = Kz^2 \frac{Z}{A} \frac{1}{\beta^2} \left[\frac{1}{2} \ln \frac{2m_e c^2 \beta^2 \gamma^2 T_{upper}}{I^2} - \beta^2 - \frac{\delta(\beta\gamma)}{2} \right] \quad (3.1)$$

where

$K = 0.307075 \text{ MeVg}^{-1} \text{ cm}^2$;

z — effective charge number of the incident particle;

Z — atomic number of absorber;

A — atomic mass of absorber;

β — ratio of the velocity of the particle to the velocity of light;

$m_e c^2 = 0.511 \text{ MeV}$, the rest energy of electron;

$\gamma = (1 - \beta^2)^{-1/2}$;

I — mean excitation energy;

$\delta(\beta\gamma)$ — density effect correction to the ionization energy loss.

The effective charge z of an incident ion with atomic number Z_i can be calculated with the following formula (Durrani and Bull, 1987):

$$z = Z_i [1 - \exp(-130\beta/Z_i^{2/3})] \quad (3.2)$$

The density effect correction to the ionization energy loss $\delta(\beta\gamma)$ can be calculated with Sternheimer's formula (Sternheimer *et al.*, 1984):

$$\delta(\beta\gamma) = \begin{cases} 0 & X < X_0 \\ 4.6052X + \alpha(X_1 - X)^m + C & X_0 < X < X_1 \\ 4.6052X + C & X < X_1 \end{cases} \quad (3.3)$$

where

$$X = \log(\beta\gamma) \quad (3.4)$$

T_{max} is defined as the maximum kinetic energy which can be imparted to a free electron in a

single collision, which can be calculated with Equation 3.5:

$$T_{max} = \frac{2m_e c^2 \beta^2 \gamma^2}{1 + 2\gamma m_e/M + (m_e/M)^2} \quad (3.5)$$

For Makrofol $T_{cut} = 350 \text{ eV}$ (Cecchini *et al.*, 2008), $Z/A = 0.52697$ (Sternheimer *et al.*, 1984), $I = 69.5 \text{ eV}$ (Beton and Nix, 1969) has been used. In addition:

$$T_{upper} = \min(T_{cut}, T_{max}) \quad (3.6)$$

Critical Angle

Recoils with an incident angle above the critical angle do not form a visible track. Based on the mechanism of track etching, the critical angle can be expressed as a function of the etching-rate-ratio (V), which is the ratio of the track etching velocity (V_T) to the bulk etching velocity (V_B). The correlation is given by the following equation:

$$\cos(\theta_c) = \frac{1}{V} = \frac{V_B}{V_T} \quad (3.7)$$

$$\theta_c = \text{arcsec}(V) \quad (3.8)$$

When the incident angle θ of an ion is larger than the critical angle θ_c , namely $V_T \cdot \cos(\theta) < V_B$ (see Figure 3.20), which results in that the etched pit will not reach the new surface when the whole layer containing the track is etched away.

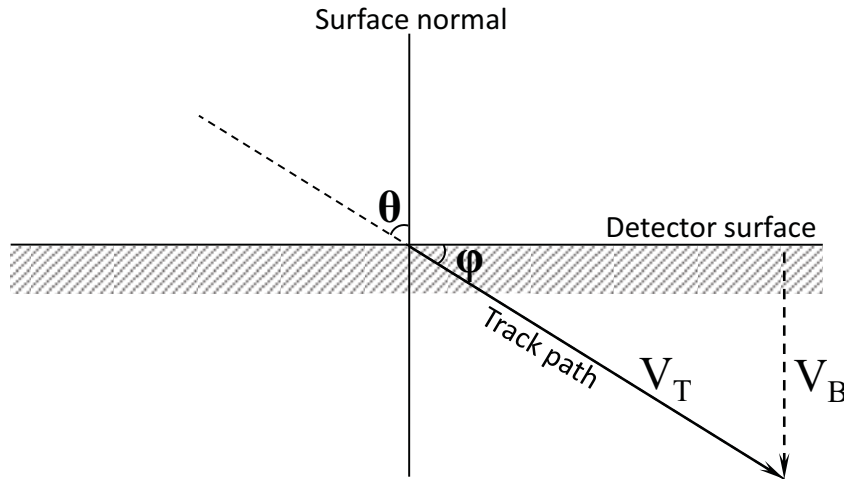


Figure 3.20: Geometry of track etching. V_T is track etching velocity, and V_B is bulk etching velocity. $\cos\theta = \sin\phi = V_B/V_T$.

The critical angle varies with different ions and different energies of the ions. In an earlier work (Somogyi *et al.*, 1976) it was found that, for most of the commercial plastics, V can be

approximately described by the relation:

$$V = 1 + \alpha REL^\beta \quad (3.9)$$

where the unit of the REL is $MeV/(mg/cm^2)$.

Based on Equation 3.9 and the value of REL, which can be calculated with the method described in Section 3.5.2.3, the critical angle can be calculated.

In Equation 3.9 the values of α and β vary with different detector materials and different etching conditions. The corresponding values were determined to describe the Makrofol DE 1-4 detector material and the two-step ECE procedure at KIT.

3.5.2.4 Monte Carlo Simulation

The method of simulating the response of Makrofol as a SSNTD is discussed in this section. In combination of Monte Carlo simulations with track counting criteria, the method to calculate the response of Makrofol detectors to fast neutrons are discussed in detail.

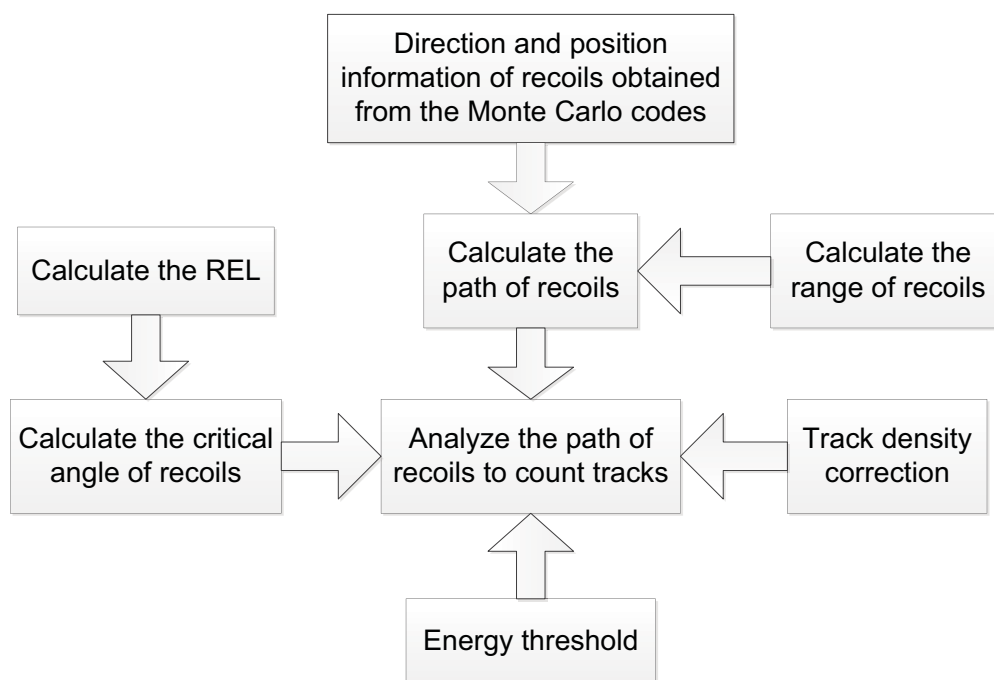


Figure 3.21: Diagram of the SSNTD simulation.

To perform the simulation, there are some essential assumptions to be noticed:

- Trajectories of heavy recoils are approximate straight lines
- Many of early etch pits, once formed, continue to be visible until a time limit is reached
- Track etching rates are constant

Based on the track formation criteria (see Section 3.5.2.3) and the assumptions above, the response of the Makrofol nuclear track detector is calculated with the Monte Carlo codes MCNPX and Geant4 by applying the track formation criteria (see Figure 3.21).

The Monte Carlo codes simulate the transport of neutrons in Makrofol detectors. All the information of interest, including position, direction, energy and type of recoils were archived into a plain text file. For different energy regions, RELs were calculated with the Bethe-Bloch equation and SRIM, which was also used for computing the range of recoils. Using the calculated REL and range values, a counting program SSNTDKIT (see Section 3.5.2.4 for more details) reads the file saved by the Monte Carlo code, calculates the path of recoils and the REL-related critical angle of the recoils. Then on the basis of the information above, SSNTDKIT determines whether a recoil can form a visible track on a certain etching surface (see Figure 3.22 for the procedure of track counting). Due to the very small proportion of latent alpha tracks, only carbon and oxygen recoils have been taken into account.

The track counting considers only tracks in a predetermined layer. For different combinations of α and β (see Equation 3.9), namely different results of critical angle, the track revelation is determined. In the present work, a layer which is thicker than the actual etched layer is taken into account to reduce the error of the counting, then the result is multiplied by a constant factor as a correction.

Sampling Watt Fission Spectra

For the simulation of the Makrofol detectors, the spectrum of Cf-252 is generated by sampling Watt fission spectra (Cullen, 2004) with coefficients of $a = 1.180000$ and $b = 1.03419$, which were taken from the MCNPX manual (Pelowitz, 2008). In MCNPX this can be done with one simple input card, but in Geant4 a sampling function has to be programmed to obtain the spectrum.

The probability density function of Watt Fission Spectra is the following:

$$f(E) = C \exp(-E/a) \sinh(bE)^{1/2} \quad (3.10)$$

The algorithm of sampling Watt fission spectra can be described as follows (for details see ref. (Everett and Cashwell, 1983)):

Define \hat{a} , K , L and M ,

$$\hat{a} = 1/a \quad (3.11)$$

$$K = 1 + (b/8\hat{a}) \quad (3.12)$$

$$L = \hat{a}^{-1}K + (K^2 - 1)^{1/2} \quad (3.13)$$

$$M = \hat{a}L - 1 \quad (3.14)$$

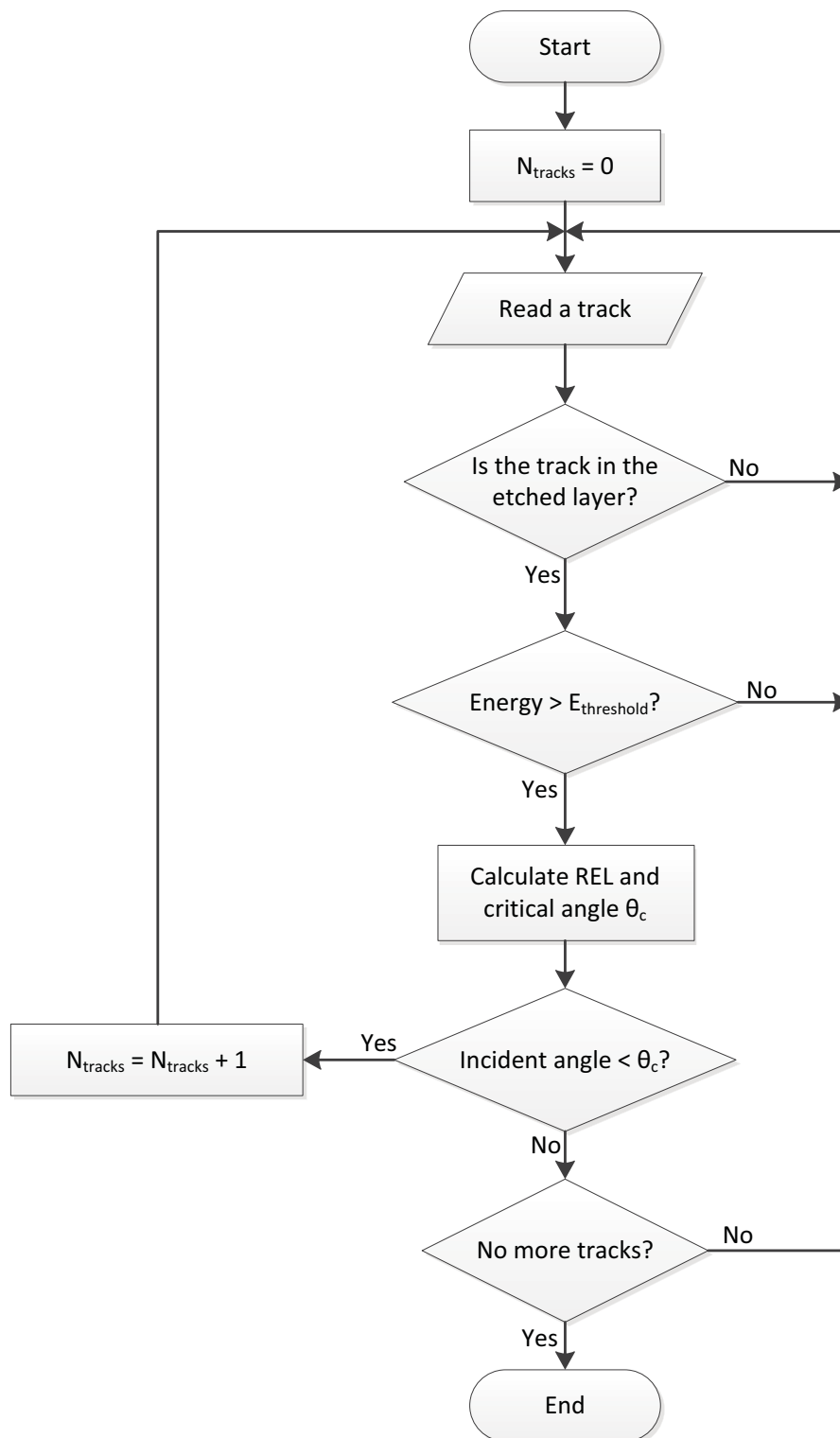


Figure 3.22: Flow chart of track counting based on simulation data.

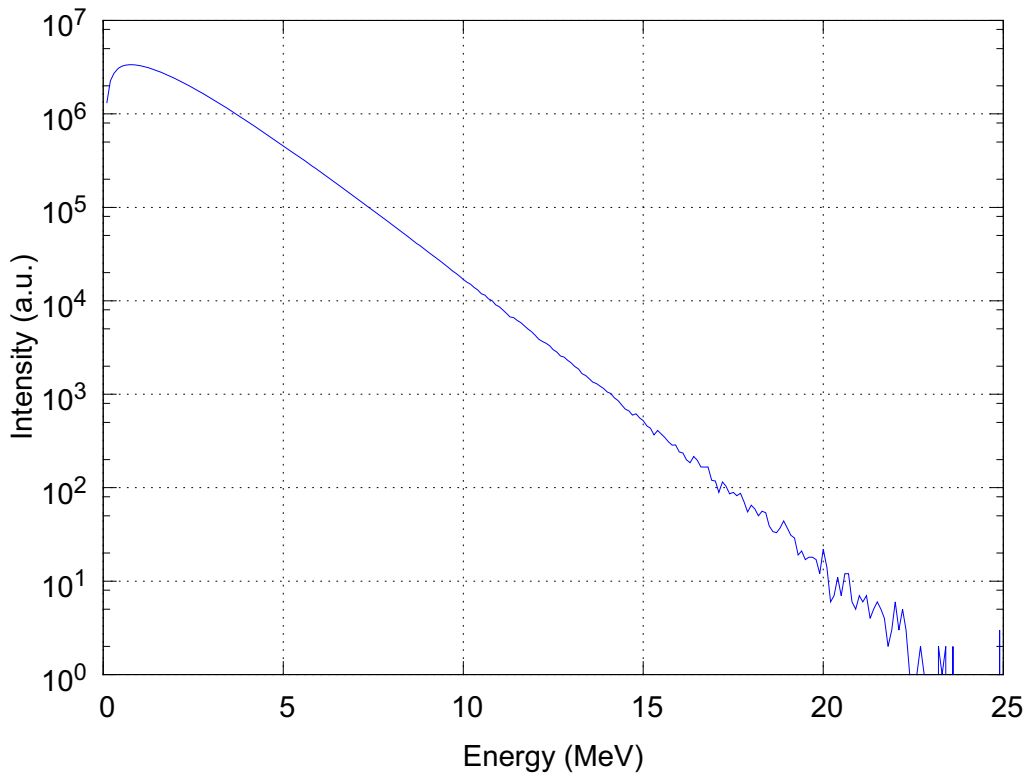


Figure 3.23: Calculated Cf-252 Spectrum.

Define x and y with two different random numbers, r_1 and r_2 ,

$$x = -\ln r_1 \quad (3.15)$$

$$y = -\ln r_2 \quad (3.16)$$

Accept x if $(y - M(x + 1))^2 \leq bLx$, otherwise define x and y again.

The spectrum of Cf-252 calculated with above algorithm is shown in Figure 3.23.

Rotating Vectors

In the "HISTP" file of MCNPX, the direction vectors are given with respect to the direction of incident neutrons. Rotations are needed to convert the vectors into the laboratory coordinate system.

In the "old" coordinate system, the moving direction vector of the neutron is $(0, 0, 1)$ while it is (u_n, v_n, w_n) in the laboratory coordinate system. In order to make the conversion between two coordinate systems, a rotation matrix which can rotate $(0, 0, 1)$ to (u_n, v_n, w_n) is needed.

As can be seen from Figure 3.24. The direction vector (u_n, v_n, w_n) can be obtained by rotating $(0, 0, 1)$ around y -axis with an angle of β clockwise, then around z -axis with an angle of γ clockwise.

The rotation can be implemented with the following rotation matrix (Weisstein, 2011):

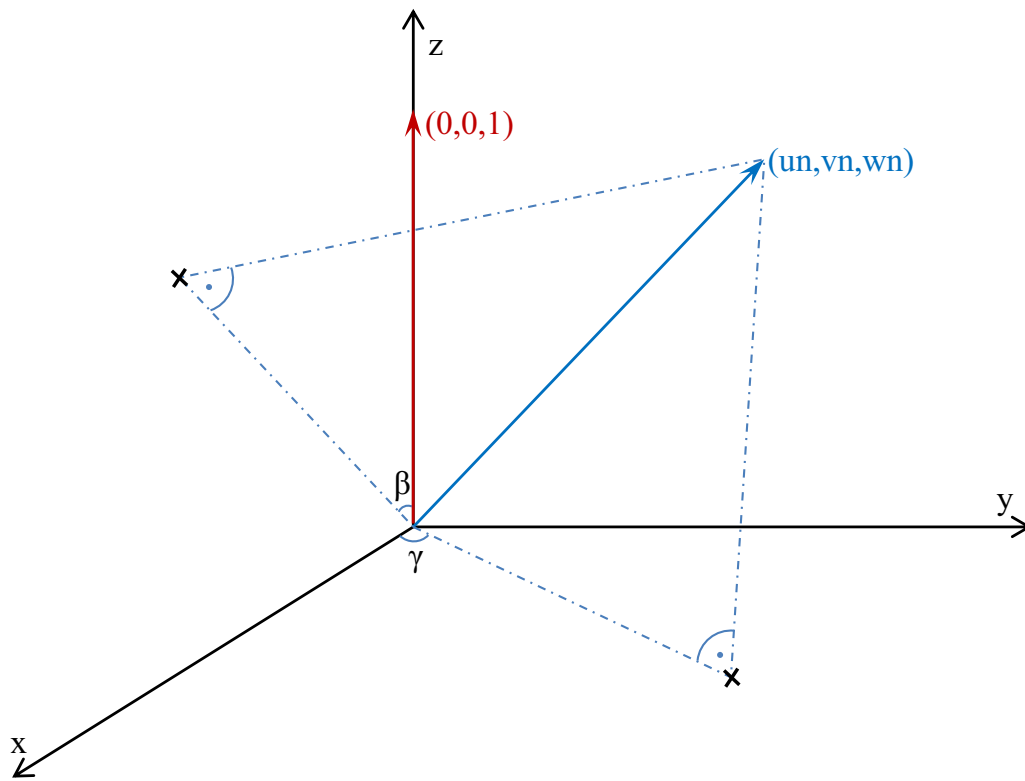


Figure 3.24: Rotating vector $(0, 0, 1)$ to vector (un, vn, wn) .

Rotate around y-axis with angle of β clockwise,

$$\begin{bmatrix} \cos\beta & 0 & -\sin\beta \\ 0 & 1 & 0 \\ \sin\beta & 0 & \cos\beta \end{bmatrix}$$

Rotate around z-axis with angle of γ clockwise,

$$\begin{bmatrix} \cos\gamma & \sin\gamma & 0 \\ -\sin\gamma & \cos\gamma & 0 \\ 0 & 0 & 1 \end{bmatrix}$$

Therefore, the rotation matrix should be:

$$\begin{bmatrix} \cos\beta & 0 & -\sin\beta \\ 0 & 1 & 0 \\ \sin\beta & 0 & \cos\beta \end{bmatrix} * \begin{bmatrix} \cos\gamma & \sin\gamma & 0 \\ -\sin\gamma & \cos\gamma & 0 \\ 0 & 0 & 1 \end{bmatrix} = \begin{bmatrix} \cos\beta\cos\gamma & \cos\beta\sin\gamma & -\sin\beta \\ -\sin\gamma & \cos\gamma & 0 \\ \sin\beta\cos\gamma & \sin\beta\sin\gamma & \cos\beta \end{bmatrix}$$

Accordingly, an arbitrary vector (uc, vc, wc) in the old coordinate system can be trans-

formed to a vector (ul, vl, wl) in the new coordinate system through the following formula:

$$\begin{pmatrix} ul & vl & wl \end{pmatrix} = \begin{pmatrix} uc & vc & wc \end{pmatrix} * \begin{bmatrix} \cos\beta\cos\gamma & \cos\beta\sin\gamma & -\sin\beta \\ -\sin\gamma & \cos\gamma & 0 \\ \sin\beta\cos\gamma & \sin\beta\sin\gamma & \cos\beta \end{bmatrix}$$

Compiling MCNPX 2.6.0

As the official version of MCNPX 2.6.0 cannot retrieve the detail information of neutron induced heavy recoils, a modified version has to be compiled from the source code.

The steps to patch¹³ and compile the source file of MCNPX on Windows (the script for Linux can be found in Appendix C) are given below.

1. Uncompress the MCNPX 2.6.0 source file.
2. Save the patch in Appendix E to a file, for example "patch.MCNPX.SSNTD". Put the file to the MCNPX directory. In addition, this patch also modifies the source file of HTAPE3X.
3. Change to the MCNPX directory and apply patch with the following command¹⁴:
`$ patch -p1 < patch.MCNPX.SSNTD`
4. Create a build directory "MCNPX_BLD" at the same level as your MCNPX directory.
5. Change to the MCNPX_BLD directory and compile.
`$ cd MCNPX_BLD`
`$..\MCNPX\configure I8 MPI`
6. Set environment variable DATAPATH to the directory where your cross section data are.

Simulation with MCNPX

MCNPX 2.6.0 is able to transport both neutrons and heavy ions. The modified version of MCNPX can retrieve the information of neutron induced heavy recoils, which includes atomic number, mass number, position, moving direction (with respect to the normal to the detector surface) and so on. Using the HISTP card, all information can be saved to a binary file. The modified HTAPE3X can read the binary file generated by MCNPX and save the information needed for track counting to a plain text file.

Generally, neutron transport is based on evaluated data libraries. Unfortunately, data libraries for the generation of heavy recoils are not available. Therefore, theory models were used for the simulation.

In order to use model physics to transport neutrons, the MX card and its MODEL parameter should be applied in the input file of MCNPX. This card can replace the data

¹³To fix software bugs or to add new features

¹⁴This should be done with the Cygwin environment.

library of an element of a material with another element's library or a model for certain particles (see Appendix F.1).

A HISTP card is used to save the particle information of a related cell. After the simulation, a file called HISTPA or with a similar name will be generated. The modified HTAPE3X code can read the HISTP output file and can archive the information of interest. Similar to MCNPX, an input file is required (see Appendix F.2).

Simulations with Geant4

As a C++ tool-kit Geant4 has the advantage of flexibility, i.e. it allows the user to mix and match different processes and models, and to retrieve all information of interest in any possible formats. Particles can be killed right after their information is saved while other codes continue to simulate them.

The available models in Geant4 are called data driven models, theory driven models and parametrisation driven models. They are based on data, theory, and both data and theory, respectively. Data driven models, which are the highest precision models, were chosen for the Geant4 simulations. Following process and model classes were employed for the neutron transport (the source code can be found in Appendix G):

- Process (I): G4NeutronInelasticProcess
 - Model: G4NeutronHPInelastic ($0 < E < 20MeV$), G4BinaryCascade ($19.8MeV < E < 10GeV$)
- Process (II): G4HadronCaptureProcess
 - Model: G4NeutronHPCapture ($0 < E < 20MeV$), G4LCapture ($19.8MeV < E < 100TeV$)
- Process (III): G4HadronFissionProcess
 - Model: G4NeutronHPFission ($0 < E < 20MeV$), G4LFission ($19.8MeV < E < 100TeV$)
- Process (IV): G4HadronElasticProcess
 - Model: G4NeutronHPElastic ($0 < E < 20MeV$), G4LElastic ($E > 19.8MeV$)

The Geant4 kernel only handles processes which have a process class registered, and calculates the final state of particles with associated models of the process. In this work the data driven high precision models are assigned to 4 registered neutron process classes, which are used for elastic scattering, inelastic scattering, capture and fission, for neutrons with energies below 20 MeV.

The C++ source files of Geant4 style can be compiled on Windows, Mac OS X or Linux systems to generate a executable file. Without any further modification, a text file generated by the Geant4 executable includes the necessary information for the track counting.

Density Correction

When two tracks are at the same position or very close to each other, they can be recognized as only one track. For low track density, this effect can be neglected due to the low overlapping probability. With the increase of the track density, the portion of overlapping tracks also increases. The track density will be overestimated by the simulations compared to the experiments if the effect of overlapping is not taken into account for high track densities.

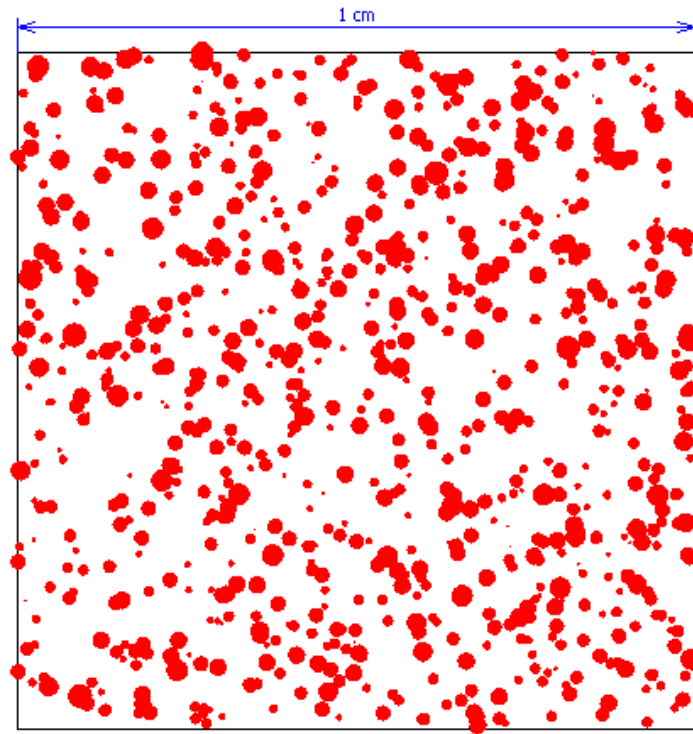


Figure 3.25: Simulated round tracks.

To correct for the overlapping effect, a Monte Carlo based C++ code has been developed in this work to simulate the behaviour of the track overlapping. In this code, the shape of track pit was considered to be round (see Figure 3.25). The distribution of the track diameters was obtained from experimental data. This was used for sampling track diameters in the simulations. The positions of tracks are determined by random numbers of a uniform distribution. For a given distance limit of tracks, when the centers of two tracks are closer than the distance limit value, they are counted as one track. As a result, correction factors (the ratio of the number of residual tracks, which is the number of track considering the overlapping, to the number of total tracks, which is the number of tracks without considering the overlapping) for the counting can be determined from the code for different track densities (see Appendix H for details).

Figure 3.26 shows the detailed work flow of calculating the density correction factor. First, the positions and diameters of tracks are sampled with random number which are generated with a random number generator. Positions are uniformly distributed in the whole area, and diameters are determined with the distribution of experimental results. Then, the distances

of any two tracks are calculated. When two tracks are too close, 1 will be subtracted from the total number of tracks. Finally, the residual number of tracks divided by the initial number of tracks is the density correction factor.

SSNTDKIT

SSNTDKIT stands for Solid State Nuclear Track Detector toolKIT, which has been developed based on Qt in this work. This is used to process the data generated with Monte Carlo codes and to calculate the response of the Makrofol detectors (see Appendix I for more details).

To simulate the response of Makrofol detectors, the data of recoils need to be processed and analyzed on the basis of track formation criteria. The range, restricted energy loss, and critical angle of each recoil needs to be calculated, and every track should be decided whether it can be revealed. Many data are needed for the simulation. The SSNTDKIT code integrates all data and parameters together to perform the simulation in an efficient way.

The following tasks can be done with SSNTDKIT:

- Calculating ranges of heavy recoils in Makrofol
The range tables of carbon and oxygen for different energies are calculated with SRIM. Based on the table, SSNTDKIT calculates the range of different ions by using interpolation between 2 neighbouring values.
- Reading the text file generated by Monte Carlo codes
Reads the text file generated by Monte Carlo codes to produce a new file which is used for track counting. In the new file, track paths are calculated in terms of two end points of tracks which are determined on the basis of the range, moving direction and position of the tracks.
- Calculating the REL
In the low energy region, REL is computed by interpolating the data from SRIM. The Bethe-Bloch formula is applied for the higher energy region.
- Calculating the critical angle
Based on the relation of REL and critical angle, SSNTDKIT calculates critical angles for carbon and oxygen recoils, using values of α and β given by the user.
- Track counting
Using the threshold and critical angle rule, SSNTDKIT determines whether a latent track can be revealed after etching. The number of etchable tracks in an assigned layer is stored in a plain text file.
- Error calculation
The relative errors of the track densities are calculated.

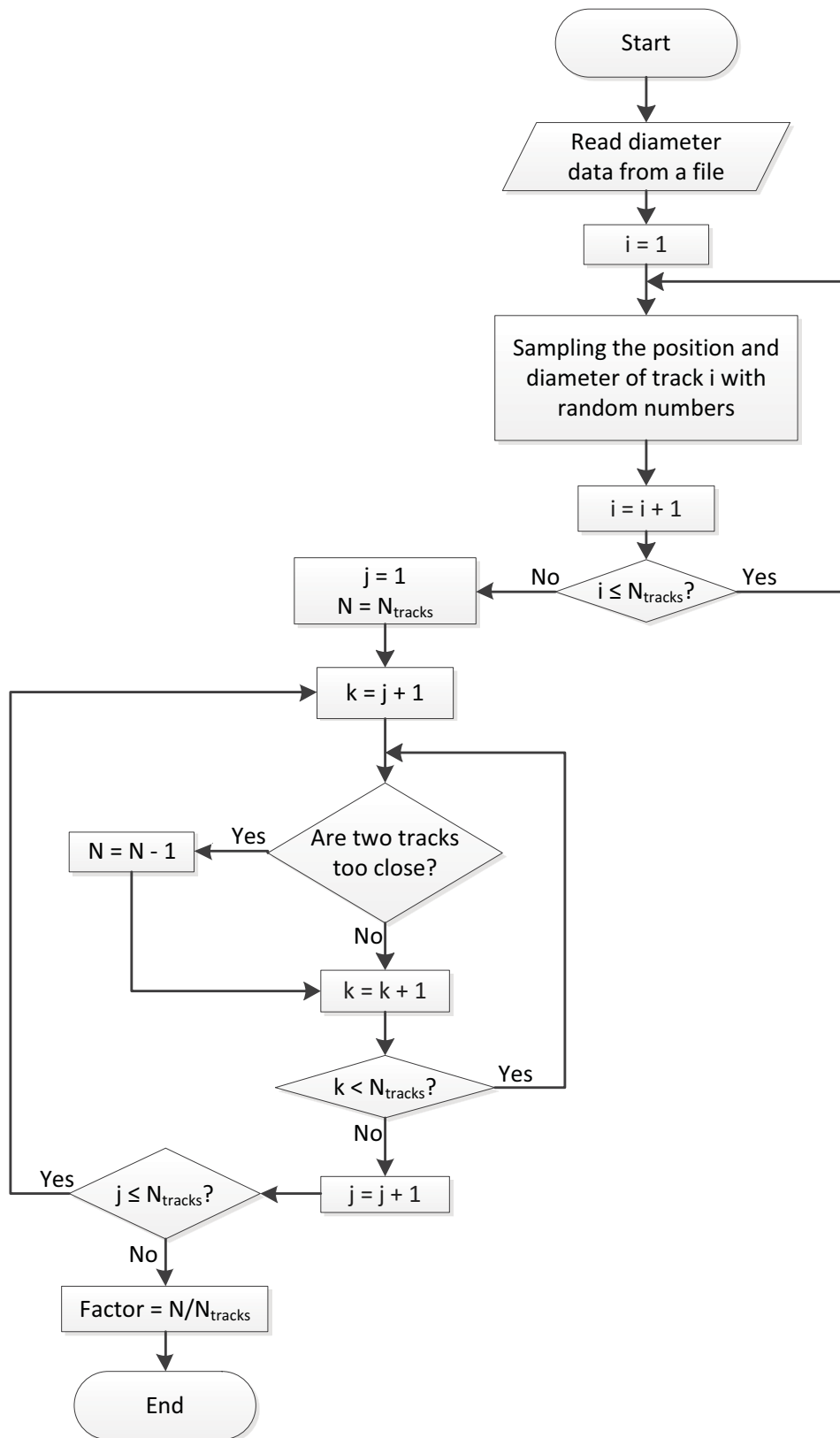


Figure 3.26: Flowchart of the calculation of the track density correction factor. i, j, k : integer counters; N : residual number of tracks; N_{tracks} : total number of tracks.

- Calculating the density correction factor.
For different track densities, SSNTDKIT can calculate the density correction factor to simulate the track overlapping effect.
- Plotting
The simulated round tracks, the angular response curve, and the density correction factor curve for different track densities can be plotted.

The SSNTDKIT program is platform independent and can run on Windows, Linux and Mac OS X systems.

3.5.2.5 Experiments

To verify the results of the simulations, two experiments with Cf-252 neutrons were carried out at KIT and PSI¹⁵, respectively. It turned out that the accuracy of the experiment at KIT could be improved due to the low source activity and a provisional detector holding device. To reduce the errors, a stronger Cf-252 source and a more precise angle adjustment device were used for the experiment performed at PSI. For the two experiments, the same two-step ECE procedure was carried out in the KIT solid state dosimetry laboratory.

Detector Pair and Etching Package

At KIT, Makrofol DE 1-4 (Bayer, Germany) detector pairs are normally used in practice. A detector pair consists of two identical detectors. A standard detector is about 3 cm long, 2 cm wide and 475 μm thick (see Figure 3.27). Only the glossy surfaces in between the pair will be etched to avoid the effect of surface scratches (Hassib, 1978).

To avoid the effect of alpha particles which exist almost everywhere in the environment, the detector pair is usually vacuum sealed in an aluminized plastic foil package (see Figure 3.28) which is evacuated with a vacuum device (Helmut Boss Verpackungsmaschinen KG, see Figure 3.29). More than one pair can be put into a package as needed.

Etching packages are placed in an electric heating cabinet (Memmert GmbH+Co.KG, see Figure 3.30) during the etching to maintain a constant temperature while an oscillating high voltage is applied. The etching package comprises Makrofol detectors, rubber seals, plastic slabs, and an etching frame (see Figure 3.31).

Two-step ECE Procedure

A standard KIT two-step ECE etching procedure (Piesch *et al.*, 1991; Józefowicz *et al.*, 1997) has been applied to reveal latent tracks. The two-step ECE was performed at an etching temperature of 40 °C, with an etching voltage of 2 kV, an etchant of 6.5N KOH water solution and ethanol (99.8%) with a volume ratio of 1:1, and an etching frequency of 100 Hz for 5 h followed by 2 kHz for 1 h (see Appendix J). Basically, the etching procedure includes three parts: chemical etching (CE), electro-chemical etching (ECE) and post etching (PE).

¹⁵Paul Scherrer Institute

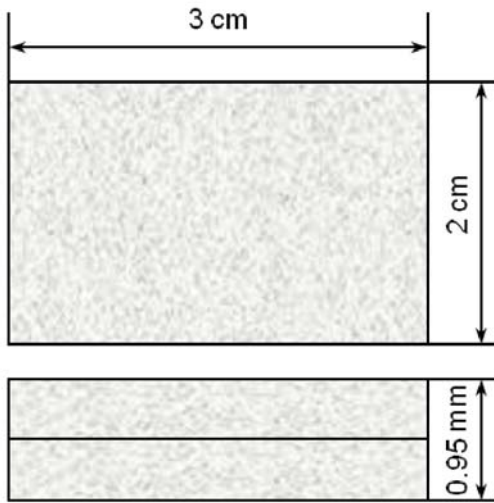


Figure 3.27: Detector pair.

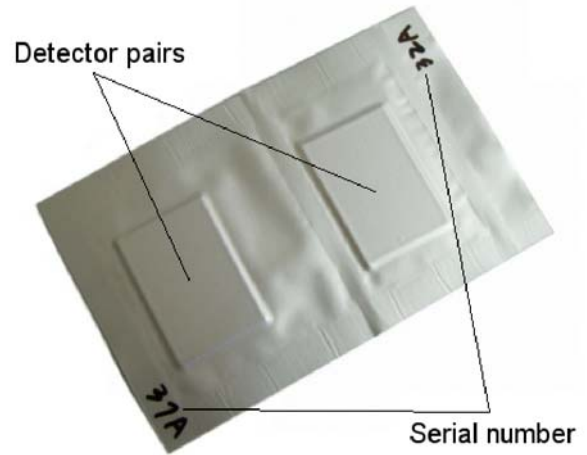


Figure 3.28: Detector package.



Figure 3.29: Vacuum device, which is used to evacuate the detector package.



Figure 3.30: Heating cabinet, which is used to maintain a constant temperature while an oscillating high voltage is applied.

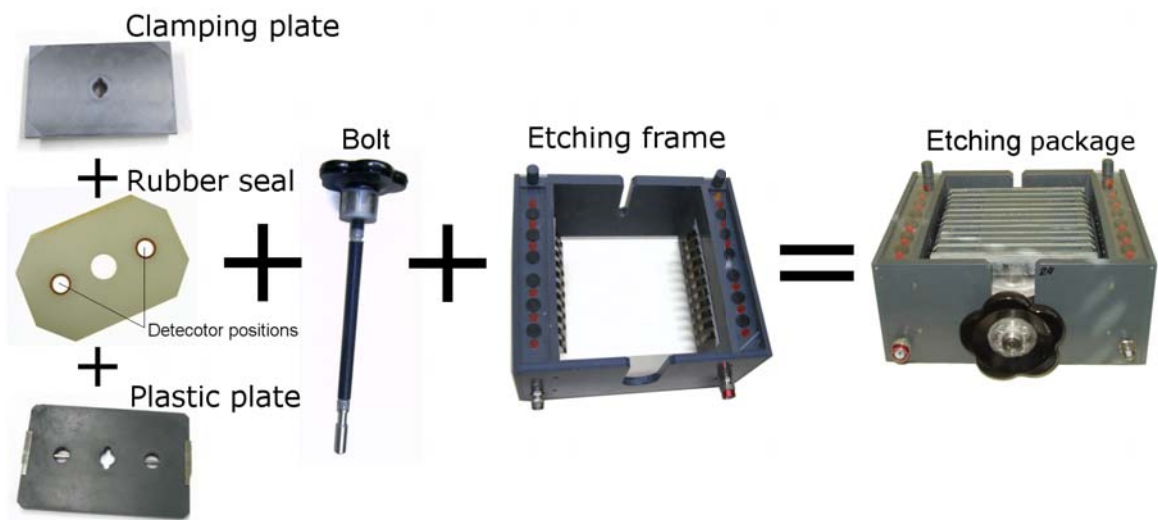


Figure 3.31: Etching component at KIT.

CE (5 h, 2000 V, 100 Hz) During the CE, reactions take place between the etchant and the material. As a result of different track etching velocity and bulk etching velocity, conical tracks are scooped out by the etchant. In addition, the low-frequency high-voltage induces treeing which can prevent tracks stemming from low energy recoils to be erased (Tommasino *et al.*, 1984).

ECE (1 h, 2000 V, 2 kHz) The ECE procedure enlarges the track size and thus increases the sensitivity of the vision. A cell is divided by SSNTDs into two parts, and one part contains an etchant. High-frequency high-voltage is connected to electrodes which are placed in each half of the cell. Due to the track cone being filled with conducting etchant, a very high electric field occurs at the cone tips. As the field oscillates, a series of dielectric breakdowns will be produced at the cone tips. The dielectric breakdowns lead to damages over a considerable volume around the track tips. The damages appear along the approximate direction of the electric field and create a tree structure, which produces a rather large visible spot close to the track tip. This procedure increases the size of tracks, which is very helpful for the track counting.

PE (0.5 h, 0 V, 100 Hz) After the ECE is finished, the etching device remains in the oven (see Figure 3.30) for half an hour without voltage applied. This leads to rounding of the tracks, which improves the recognition of the tracks.

Experiment at KIT

To verify the simulation results, an experiment was carried out in the KIT calibration laboratory. The irradiations were carried out at angles of 0, 15, 30, 45, 60, 75 and 90 degrees (with respect to the normal to the detector surface, see Figure 3.32 for the details of the experimental setup at KIT). The detectors were irradiated with a total dose of 2.76 mSv at a distance of 70 cm from the neutron source.

Lacking of special designed detector holders, a simple frame was constructed manually. Detectors were fixed on steel sticks, which can be turned for different neutron incident angles. The whole frame was connected by screws, and the detectors are fixed on sticks. The provisionality of the system affects the accuracy of the position and the angle determination.

As the activity of the Cf-252 source is rather low (2.06×10^6 Bq), the experiment took about 2 days. It is hard to get a high dose value.

Experiment at PSI

As the experimental results at KIT showed large errors, the experiment was improved. In collaboration with the PSI, a more precise experiment was carried out. All detectors were irradiated at PSI and etched at KIT.

The irradiations were carried out also at angles of 0, 15, 30, 45, 60, 75 and 90 degrees with respect to the normal to the detector surface (see Figure 3.33 for the details of the experimental setup at PSI). The detectors were irradiated with a total dose of 10 mSv at a

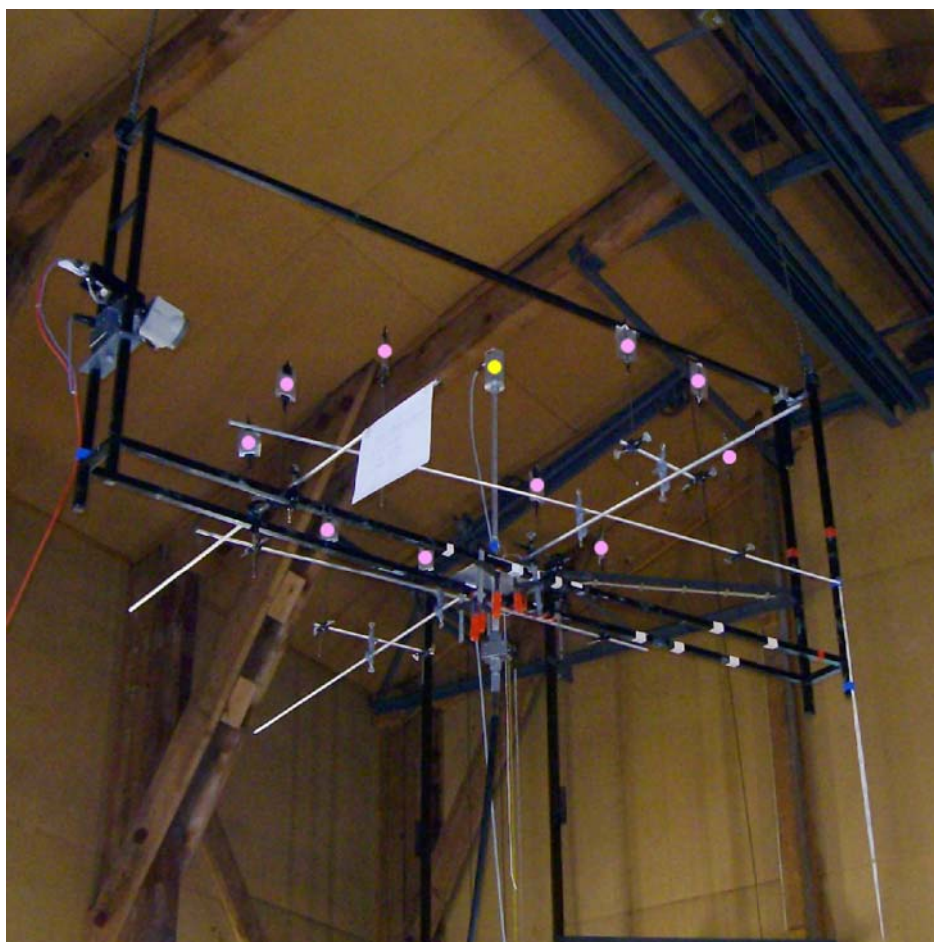


Figure 3.32: Experimental setup at KIT. Yellow dot: position of the Cf-252 source; pink dots: positions of the Makrofol detectors.

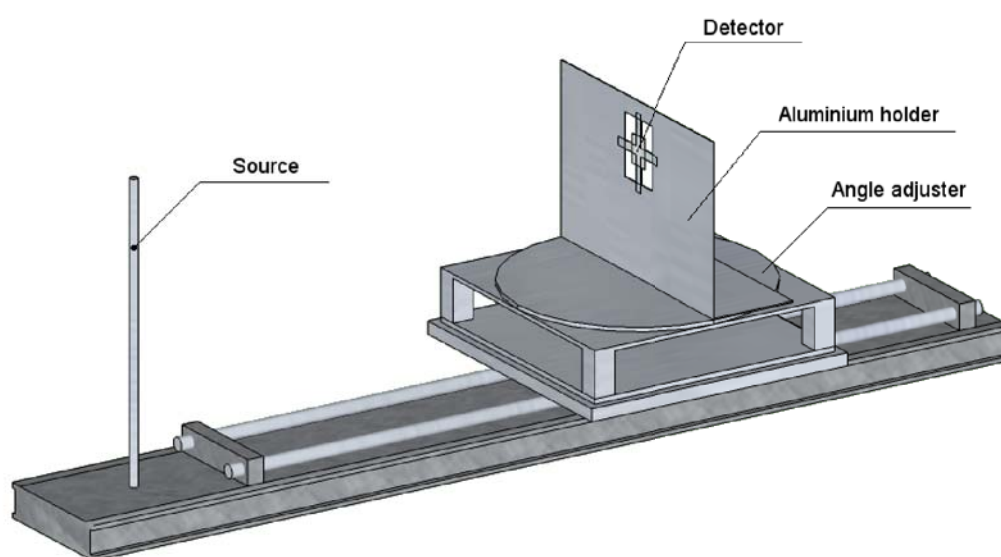


Figure 3.33: Experimental setup at PSI (Zhang *et al.*, 2011b).

distance of 1 m from the neutron source. A stronger Cf-252 neutron source (2.258×10^9 Bq), a dedicated stable detector holder and a precise angle adjustment device were used at PSI. The Makrofol detector package was fixed inside the window of a 1 mm thick aluminum holder. The Cf-252 source was placed in an aluminum standpipe at the same height as the detector. The distance between source and detector can be altered by moving the detector holder along the rails. The incident angle of the neutrons can be adjusted by rotating the round plate under the holder and a scale of angles on the plate allows to determine the incident angle quite precisely ($\pm 1^\circ$).

Auto Analyzing System

A digital image analysis system, which comprises a CCD camera, a microscope, a thickness measurer and an image processing program, was applied for track counting in the KIT solid state dosimetry laboratory (see Figure 3.34). By analyzing the shape of tracks, the analysis system can distinguish overlapping tracks (see Figure 3.35). At last, the track density and the track picture of the etched surface can be obtained.

Data Processing and Error Calculation

In the experiments, front detectors and rear detectors (with respect to the source) were analyzed separately. Besides the detectors irradiated with Cf-252, several "background" detectors also sealed in aluminized plastic foils were not irradiated. All detectors were etched together with the same two-step ECE etching procedure. The track densities were calculated as the difference of the readings of irradiated detectors and the readings of background detectors.

Suppose that x_N is the number of tracks on irradiated detectors, x_B is the number of tracks on unirradiated detectors, D is the track density caused by source neutrons. If the total area of irradiated detectors is a , and b for unirradiated detectors. The track density and relative error r can be calculated as follows:

$$D = \frac{x_N}{a} - \frac{x_B}{b} \quad (3.17)$$

$$\sigma_N \approx \sqrt{x_N} \quad (3.18)$$

$$\sigma_B \approx \sqrt{x_B} \quad (3.19)$$

$$\sigma = \sqrt{(\sigma_N/a)^2 + (\sigma_B/b)^2} \quad (3.20)$$

$$r = \frac{\sigma}{D} = \frac{\sqrt{(\sigma_N/a)^2 + (\sigma_B/b)^2}}{x_N/a - x_B/b} \approx \frac{\sqrt{x_N/a^2 + x_B/b^2}}{x_N/a - x_B/b} \quad (3.21)$$

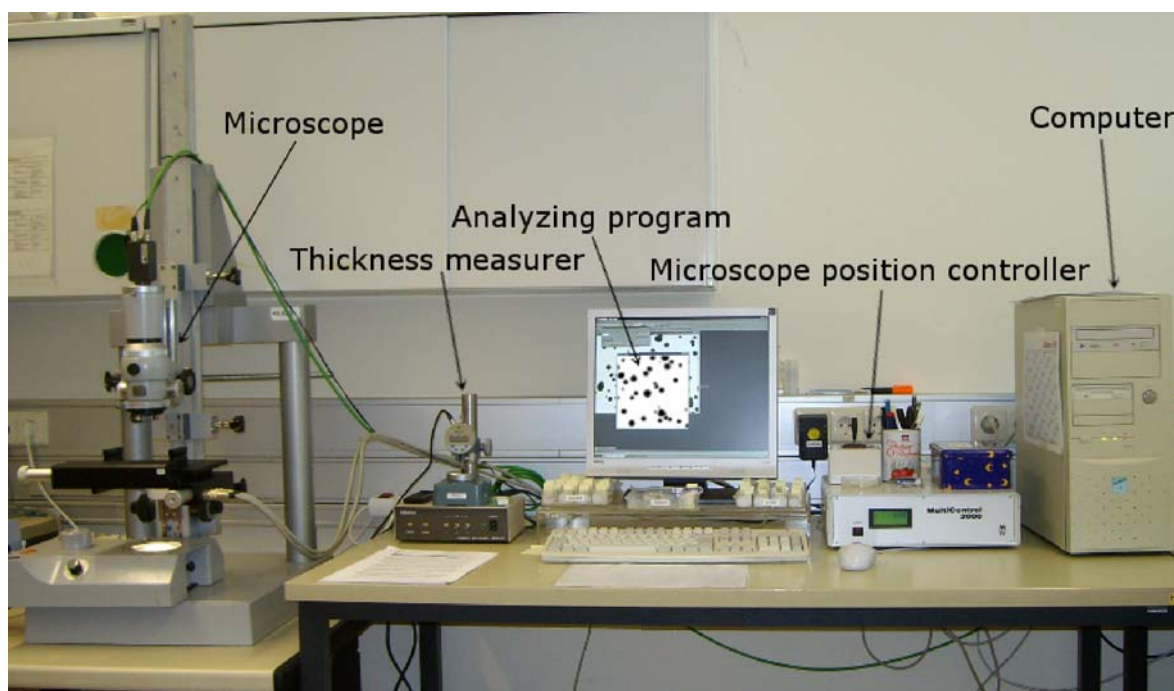


Figure 3.34: Auto analyzing system.

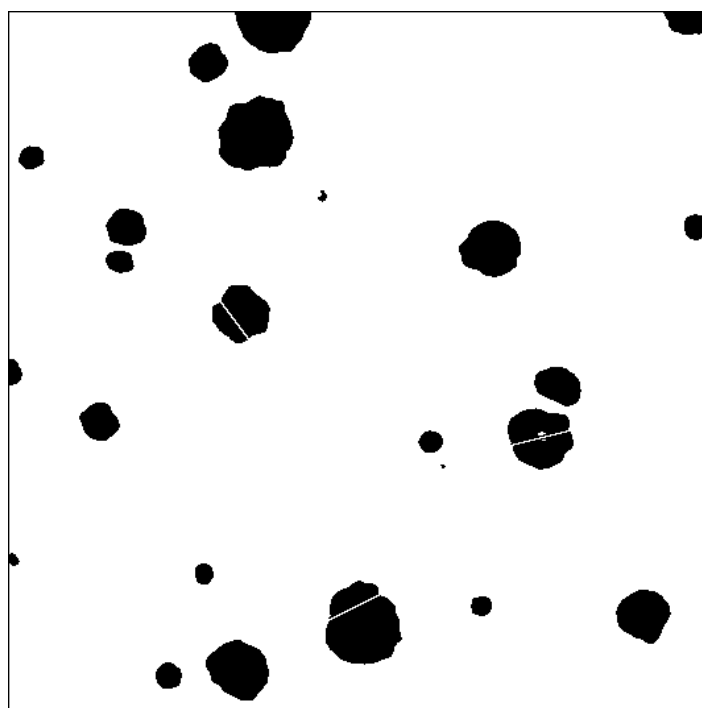


Figure 3.35: Enlarged experimental tracks observed with the analyzing system. Overlapping tracks can be distinguished by the analyzing software, as indicated by the "cutting" lines.

Chapter 4

Results and Discussion

The results of different simulations and experiments are shown in this chapter. Based on the results, analyses and discussions are made to compare data, methods and tools for the radiation field of the interim storage facility, the albedo dosimeter, and Makrofol dosimeters.

4.1 Radiation Field in the Interim Storage Facility

4.1.1 Surface Source Spectra

Figure 4.1 shows the calculated spectra at the outer surface of a CASTOR. The spectra calculated with a surface source are basically the same as those calculated with analog simulations. Since the simulation with the surface source performs the random sampling of particles (including energy, position, weight and direction) based on the information stored in the surface source file rather than duplicates the analog simulation, the spectra look a little bit different.

Taking into account the statistics, surface sources could be considered as the equivalent of original sources to the outside of the CASTOR.

4.1.2 Characteristics of the Radiation Field

4.1.2.1 Dose Rate Outside a CASTOR

Figure 4.2 shows the radial distribution of dose rates. The highest doses are stemming from the neutrons. The photon dose is lower than a quarter of the neutron dose. The contribution of neutron induced photons is rather small.

4.1.2.2 Distribution of Dose Rates in the Facility

Various arrangements of CASTORs in the facility were calculated to estimate the dose rates at several positions. A $m \times n$ array of CASTORs and seven sphere detectors of 30 cm were considered in the calculation (see Figure 4.3).

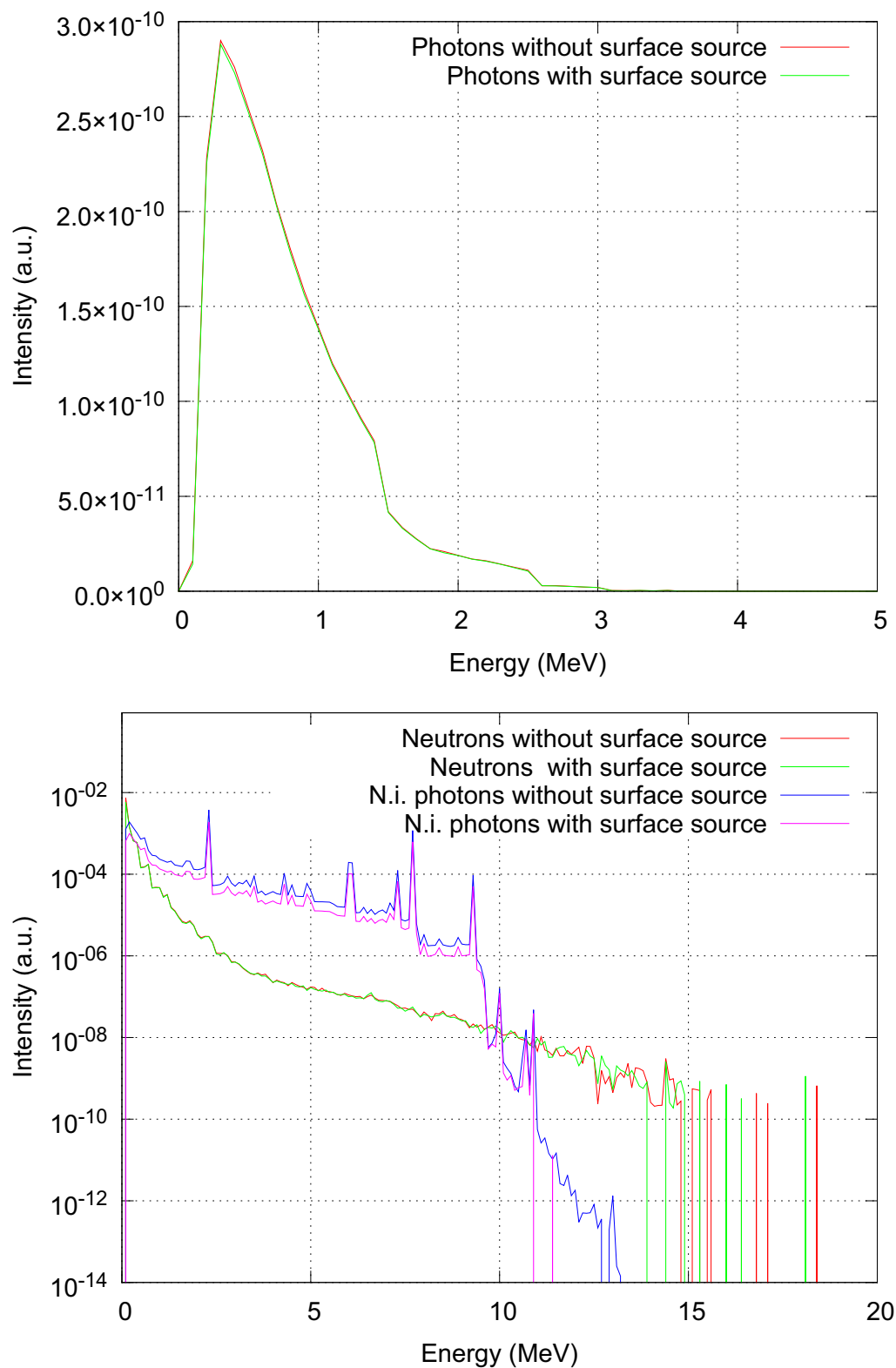


Figure 4.1: Calculated spectra of neutrons, photons and neutron induced (N.i.) photons at outer surface of a CASTOR.

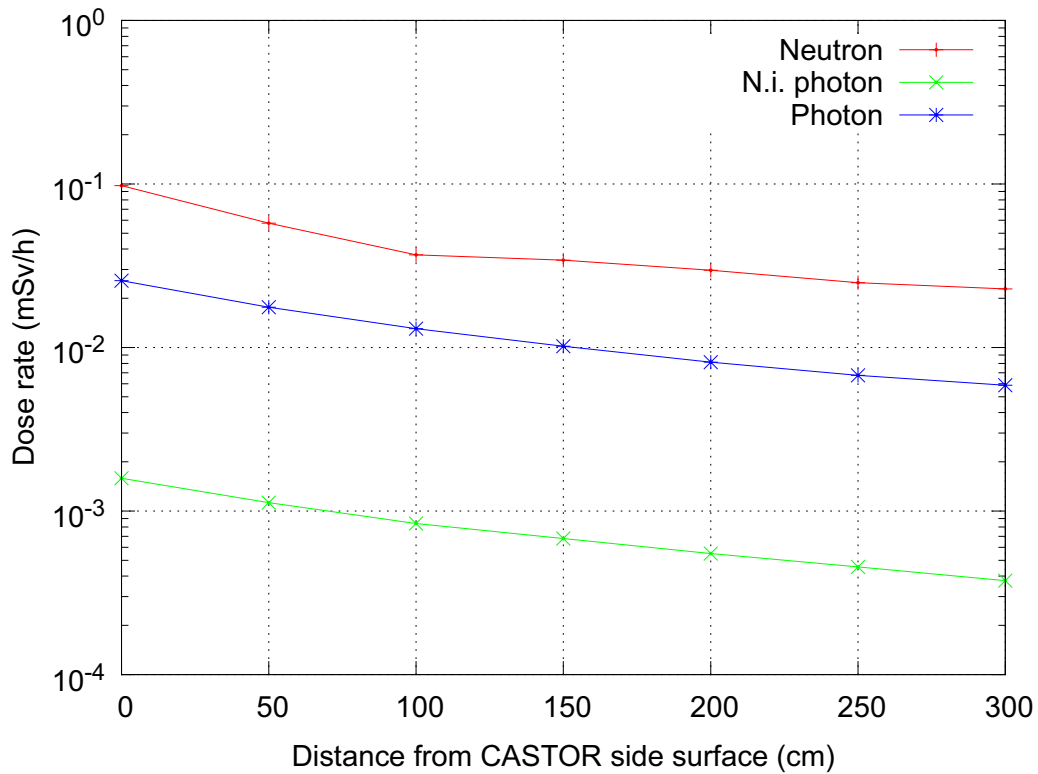


Figure 4.2: Calculated dose rates of neutrons, photons and neutron induced (N.i.) photons as a function of the distance from the CASTOR side surface.

Figure 4.4, 4.5 and 4.6 show the dose rates of neutrons, neutron-induced photons and photons at different detector locations. Different arrangements of CASTORs influence the dose rate distribution. For example the 4×2 array shows a higher dose rate than the 2×4 array at most detector positions. Therefore, the arrangement of CASTORs should be optimized in practice to produce the lowest dose rates at positions where workers usually would stay.

Figure 4.7 and Figure 4.8 show the calculated dose rate distributions in the interim storage facility with surface sources applied. As can be seen from the pictures, neutrons contribute more than photons to the dose rates. The maximum dose rates are lower than 0.2 mSv/h for neutrons and lower than 0.03 mSv/h for photons.

The dose rates inside CASTORs are higher than the dose rates outside, because the sources are located in the CASTORs. As a result of the application of the surface source, the dose rates inside the CASTORs are much lower than outside. Surface sources change the original source distribution, such as the particle position, so that the calculated dose rates inside the CASTORs are not correct (cf. white spots in Figure 4.7 and 4.8). Since only the dose rates outside the CASTORs are of interest in this work, surface sources are equivalent to the original sources to the outside of CASTORs. Therefore, the dose rates in the room can represent the actual values.

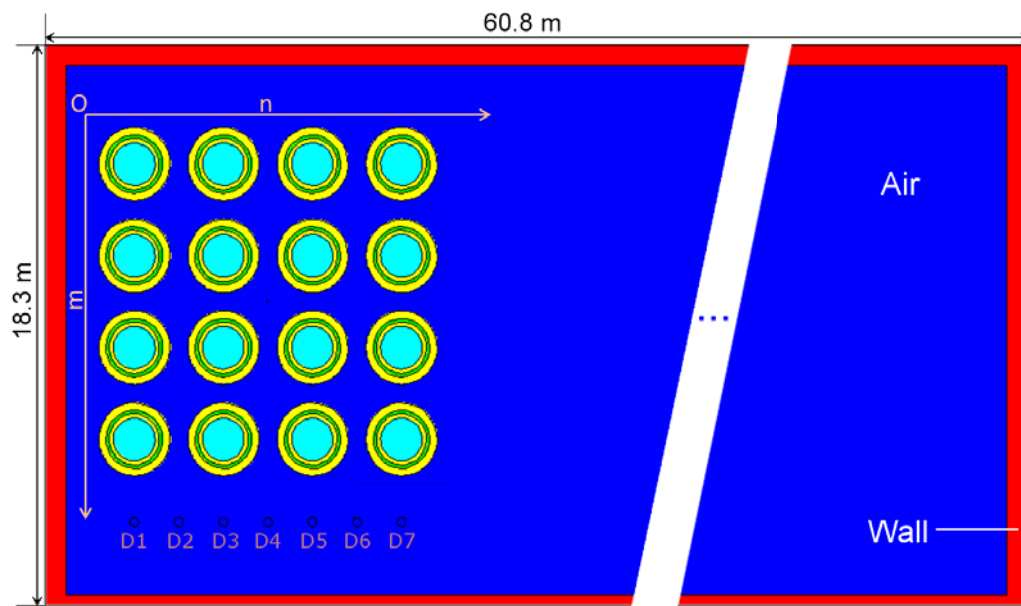


Figure 4.3: Arrangement of an array of $m \times n$ CASTORs (m and n are counted from the origin point O) and the positions of 7 sphere detectors D1 to D7.

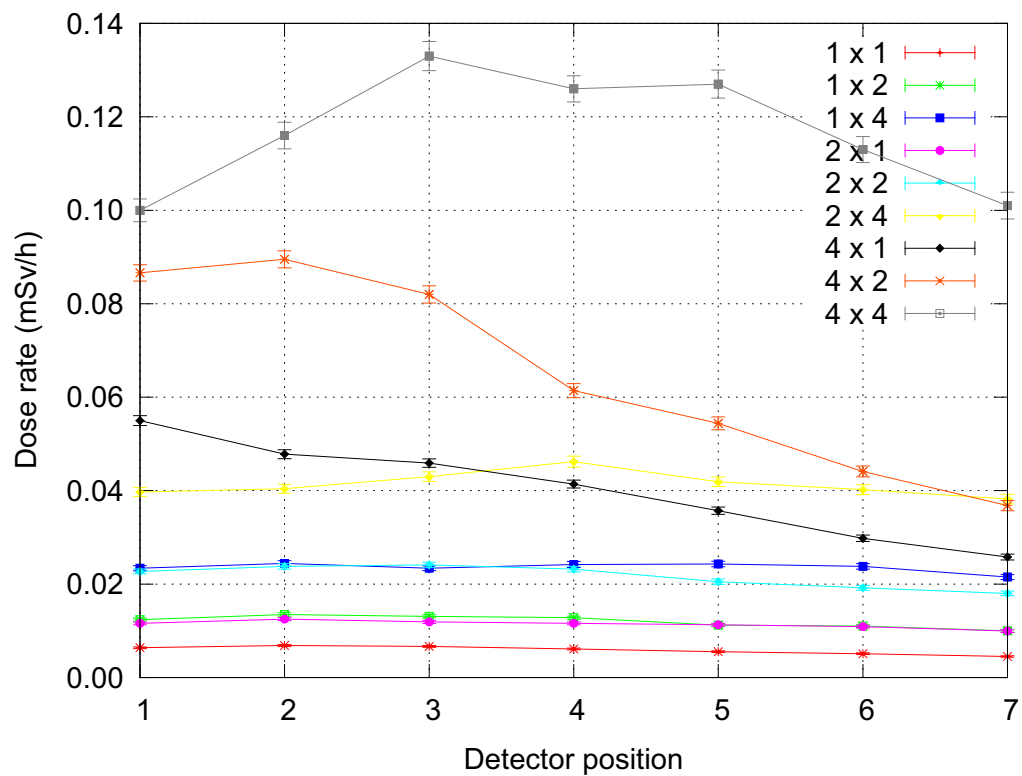


Figure 4.4: Neutron dose rates at different locations for arrays of $m \times n$ (see Figure 4.3).

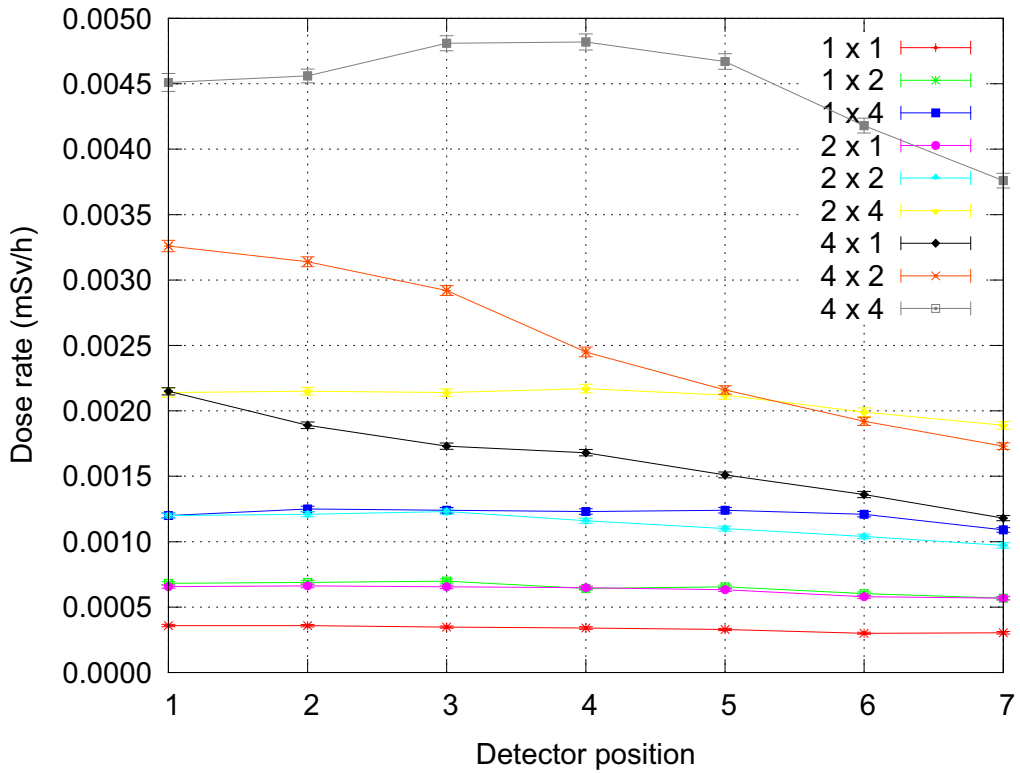


Figure 4.5: Neutron induced photon dose rates at different locations for arrays of $m \times n$ (see Figure 4.3).

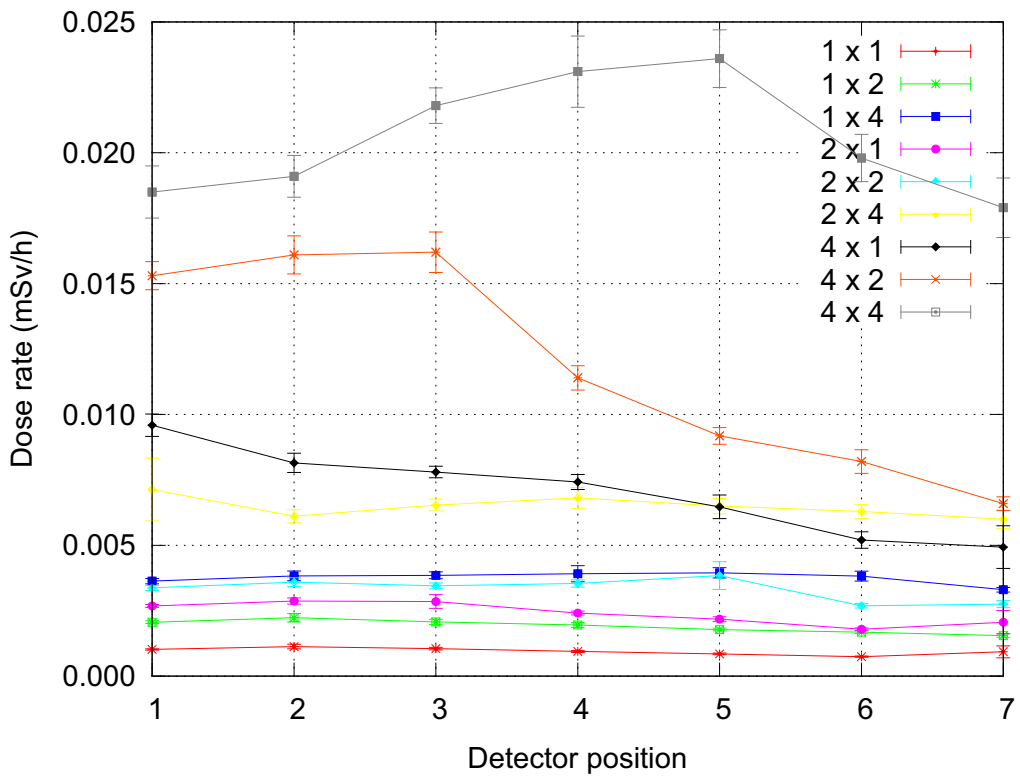


Figure 4.6: Photon dose rates at different locations for arrays of $m \times n$ (see Figure 4.3).

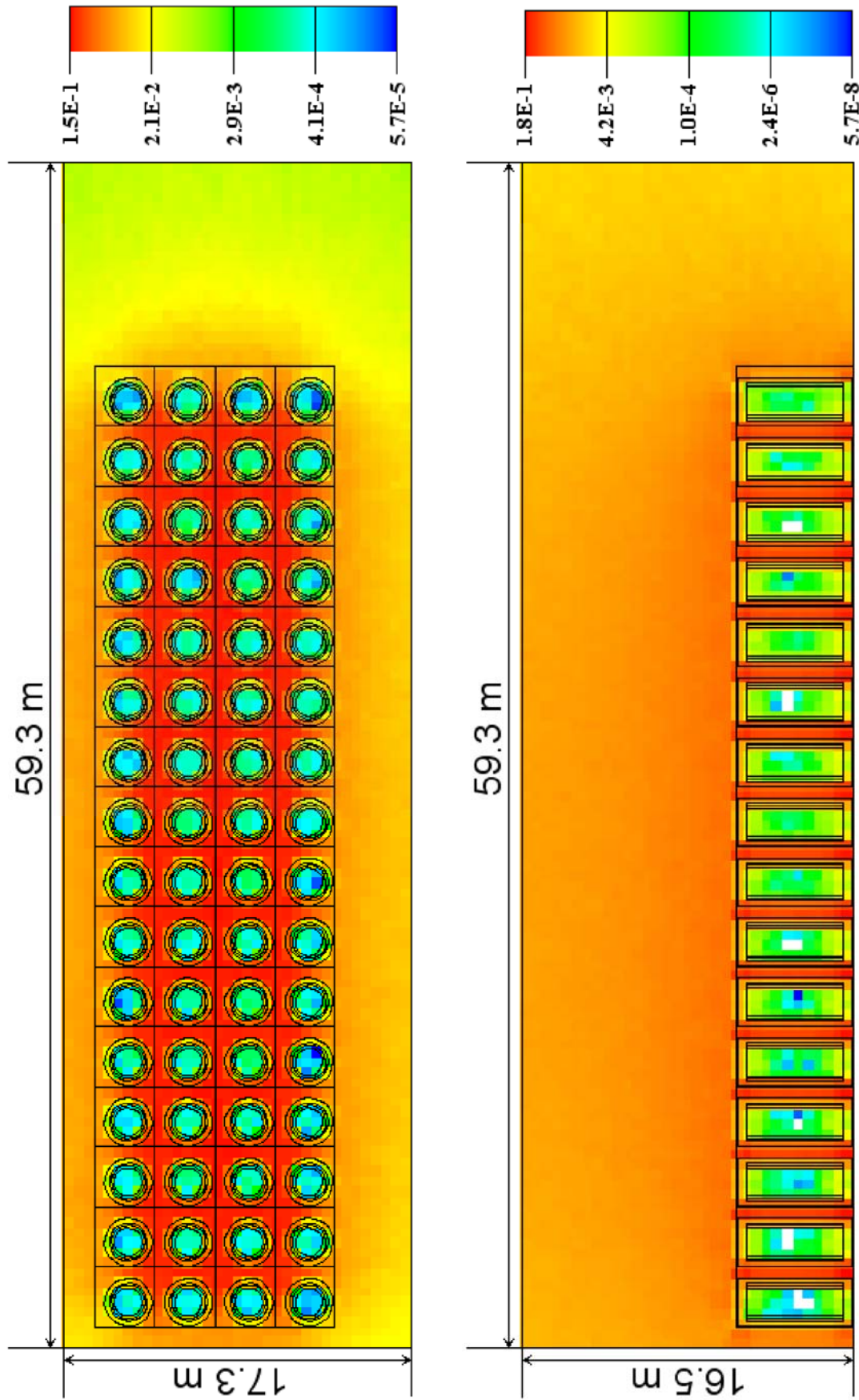


Figure 4.7: Calculated neutron dose rate distribution in the interim storage building loaded with 64 CASTORs (units: mSv/h).

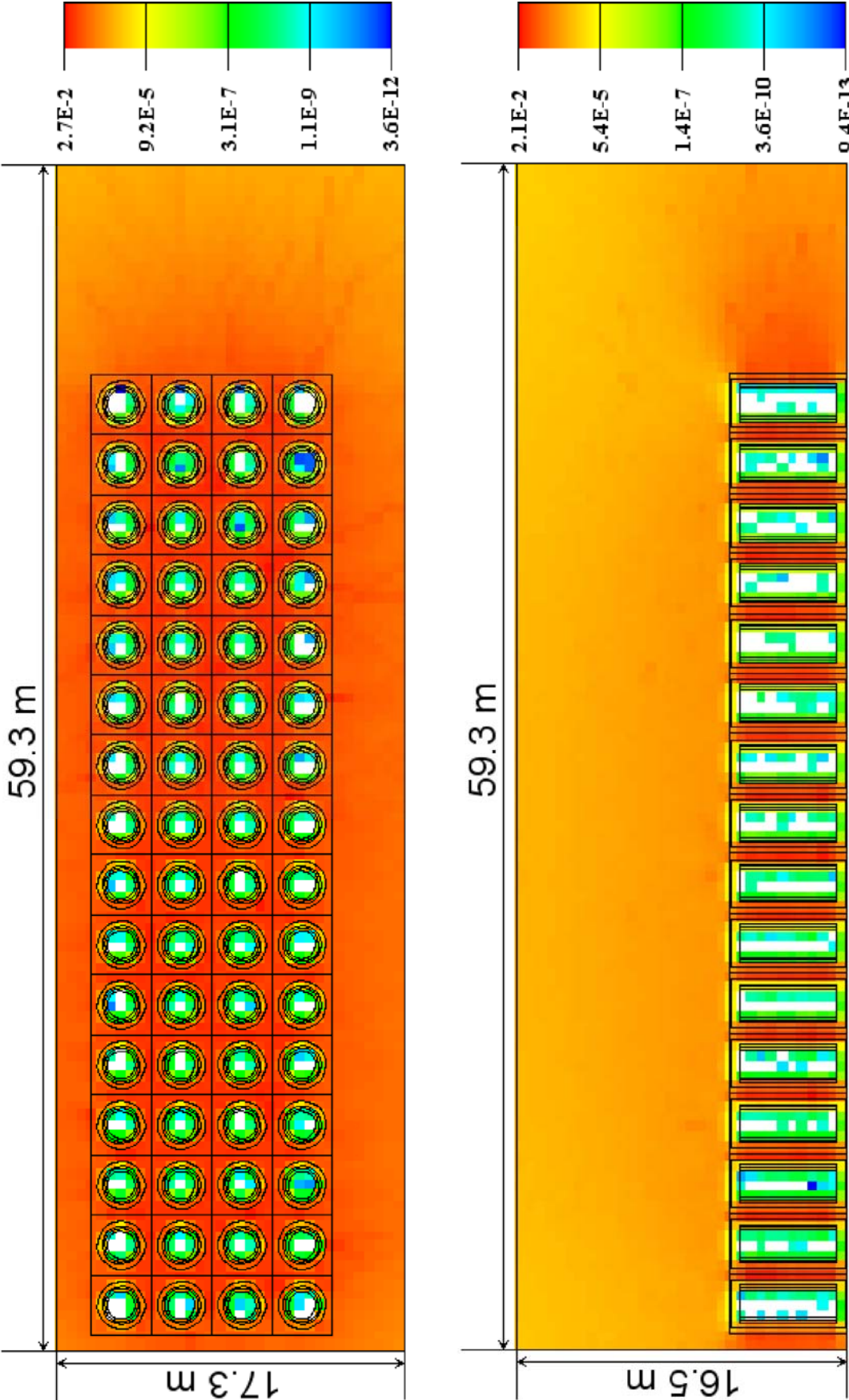


Figure 4.8: Calculated photon dose rate distribution in the interim storage building loaded with 64 CASTORs (units: mSv/h).

4.1.3 Performance of Calculations

4.1.3.1 Performance of Different Methods

Table 4.1: Performance of different methods.

Source particle*	Tally particle ⁺	Method	Computer time (min)	Relative error	FOM
Neutron	Neutron	Analog	7.60×10^3	7×10^{-4}	2.69×10^2
		Weight windows	5.63×10^3	4×10^{-4}	1.11×10^3
		Surface source	2.79×10^1	5×10^{-4}	1.44×10^5
	Gamma	Analog	7.60×10^3	1.2×10^{-3}	9.14×10^1
		Weight windows	5.63×10^3	4×10^{-4}	1.11×10^3
		Surface source	2.79×10^1	5×10^{-4}	1.44×10^5
Gamma	Gamma	Analog	4.33×10^4	8.67×10^{-2}	3.08×10^{-3}
		Weight windows	5.36×10^3	4.0×10^{-3}	1.17×10^1
		Surface source	3.72×10^2	4.0×10^{-3}	1.68×10^3

*The type of particles emitted from the fuel region

⁺The type of particle recorded by the detector

The performances of different simulation methods were tested with a representative CASTOR V/19. The figure of merit, FOM (see Section 2.2.3), is used to measure the efficiency of the calculations. As shown in Table 4.1, weight windows can improve the performance by a factor of about 5 for neutrons and by a factor of about 10 for neutron-induced gammas. For the gamma component of the CASTOR content, weight windows can improve the efficiency by a factor more than 2 orders of magnitude. When a surface source generated with weight windows is employed, more calculation time can be saved, because the transport of source particles inside the CASTOR is no longer needed.

4.1.3.2 Parallel Computing with Surface Sources

The surface source can reduce the calculation time for a set of CASTORs of the same type. However, sometimes a problem includes more than one type of CASTOR or different source terms. To investigate the performance of surface sources for this condition, a 4×4 array of CASTORs was tested with the normal source distribution and surface sources. The source information of a CASTOR V/19 was employed as representative CASTOR. For the analog simulation, the source is copied and translated to all 16 CASTOR positions (see Figure 4.9 left). The surface source is placed at the outer surface of one CASTOR (see Figure 4.9 right) and calculated 16 times at the different positions. The calculation time including surface source generation was multiplied by a factor of 16 to get the total time of the calculations. Calculations for both neutron and gamma source terms of the fuel inside the CASTOR were calculated. The total fluence over surfaces which surround the CASTOR array was used as the reference tally to compare the performance of the calculations.

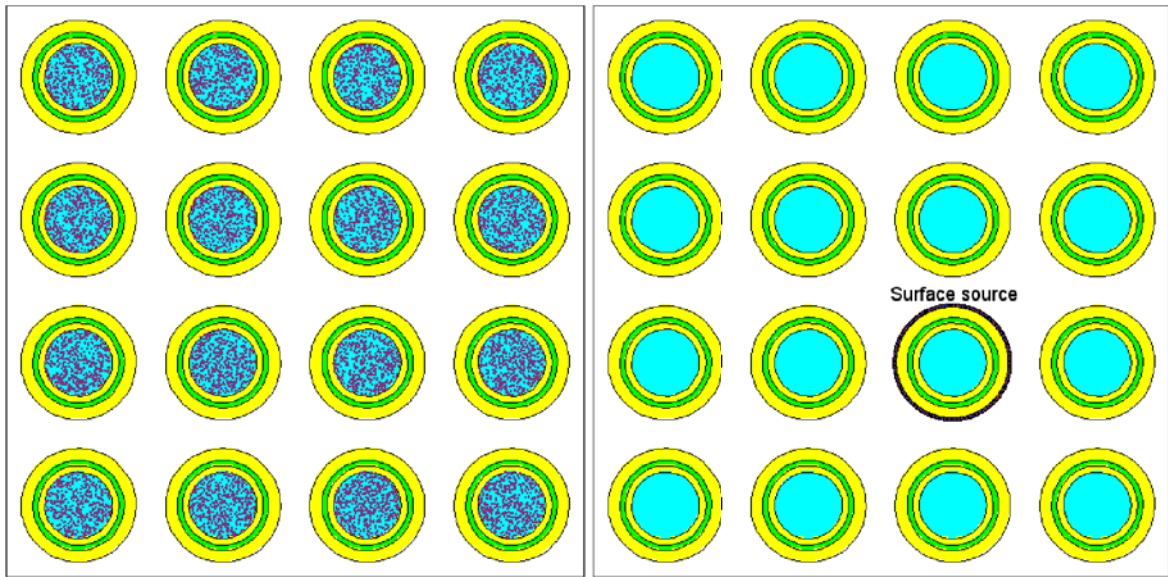


Figure 4.9: Distribution of source particles (points) with an analog simulation (left) and a surface source (right) on the cross section of an array of 4×4 CASTORs.

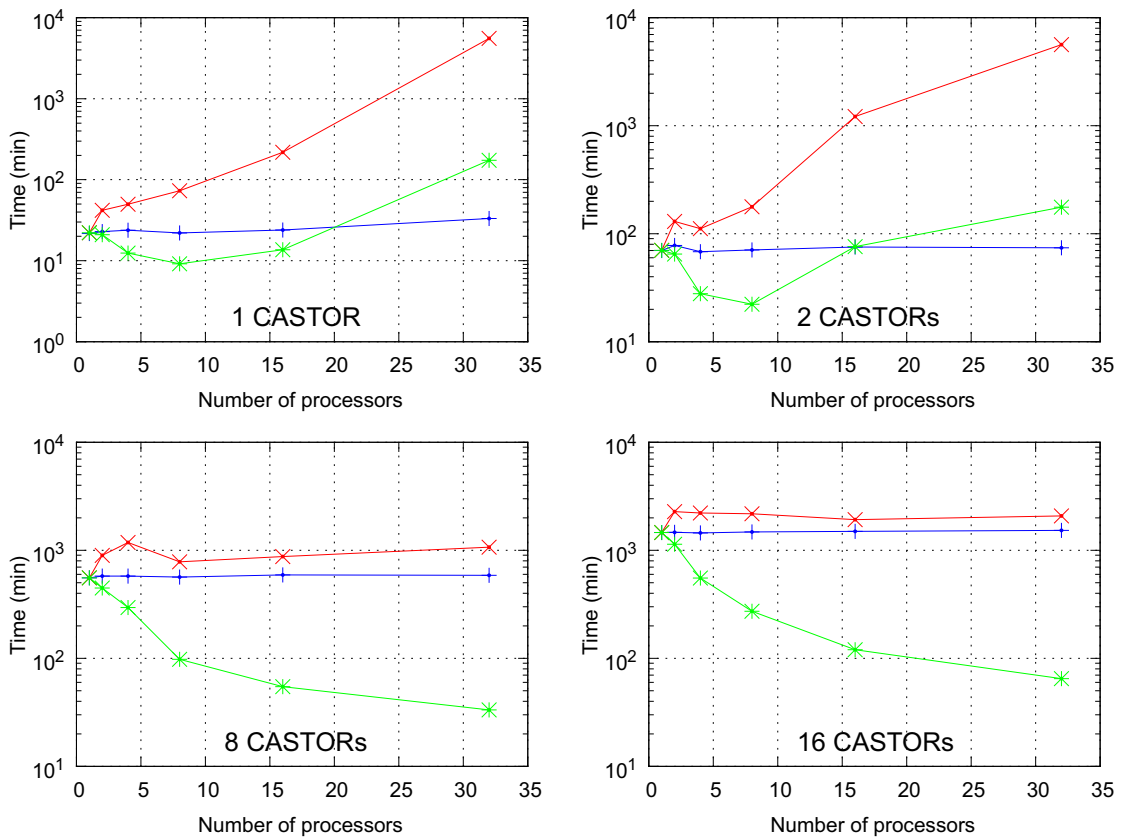


Figure 4.10: Total computer time (red), total calculation time (blue) and computer time per processor (green) as a function of the number of processors for different numbers of CASTORs, obtained with neutron source particles.

Table 4.2: Results of analog simulation and surface sources for 16 types of CASTORs.

Source particle*	Tally particle ⁺	Method	Computer time (min)	Relative error	FOM
Neutron	Neutron	Analog	1.06×10^5	3×10^{-4}	1.05×10^2
		Surface source	1.44×10^5	1.7×10^{-4}	2.41×10^2
	Gamma	Analog	1.06×10^5	7×10^{-4}	1.93×10^1
		Surface source	1.44×10^5	2.21×10^{-4}	1.42×10^2
Gamma	Gamma	Analog	8.99×10^3	3.39×10^{-1}	9.71×10^{-4}
		Surface source	1.24×10^5	3.60×10^{-3}	6.23×10^{-1}

*The type of particles emitted from the fuel region

⁺The type of particle recorded by the detector

Table 4.2 shows the results of different methods for different sources and tallies. For 16 types of CASTORs, surface sources can improve the calculation efficiency by more than two orders of magnitude for gamma source particles, because only a small part of gammas can go through the wall of the CASTOR. As neutrons can penetrate the wall more easily, the performances for neutrons and neutron-induced gammas are improved less by surface sources for the neutron source.

Figure 4.10 shows the results of parallel computing with surface source generated with a neutron source. With the increase of processors, the total computer time, which is the sum of the computer time of all processors, increases rapidly for 1 and 2 CASTORs while the calculation time, which is a part of total computer time used for the calculation, stays almost the same. The computer time per processor, i.e. the wall clock time or the time needed to wait to get results, first decreases then increases for 1 and 2 CASTORs, and decreases for 8 and 16 CASTORs. Depending on the number of CASTORs involved, more processors do not always make the calculation faster. For 2 CASTORs, 8 processors would be a better choice.

The total calculation time increases with the number of CASTORs, because the geometry becomes more complex, and a higher number of source events is needed. For the same geometry, different number of processors and network conditions will not change the calculation time but the communication time through MPI between master and slave processes.

For a specific problem, too many processors could slow down the calculation, because the time of reading the surface source data takes longer than the time of the calculation on each processor. The performance is strongly dependent on many factors such as processor architecture, the number of computer nodes those processors locate, net work connection, program efficiency and so on. The calculation time and the communication time should be balanced to get the best performance. Each problem could have an optimum number of processors.

4.2 Dosimeters

4.2.1 Albedo Dosimeter

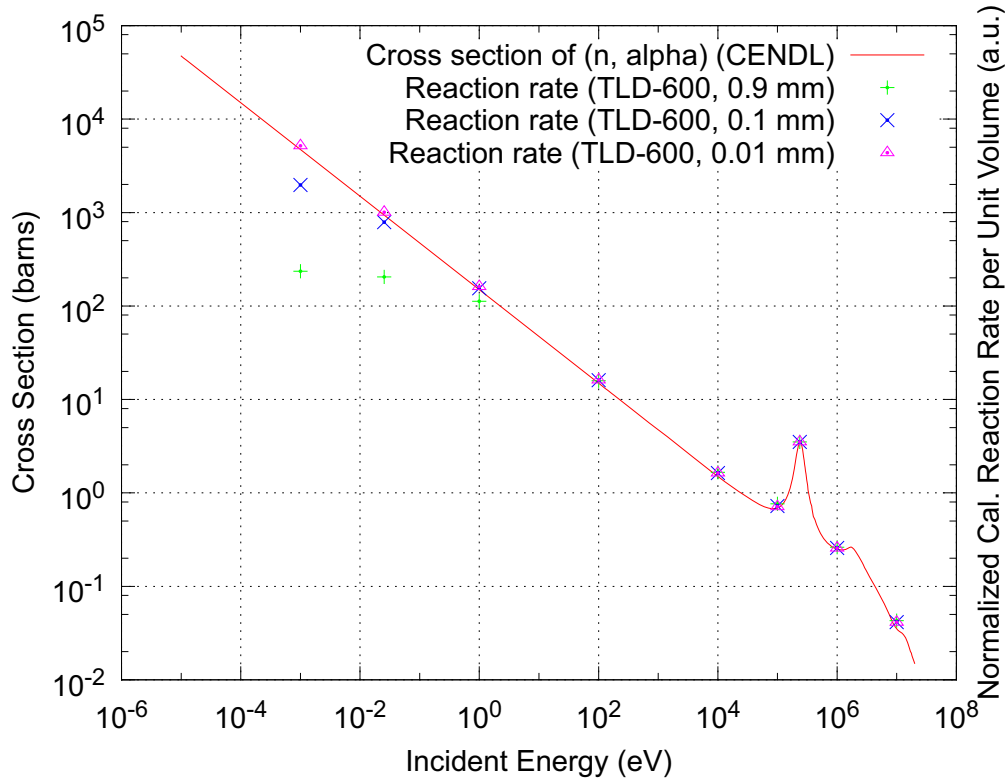


Figure 4.11: Energy dependent cross section of (n, α) reactions in Li-6 and calculated (n, α) reaction rates (normalized) in TLD-600 detectors of different thicknesses.

4.2.1.1 Calculated Reaction Rate

The number of (n, α) reactions can be obtained in MCNPX using the F4 tally (fluence averaged over a cell) together with FM card (see Appendix D). The FM card converts the fluence to the number of specific reactions.

A TLD-600 detector, which mainly comprises Li-6 and fluorine, is used in the calculations. Figure 4.11 shows the calculated (n, α) reaction rates and the experimental cross-section data from CENDL¹. All calculated values are normalized to the peak of the cross section curve at about 0.24 MeV.

As can be seen from the picture, calculated values agree well with the cross section data for energies above 100 eV. In the low energy region, the thinner detectors show a better agreement than the thicker detectors. The reason is that all low-energy neutrons are stopped in a very thin layer in the front of the detector due to the very high cross-section at low energies. For low-energy neutrons, a thicker detector does not increase the number of reactions

¹Chinese Evaluated Nuclear Data Library

but the volume. Since the investigated reaction rates represent the number of reactions per unit volume, the rates for thicker detectors are lower than those for thinner detectors.

Neglecting the effect of the detector thickness, the results of MCNP show a good agreement with the experimental cross section data. Since the neutron reading of TLD detectors is approximately proportional to the number of (n, α) reactions, this calculation method was used for calculating the response of albedo dosimeters in the interim storage facility.

4.2.1.2 Scattering Effect

In a neutron field, scattering usually exists and can influence the field properties significantly. Since albedo dosimeters are more sensitive to low energy neutrons, the neutron scattering can make a big difference to the response.

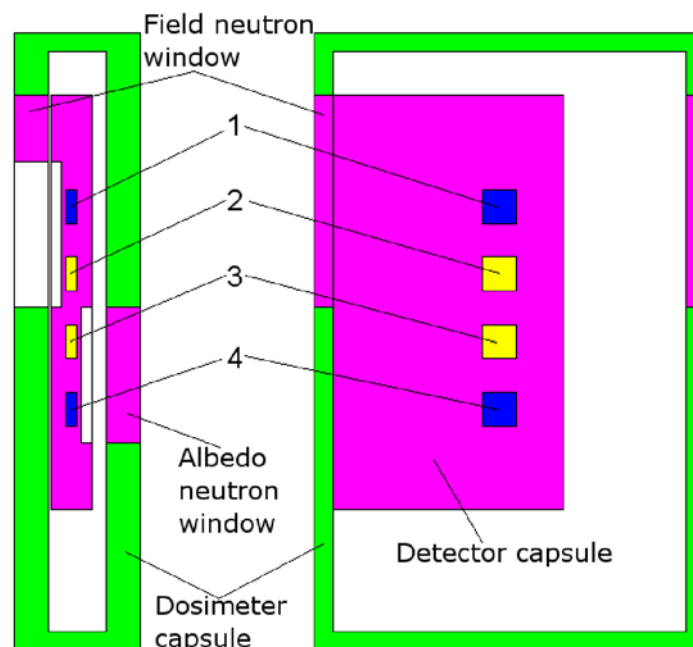


Figure 4.12: Positions of TLD-600 detectors (1 and 4) and TLD-700 detectors (2 and 3), please refer to Figure 3.14.

To investigate the effect of scattering, the albedo dosimeter model together with the Cf-252 source (see Figure 4.12) was placed at different heights from the floor (see Figure 4.13) in the calculations. The calculated reading ratios of field neutrons to albedo neutrons are shown in Figure 4.14. The reading ratios vary by a factor of up to 3. At different heights, the neutron fields are much different due to the floor scattering. As can be seen from Figure 4.15, the readings of detectors change with the height. As Cf-252 is a neutron source, the readings of TLD-700 detectors are 3 orders of magnitude lower than those of TLD-600 detectors.

In practice, the neutron scattering can be generated by floor, roof, walls or other objects. To obtain accurate dose values, the scattering needs to be considered.

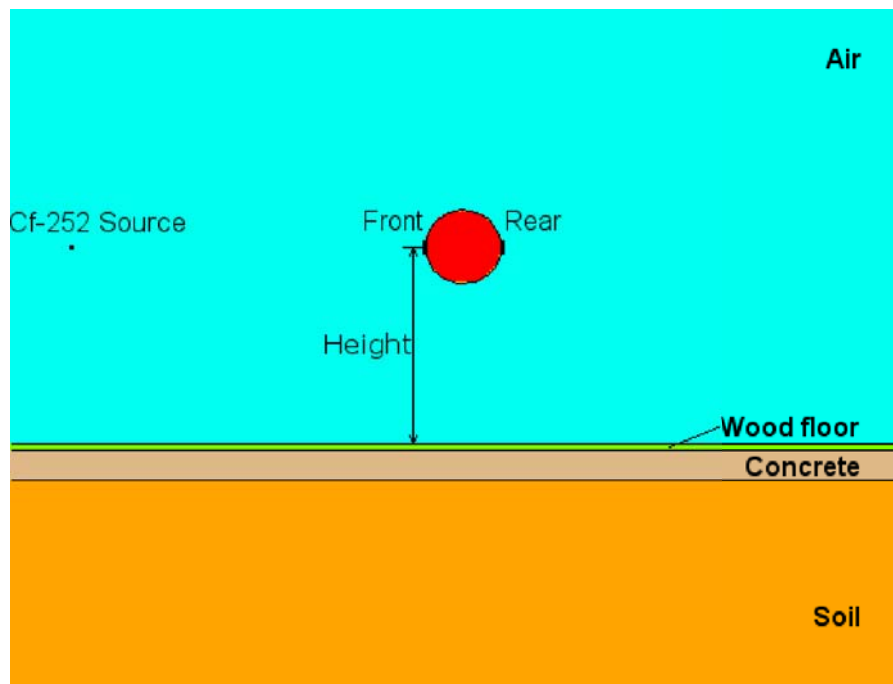


Figure 4.13: Position of the front and rear dosimeters above the floor in a low back scattering room. Red: ICRU sphere, cyan: air, green: wood, tan: concrete, and orange: soil.

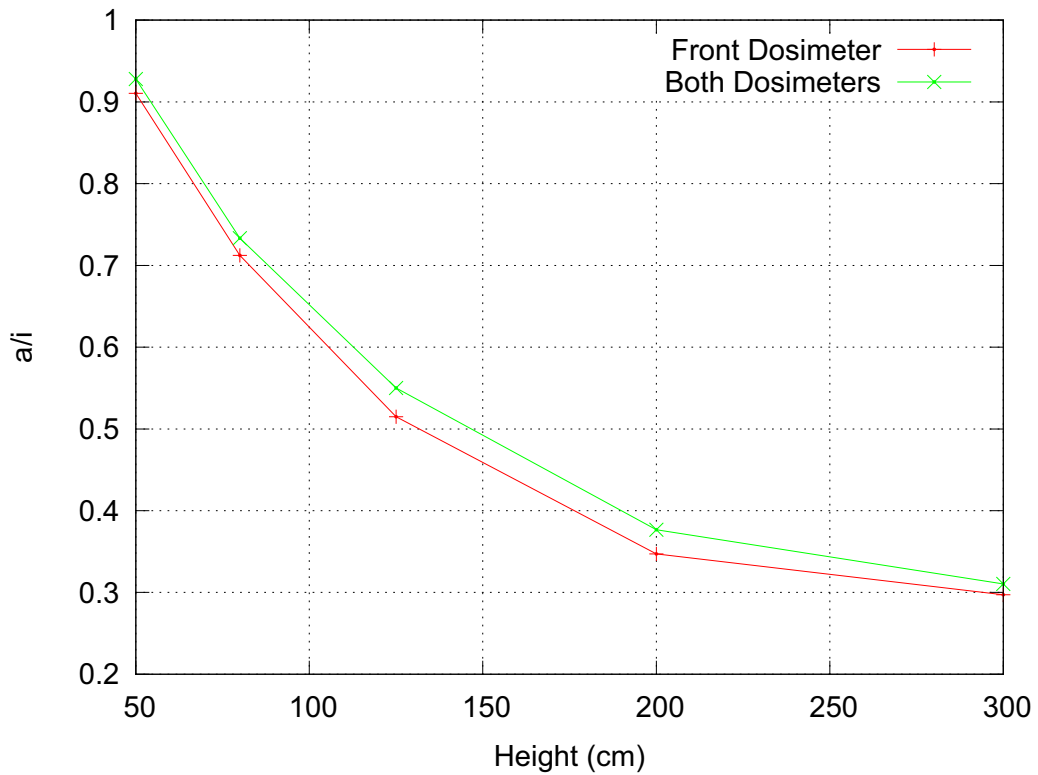


Figure 4.14: Reading ratios (a/i) of field neutrons (a) to albedo neutrons (i) at different heights using only front dosimeter or the average of both front and rear dosimeters (see Figure 4.13).

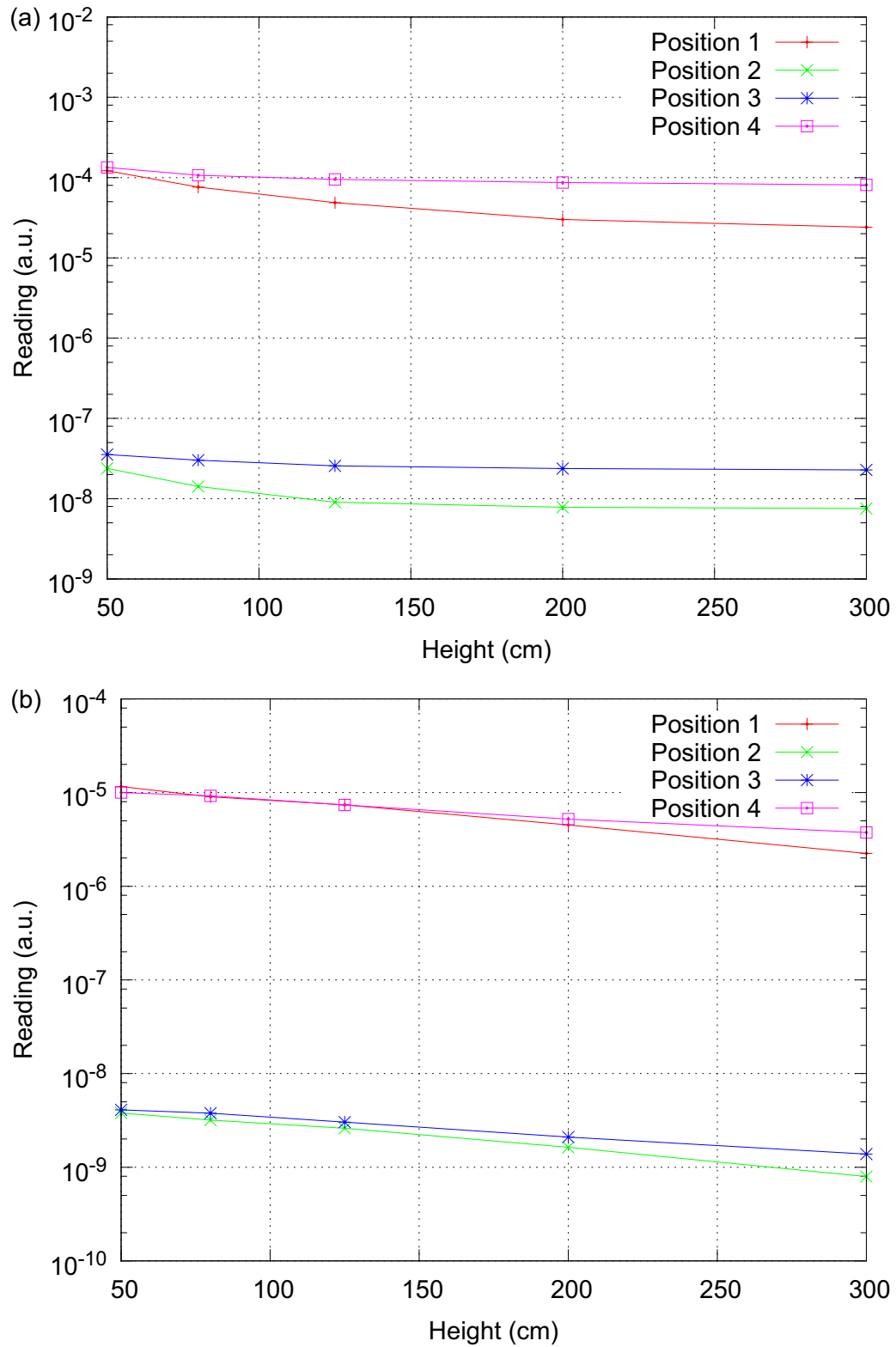


Figure 4.15: Simulated neutron readings of (a) front detectors and (b) rear detectors at different heights (see Figure 4.12 for the positions).

4.2.1.3 Response in the Interim Storage Facility

To correct for local and workplace dependent changes of the albedo response, Burkhardt and Piesch classified various neutron fields into four categories in their work (Burkhardt and Piesch, 1988), that is:

- (N1) Reactors and accelerators, heavy shielding
- (N2) Fuel element cycle, criticality, low shielding
- (N3) Radionuclide sources
- (N4) Accelerators for research inside shielding

Constant calibration factors are used for N1 and N2. For N3 and N4, the reading ratio of field neutron to albedo neutron is considered.

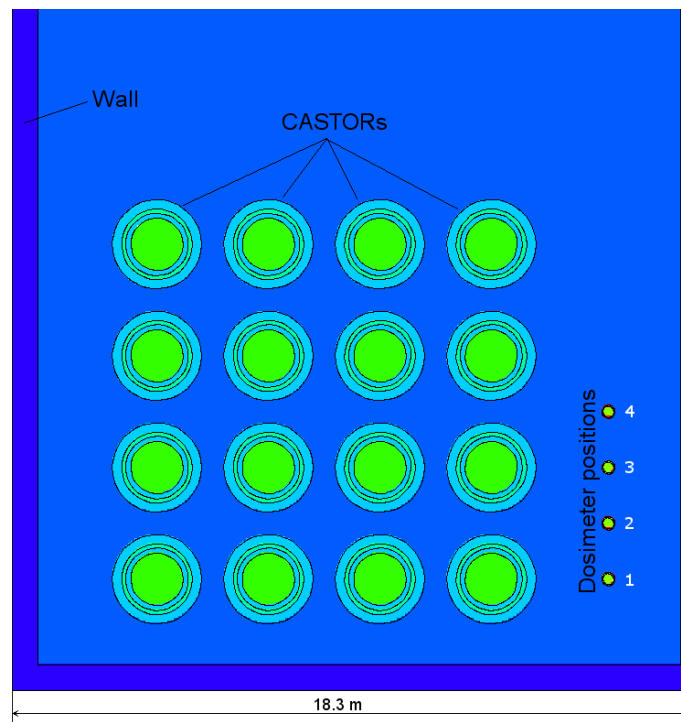


Figure 4.16: Positions of albedo dosimeters.

The appropriate calibration category was determined with Monte Carlo simulations for the high-scattering neutron field in the interim storage facility. The calculation results of 4 different albedo dosimeter pairs (see Figure 4.16), which are placed 1.3 meters above the floor, are shown in Figure 4.17 together with the results of Burkhardt and Piesch (Burkhardt and Piesch, 1988; Piesch and Burkhardt, 1988b).

The response $R_n(i)$ is defined as the ratio of the reading $M(i)$ of the albedo detector (i) (see Figure 4.17) to the neutron dose equivalent H_R :

$$R_n(i) = M(i)/H_R \quad (4.1)$$

The MCNP model of a Cf-252 point source in the calibration room at KIT was used in the calculation as a reference field. The calibration room is 11.9 m long, 8 m wide, about 8 m high, and build with low neutron scattering materials, such as wood. The Cf-252 source was placed 1.2 m above the floor to reduce the scattering.

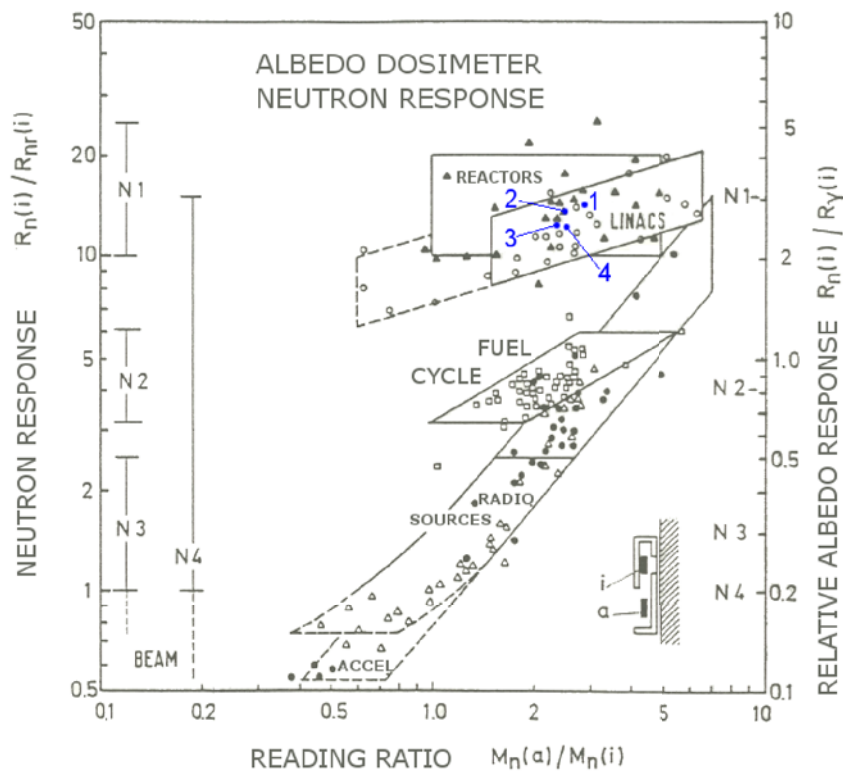


Figure 4.17: Measured and calculated neutron response of an Alnor albedo TLD dosimeter against the reading ratio of field neutrons $M(a)$ to albedo neutrons $M(i)$. Calculated results from this work are shown with blue dots. Measured results are taken from ref. (Piesch and Burghardt, 1988b). $R_{nr}(i)$ is the response of detector in the reference field while $R_\gamma(i)$ is the response to a reference gamma source (Cs-137).

As shown in Figure 4.17, the calculated results are similar to the measured results in the fields of reactors and linear accelerators. Thus the radiation field in the interim storage facility can be classified as N1, and the calibration factor for N1 can be applied for the field. To extend this statement to be valid in general for reactors and interim storage facilities, more information and investigations are needed.

4.2.2 SSNTD

4.2.2.1 Thickness of Etched Layer

During the etching, not only latent track pits are etched but also the rest part of the detector which is in contact with the etchant. After the etching, a layer of a certain thickness was removed by the etchant. The thickness of the removed layer is dependent on the composition of the etchant, etching temperature, detector material, duration of the etching and so on.

In order to get the information about the thickness of the layer etched away, 20 Makrofol detectors were etched with the routine two-step ECE procedure in the KIT solid state dosimetry laboratory. The thicknesses of Makrofol detectors before and after the etching were measured (see Table 4.3). Based on the measured data, a layer of average thickness of 35.8

Table 4.3: Thicknesses of Makrofol detectors.

Detector	Thickness before etching (mm)	Thickness after etching (mm)	Thickness etched (mm)
1	0.465	0.429	0.036
2	0.459	0.423	0.036
3	0.461	0.425	0.036
4	0.469	0.432	0.037
5	0.469	0.434	0.035
6	0.462	0.426	0.036
7	0.466	0.430	0.036
8	0.463	0.428	0.035
9	0.466	0.432	0.034
10	0.460	0.425	0.035
11	0.460	0.425	0.035
12	0.466	0.429	0.037
13	0.457	0.422	0.035
14	0.466	0.430	0.036
15	0.466	0.432	0.034
16	0.463	0.427	0.036
17	0.462	0.426	0.036
18	0.465	0.429	0.036
19	0.468	0.431	0.037
20	0.457	0.419	0.038
Average	0.4635 ± 0.0037	0.4277 ± 0.0038	0.0358 ± 0.0010

μm will be removed from the Makrofol detector after the etching with the routine two-step ECE procedure. This value is used as the maximum counting thickness in the simulations. Since only tracks in the removed layer can be etched and tracks at the very first layer could be removed, the thickness of the effective counting layer should be smaller than the thickness of the removed layer.

4.2.2.2 Tracks at Different Angles

Different incident angles of neutrons will result in different angular distributions of heavy recoils which influence the detector response.

Figure 4.18 shows the track pictures of different neutron incident angles, and the track densities are given in Table 4.4 which are based on the data in Appendix J. As can be seen, the track density becomes lower when the incident angle increases. The incident angle plays an important role in the response of Makrofol detectors.

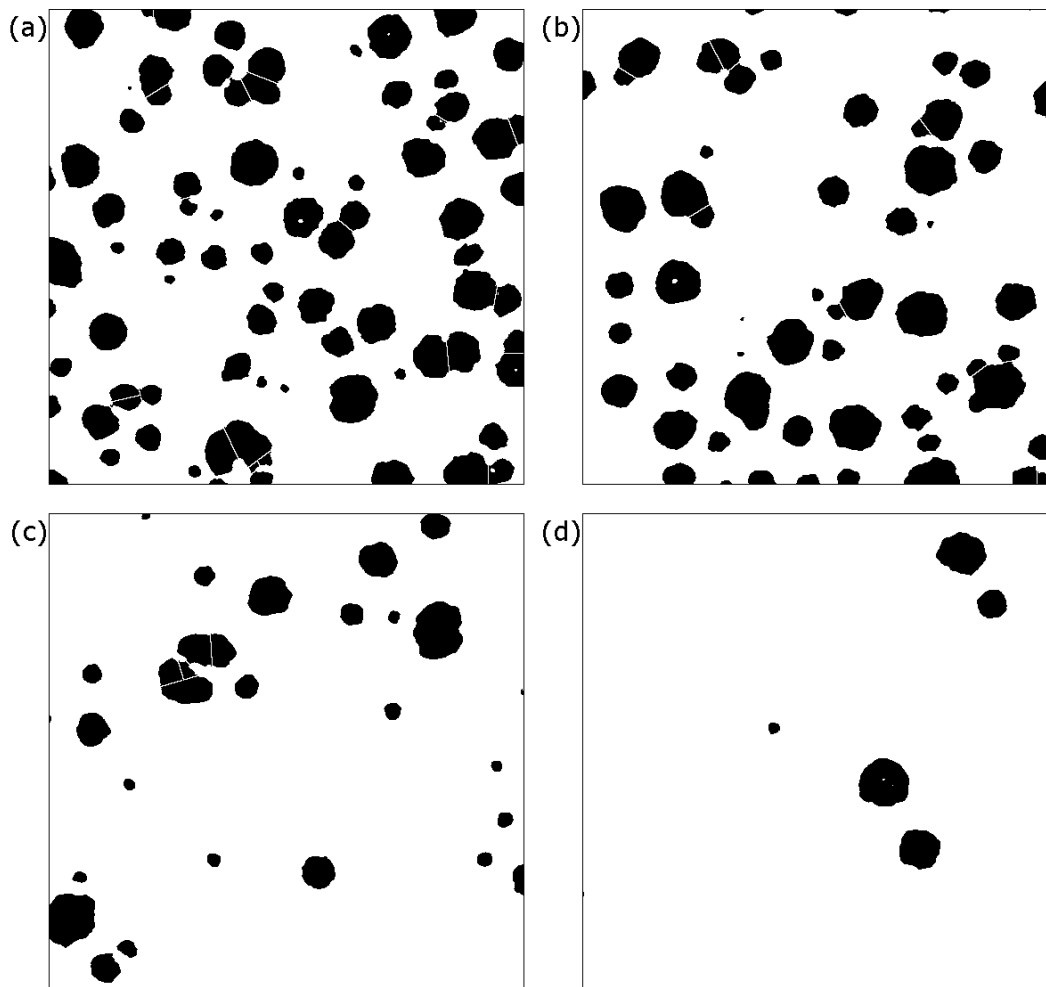


Figure 4.18: Track pictures with neutron incident angles of (a) 0, (b) 30 (c), 60 and (d) 90 degrees in the experiment. The track density decreases with the increasing of the incident angle of neutrons.

Table 4.4: Experimental results*.

Neutron incident angle (deg)	Exp. at KIT		Exp. at PSI	
	Track density (cm^{-2})	Relative error	Track density (cm^{-2})	Relative error
0	330.64	5.13%	811.01	2.24%
15	321.24	5.21%	776.96	2.29%
30	282.89	5.60%	654.45	2.51%
45	206.96	6.68%	505.34	2.87%
60	100.51	10.33%	290.86	3.87%
75	31.62	23.21%	95.56	7.43%
90	29.28	24.64%	40.38	13.30%

* Detectors at the rear side of the detector pairs (with respect to the Cf-252 source) were used for the track counting.

4.2.2.3 Restricted Energy Loss

Based on the method mentioned in Section 3.5.2.3, the RELs for carbon and oxygen were calculated. In the low energy region (< 1.2 MeV for carbon; < 1.6 MeV for oxygen), RELs were calculated with the SRIM program. In the higher energy region, RELs were computed with the Bethe-Bloch formula.

As can be seen from Figure 4.19, the results of the SRIM code and Bethe-Bloch formula are compatible at the energy boundary, no significant discontinuity is observed.

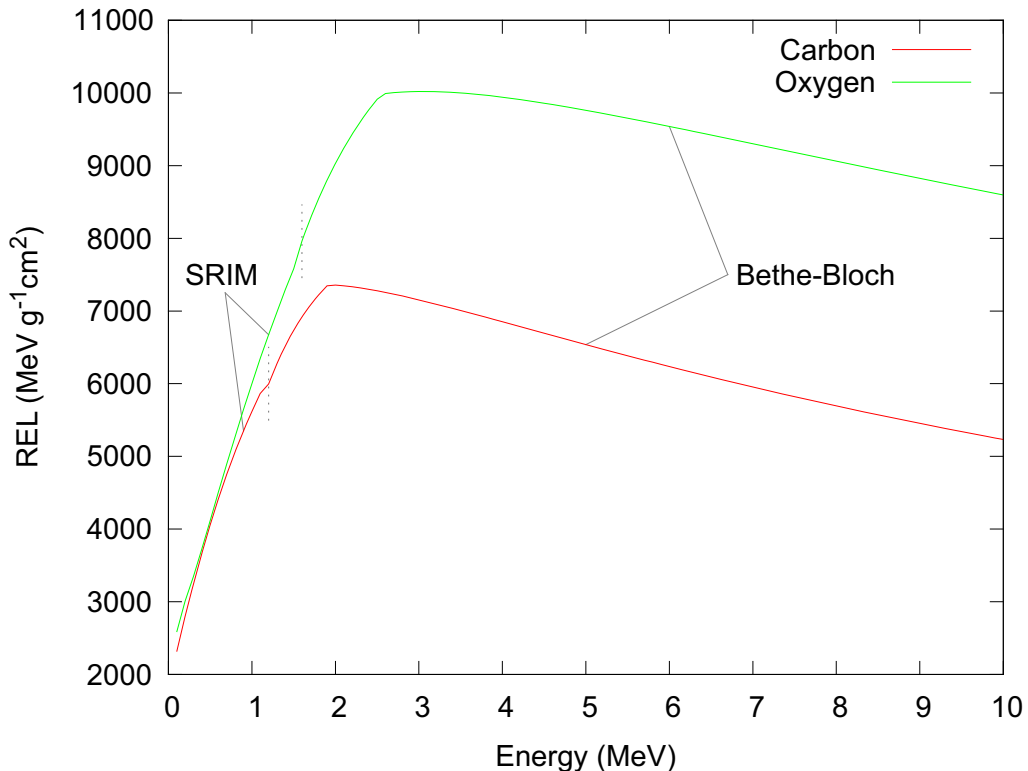


Figure 4.19: Calculated restricted energy loss (REL) of carbon and oxygen in Makrofol, using SRIM and the Bethe-Bloch formula for different energy regions.

4.2.2.4 Density Corrections

Due to the existence of overlapping effect, the track density per unit dose is not a constant. For high track densities, the overlapping effects are supposed to be strong, as the tracks overlap with a larger probability. Based on the method mentioned in Section 3.5.2.4 and the distribution of track diameters obtained from the experiment (see Figure 4.20), the track densities per unit dose were calculated for different doses.

First, it is supposed that the track density is proportional to the dose. Then, a density correction factor is calculated for the track density. Finally, the track density is multiplied by the correction factor to get the density to be comparable to the experiments.

A judgement criterion, which decides when two tracks should be recognized as one, is

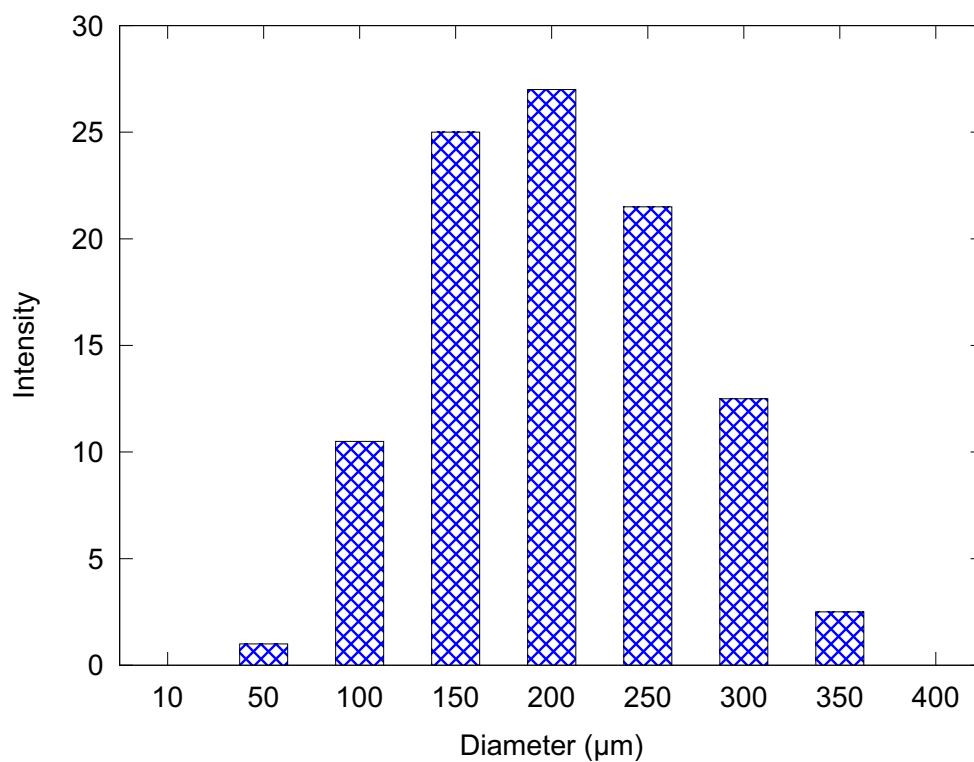


Figure 4.20: Measured distribution of track diameters, taken from ref. (Straubing, 2009).

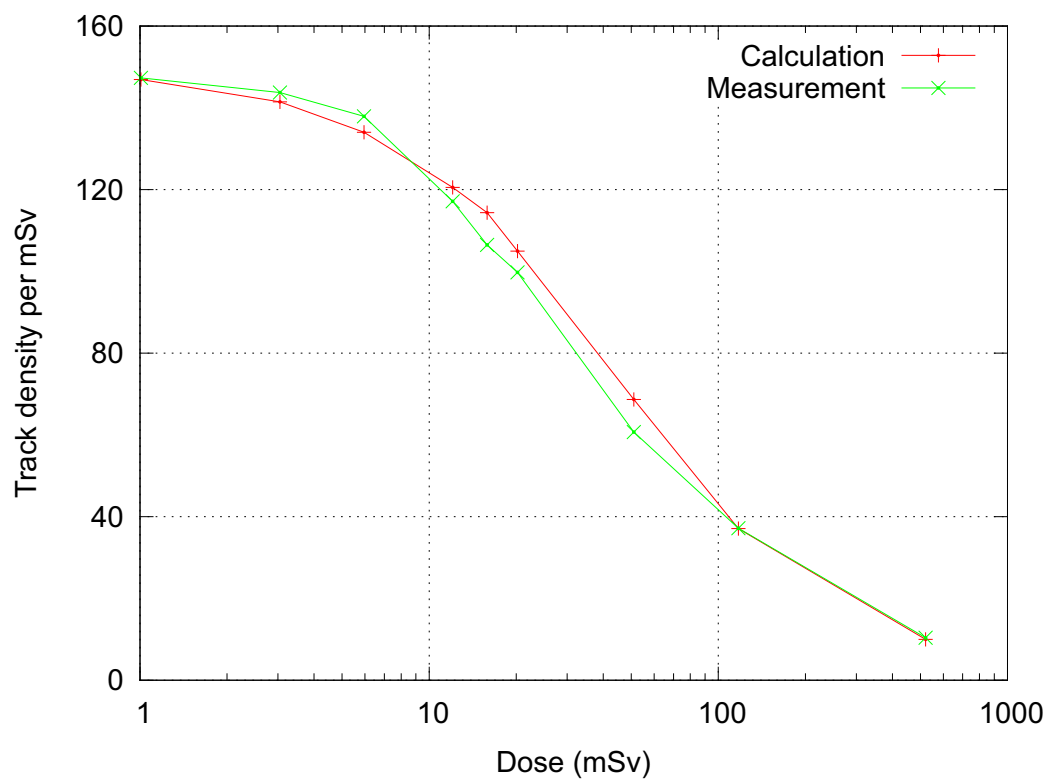


Figure 4.21: Track density per unit dose as a function of dose. The measured data are taken from ref. (Str).

necessary. In the simulations, the distance between the centers of two tracks is used to determine overlapping tracks. When the distance is smaller than a given limit L , the track of the smaller radius will be removed.

$$L = r_1 + r_2 - k * \min(r_1, r_2) \quad (4.2)$$

where r_1 and r_2 are the radii of the two tracks and k is a constant factor. The track of the smaller radius will be removed.

Figure 4.21 shows the results of experiments and simulations with $k = 1.4$ (see Equation 4.2). The results agree well.

4.2.2.5 Comparison of Monte Carlo Codes

Monte Carlo simulations are based on the sampling of tabulated experimental data and/or physics models with the help of random numbers. In MCNPX, the physics models are poor at low energies (<150 MeV); thus, data tables should be used when available (Hendricks, 2003). Unfortunately, table interactions in MCNPX do not produce heavy recoils for transport. To get the detail information of heavy recoils, which includes ion type, energy, position, moving direction and so on, physics models have to be used. In Geant4, different models, which can be data driven, theory driven or both, are available for simulations. For the transport of neutrons, data driven high precision models can be used. The high precision model is based on evaluated neutron data library, which contains cross sections, angular distributions and other information.

For the simulation of Makrofol detectors, both the MCNPX physics models and the data driven high precision neutron model of Geant4 have been investigated. The angular and energy distributions are shown in Figure 4.22 and 4.23, respectively.

The two codes gave rather different results. For the angular distribution, the curve of Geant4 has two peaks while MCNPX's curve only has one. For the energy distribution, leaving out the fluctuation on the Geant4's curve, the results of Geant4 and MCNPX show a similar trend. The amount of heavy recoils given by Geant4 is higher than by MCNPX.

4.2.2.6 Angular Response

The angular response of Makrofol detectors to neutrons has been investigated in this work in order to provide data for the effect of different neutron incident angles and to design dosimeters with an almost angular independent response in stray neutron fields.

Experimental Results

Front detectors and rear detectors, with respect to the neutron source, were analyzed separately. The track densities of different neutron incident angles are shown in Figure 4.24 and Figure 4.25. The track densities of the rear detectors are higher than those of the front

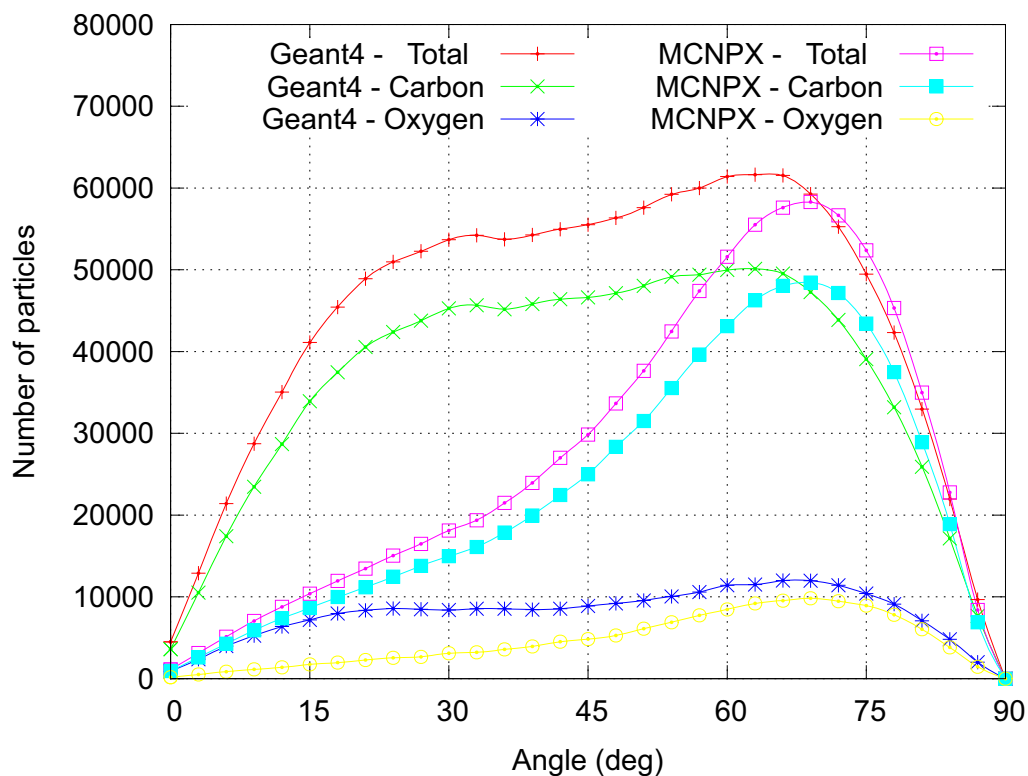


Figure 4.22: Simulated angular distribution of recoils in Makrofol induced by Cf-252 neutrons.

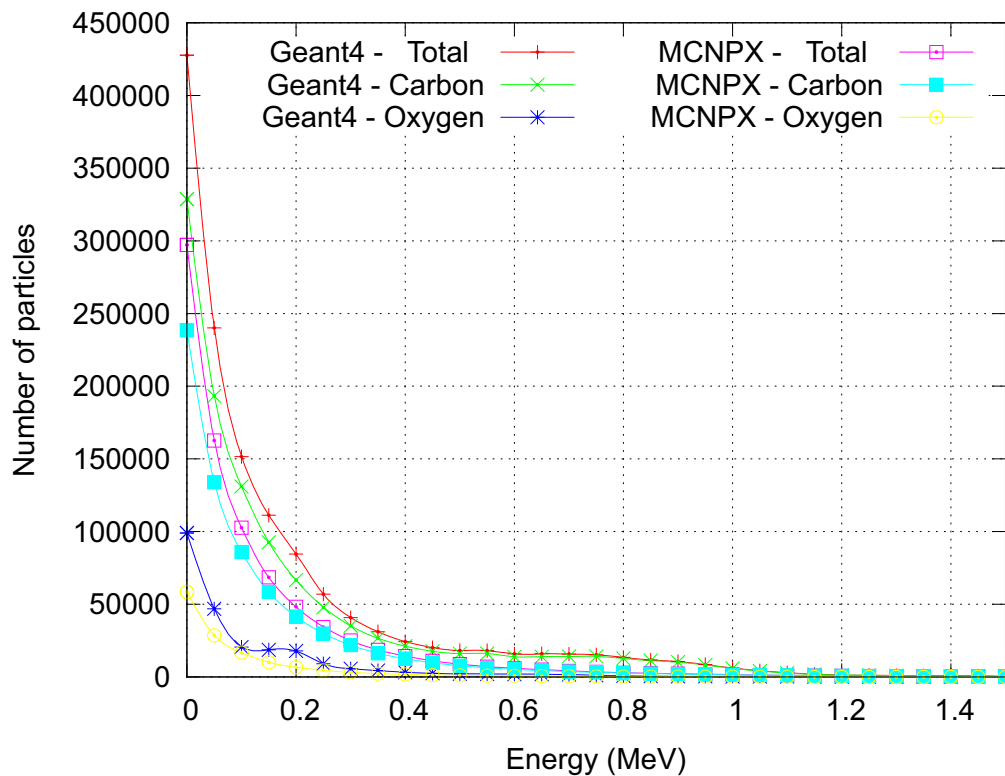


Figure 4.23: Simulated energy distribution of recoils in Makrofol induced by Cf-252 neutrons.

detectors in both experiments. Since the etching direction is the same as the direction of incident neutrons for rear detectors, and it is opposite for front detectors, energy loss variation along the ion path (Dörschel *et al.*, 1997) could be the reason of the density differences.

Despite the different track densities of front and rear detectors, the relative responses are similar (see Figure 4.26 and Figure 4.27), considering the error bars. Due to the lower relative errors, rear detectors are used for the further analysis.

The relative angular responses of the KIT and PSI experiments are shown in Figure 4.28. Normally, the overlapping effect should change the curve shape for different doses. In this work, although the irradiated doses are different for the two experiments (2.762 mSv at KIT; 10 mSv at PSI), the angular response curves are similar within the error bars. Therefore, the overlapping effect was neglected in the simulations.

Calculation Results

When different combinations of α and β in Equation 3.9 are used, the angular responses of simulations are much different (see Figure 4.29) for both MCNPX and Geant4. Since the values of α and β are relevant to the detector material and etching conditions, such as duration, etchant temperature and so on, a combination should be chosen to fit well the experimental data.

As shown in Figure 4.30 and Figure 4.31, $\alpha = 0.0028$ and $\beta = 3.3$ for MCNPX, $\alpha = 0.0034$ and $\beta = 3.5$ for Geant4 were selected to fit the experiment at KIT (Zhang *et al.*, 2011a) (see Section 3.5.2.5).

Figure 4.32 and Figure 4.33 show that $\alpha = 0.0028$ and $\beta = 3.2$ for MCNPX, $\alpha = 0.0029$ and $\beta = 3.5$ for Geant4 are a good approximation to describe the experiment at PSI (see Section 3.5.2.5).

Using appropriate values for α and β , the calculated response of Makrofol based on MCNPX or Geant4 fits to the experiments. For the large angles, the calculated response based on Geant4 agrees better with the experimental results.

As mentioned in Section 4.2.2, a layer of an average thickness of $35.8 \mu\text{m}$ is removed during the etching process. Without regard to the overlapping effect, the calculated track densities should be higher than the measured ones if the whole layer is taken into account. The track densities of calculations and experiments can be found in Figure 4.34. The calculated track densities based on MCNPX are lower than the experiments while the ones based on Geant4 are higher than the experiments. Because after a period many tracks formed at the beginning will disappear (Tommasino *et al.*, 1984) and the overlapping effect also reduces the track density, the experimental data should be lower than the calculated ones. Thus, the calculation results based on Geant4 are supposed to be more reasonable than those based on MCNPX.

Considering the low statistics of the KIT experiment and the similar angular response curves, Geant4 code combined with the selected energy thresholds (carbon: 0.24 MeV, oxygen: 0.32 MeV) and the values of $\alpha = 0.0029$ and $\beta = 3.5$ provided the better fit to the experiment.

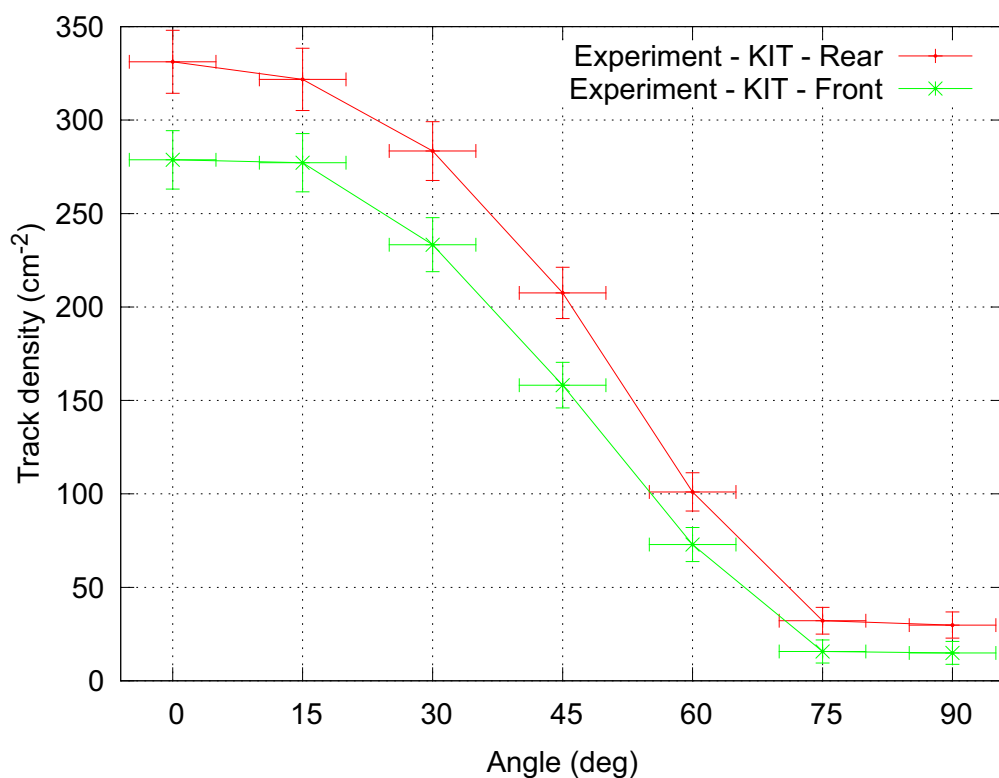


Figure 4.24: Counting results of the experiment at KIT. Detectors at front and rear side of the detector pair (with respect to the source) were counted separately.

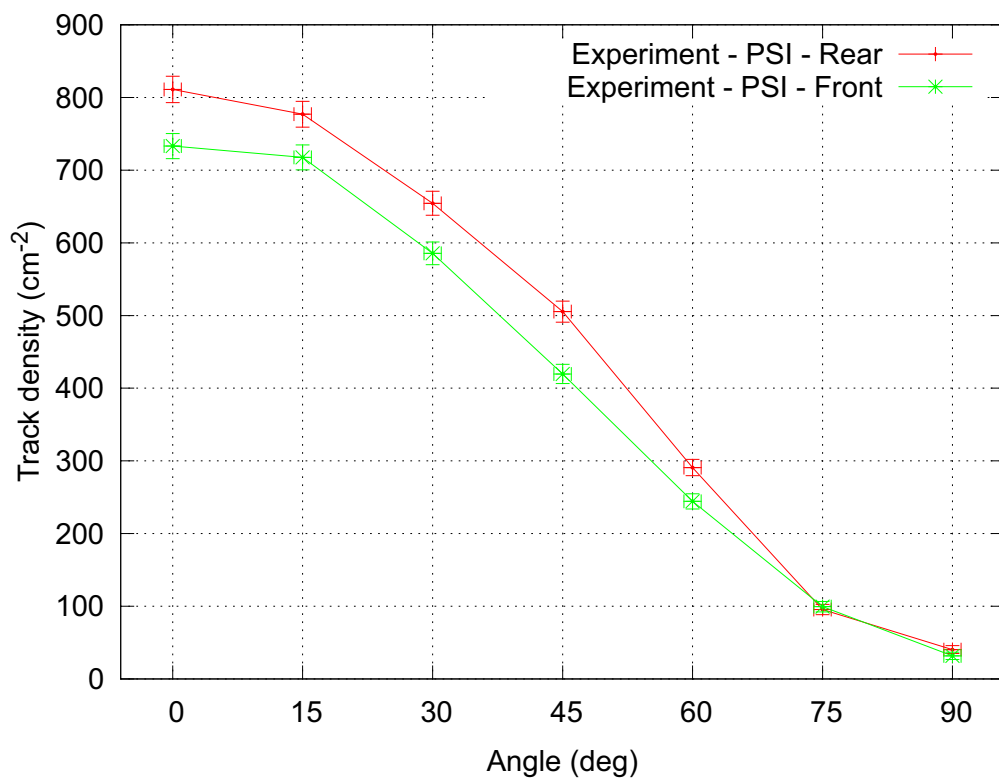


Figure 4.25: Counting results of the experiment at PSI. Detectors at front and rear side of the detector pair (with respect to the source) were counted separately.

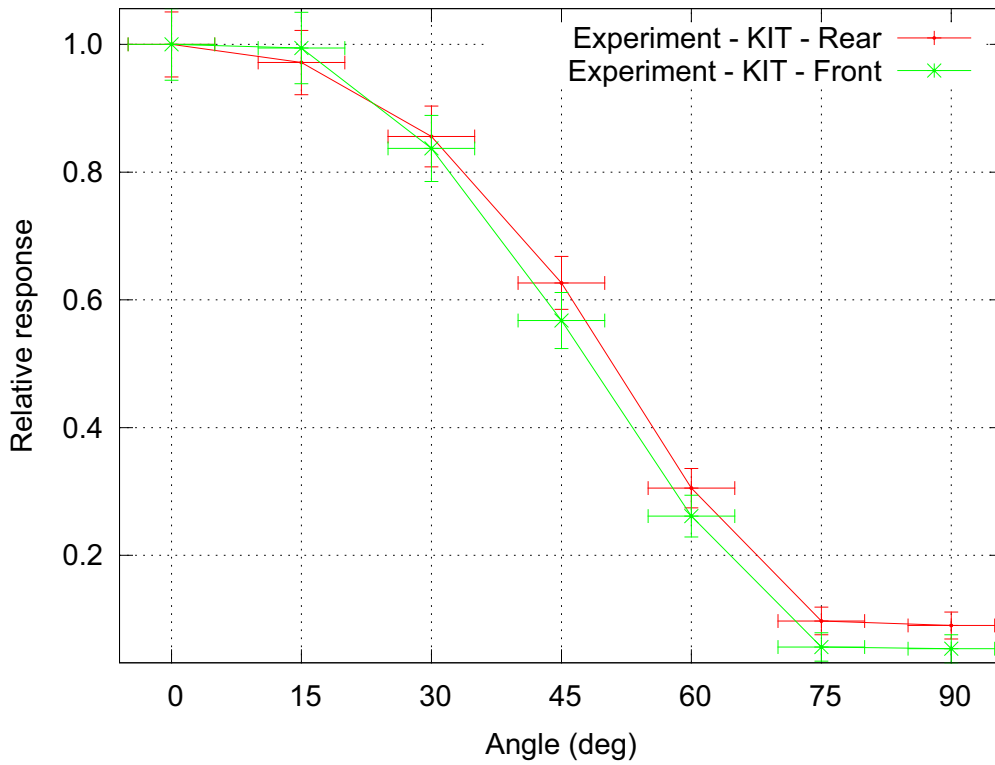


Figure 4.26: Relative response of the experiment at KIT. Detectors at front and rear side of the detector pair (with respect to the source) were counted separately.

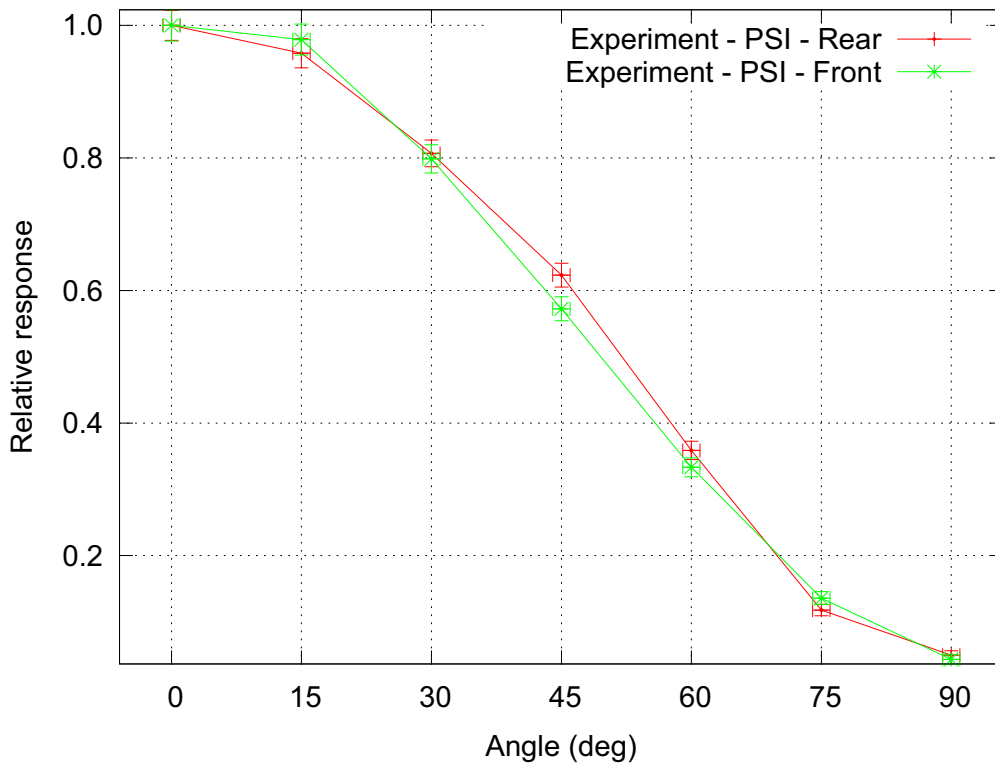


Figure 4.27: Relative response of the experiment at PSI. Detectors at front and rear side of the detector pair (with respect to the source) were counted separately.

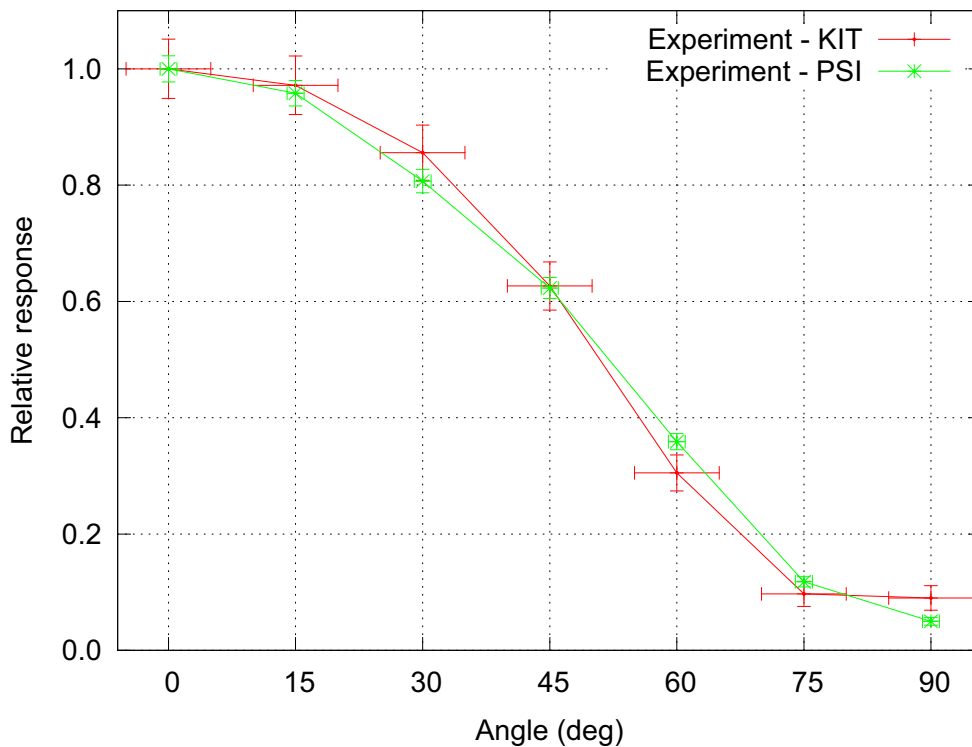


Figure 4.28: Comparison of experimental results of relative angular responses. Detectors at the rear-side (with respect to the source) of the detector pairs were used for the track counting.

4.2.2.7 Angular Responses of Detectors of Different Shapes

Detectors with an almost angular independent response can be used in high-scattering fields, such as the interim storage facility. In the work of Józefowicz et al. (Józefowicz *et al.*, 1997) two or three detectors perpendicular to each other were investigated to get a flat angular response. In this work more combinations were investigated to search for improved better angular responses. Geometries based on triangles and squares were considered which can be simply manufactured from Makrofol foils.

Based on the calculated and experimental results of different incident angles of neutrons, the responses of dosimeters of different shapes were calculated.

First different angles between incident neutrons and detectors were simulated, then the response of each detector of the dosimeter is calculated by the interpolation of the results.

Tetrahedron, pyramid and cube detectors (see Figure 4.35) were calculated. As shown in Figure 4.36, in order to see the effect of the anisotropy of the detectors, the response curve was calculated with a point neutron source placed on two planes respectively. The neutron source was moved along the semi circle on the plane and the distance between the center of the detector and the position of the source is the same at different positions.

Figure 4.37 shows the response curve of different dosimeters. As can be seen, the tetrahedron dosimeter shows the most constant response with respect to angle dependence. Even the experimental result obtained under similar conditions follows the trend of the calculations.

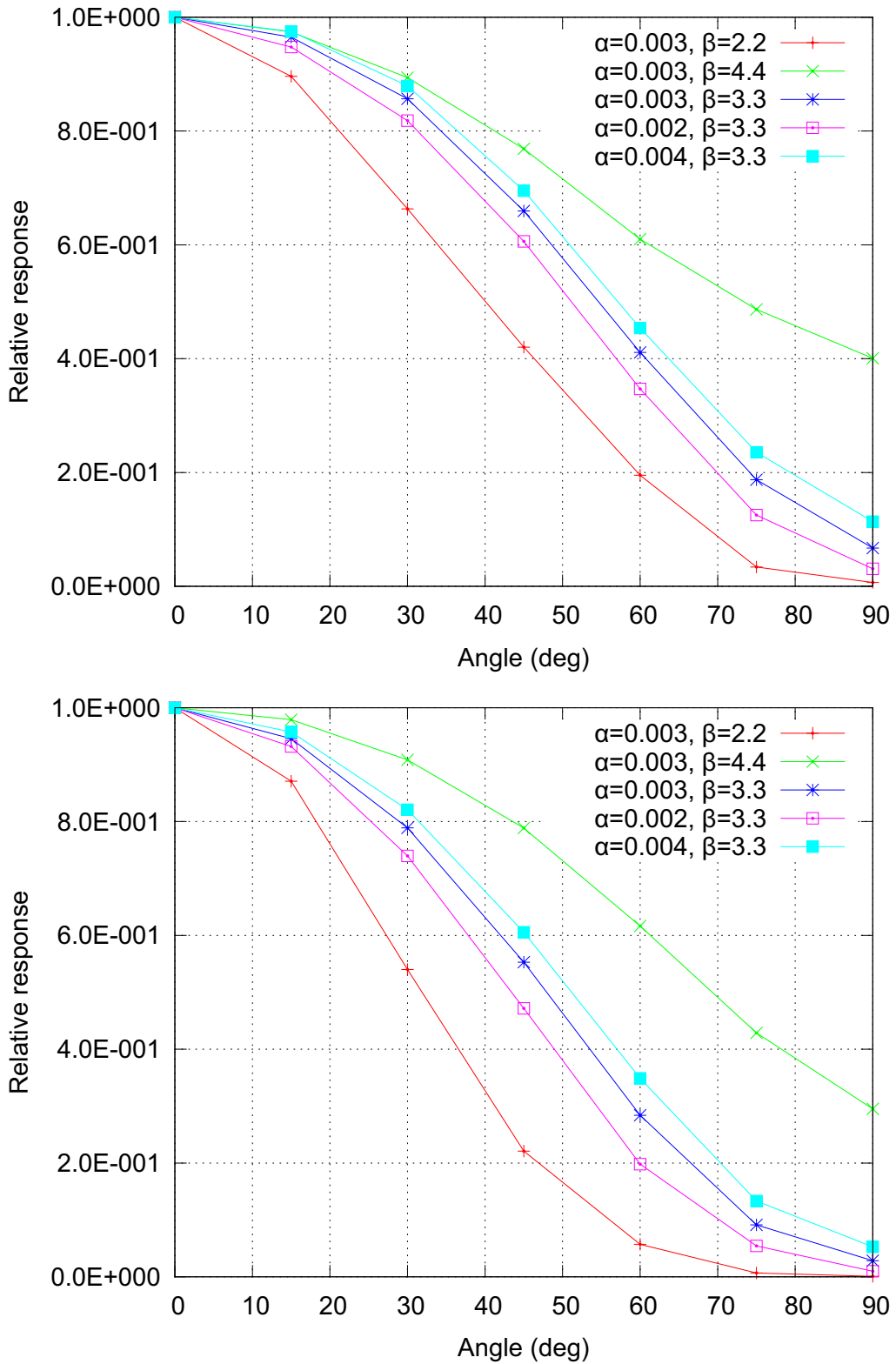


Figure 4.29: Relative response obtained with different α and β parameters calculated with MCNPX (top) and Geant4 (bottom).

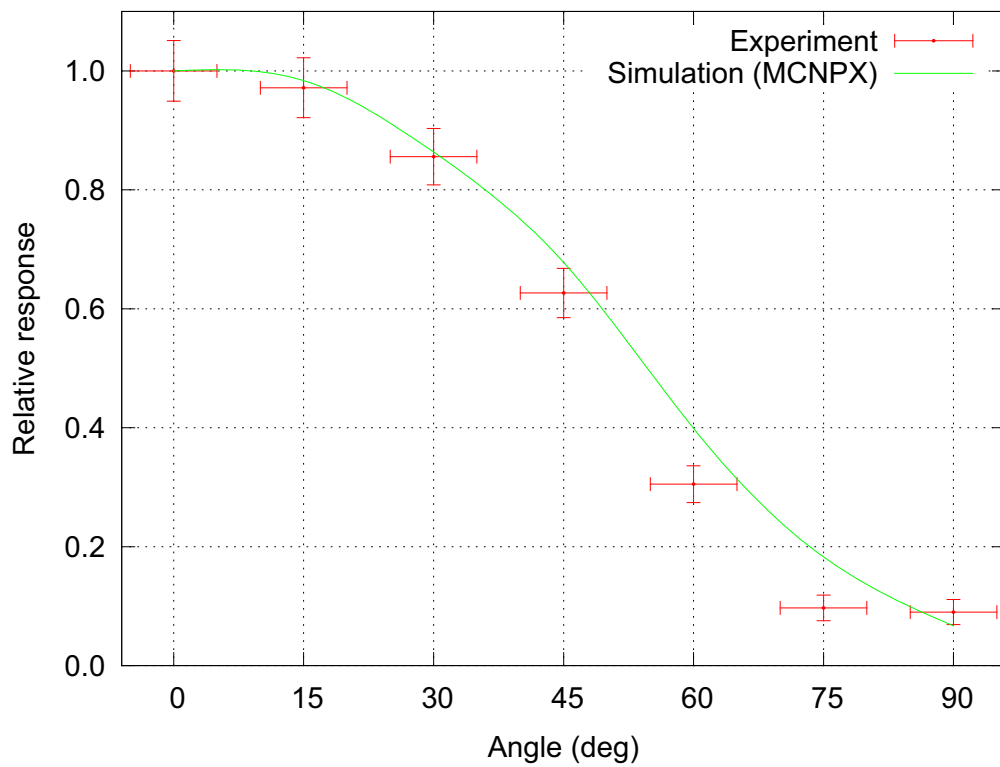


Figure 4.30: Relative angular response of the KIT experiment and calculation with $\alpha = 0.0028$ and $\beta = 3.3$.

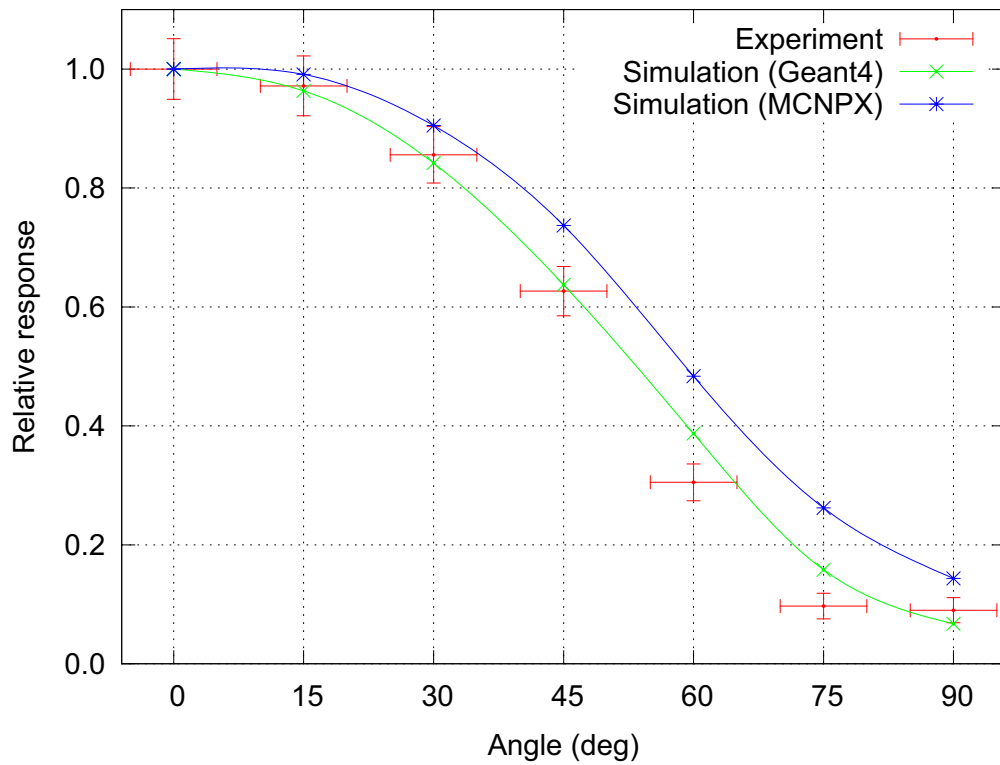


Figure 4.31: Relative angular response of the KIT experiment and calculation with $\alpha = 0.0034$ and $\beta = 3.5$. With the same α and β the results of the MCNPX simulation are much different from the results of Geant4.

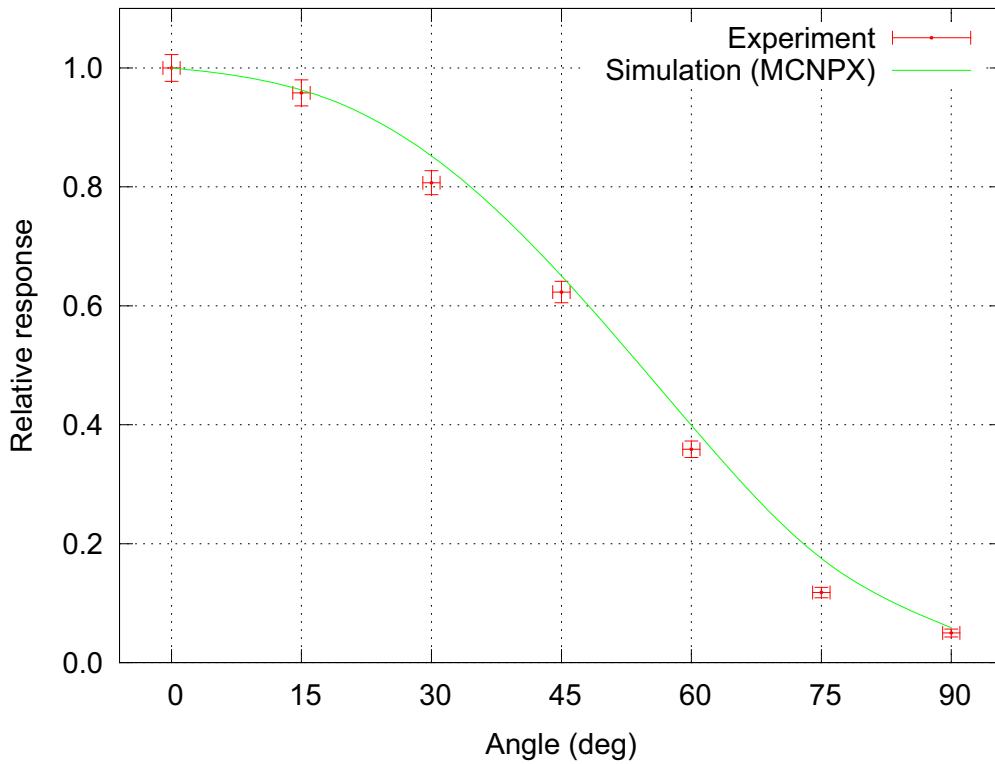


Figure 4.32: Relative angular response of the PSI experiment and calculation with $\alpha = 0.0028$ and $\beta = 3.2$.

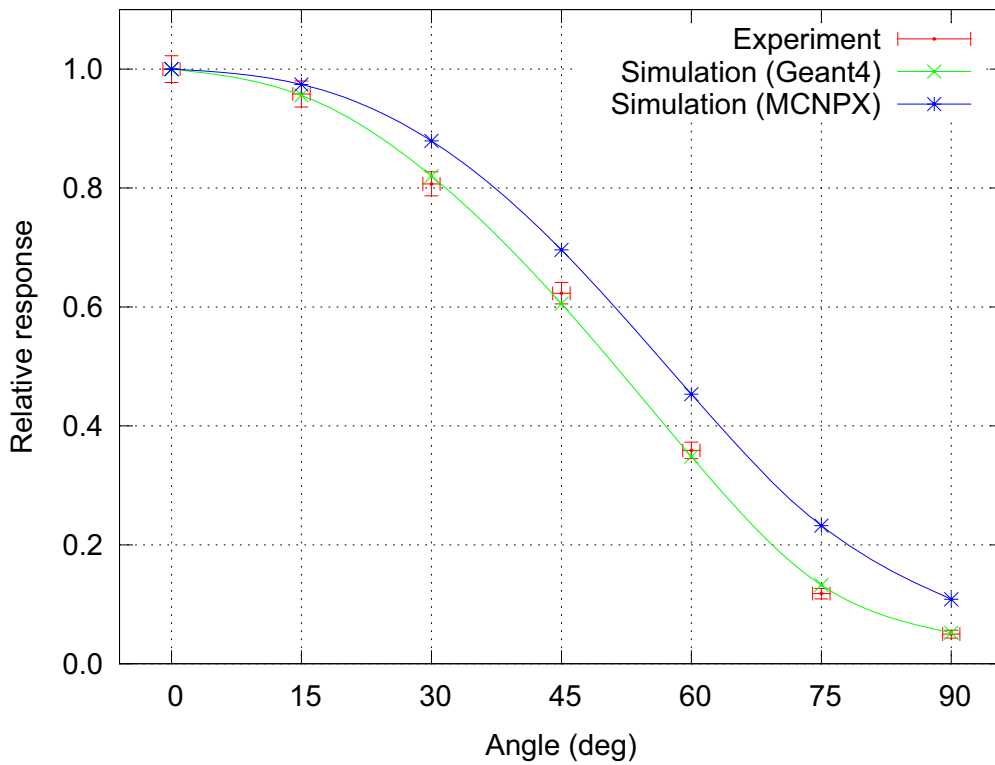


Figure 4.33: Relative angular response of the PSI experiment and calculation with $\alpha = 0.0029$ and $\beta = 3.5$. With the same α and β the results of the MCNPX simulation are much different from the results of Geant4.

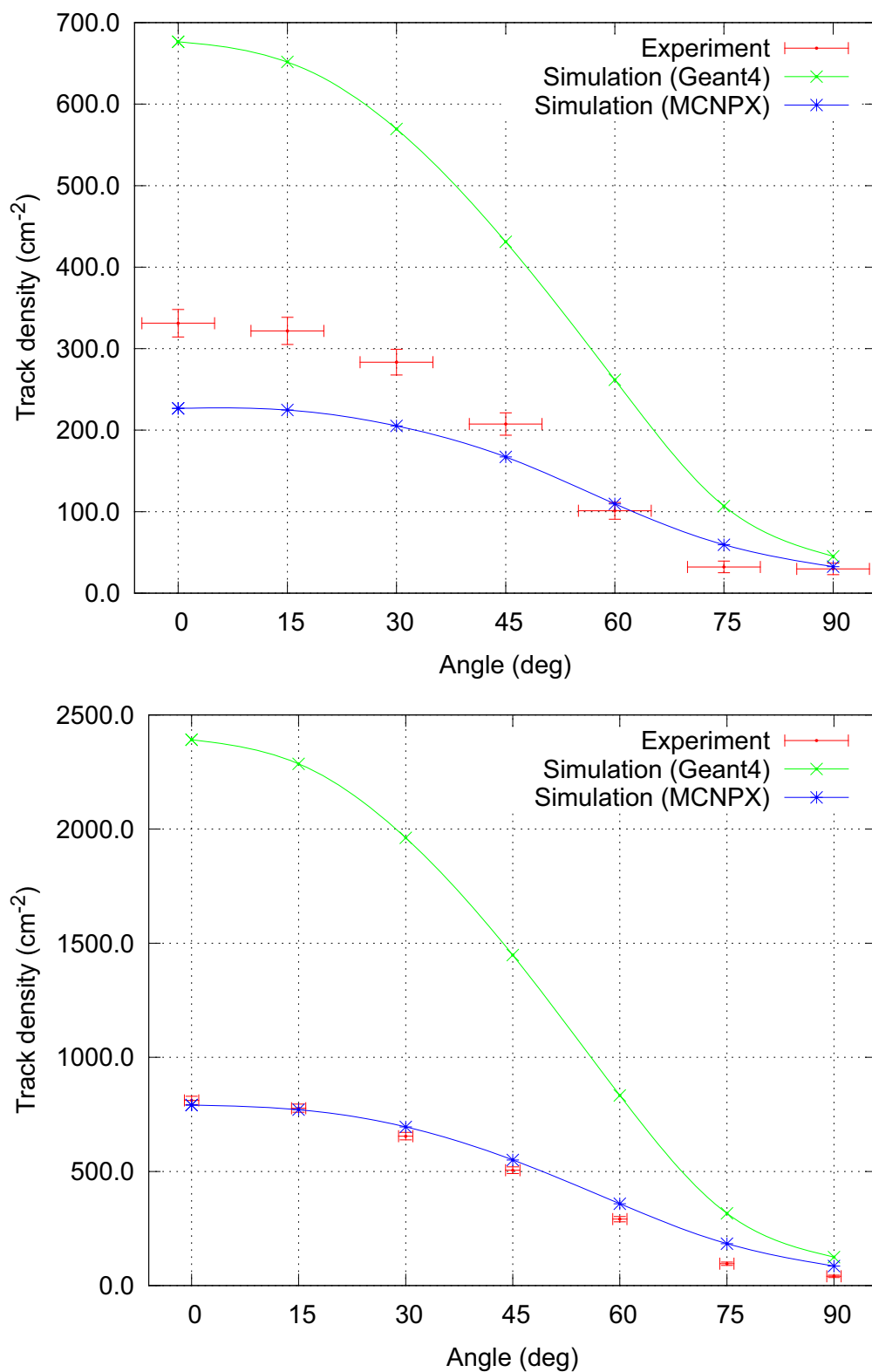


Figure 4.34: Track densities of calculations and experiments of KIT (top) and PSI (bottom). As the ideal condition is used, the calculated track density should be higher than the experimental result. This is true for Geant4 simulation but not for MCNPX as the two codes give different angular distributions of heavy recoils.

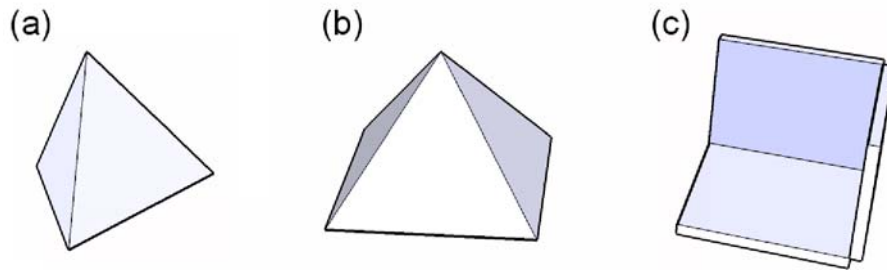


Figure 4.35: Dosimeter setup of (a) tetrahedron, (b) pyramid and (c) cube.

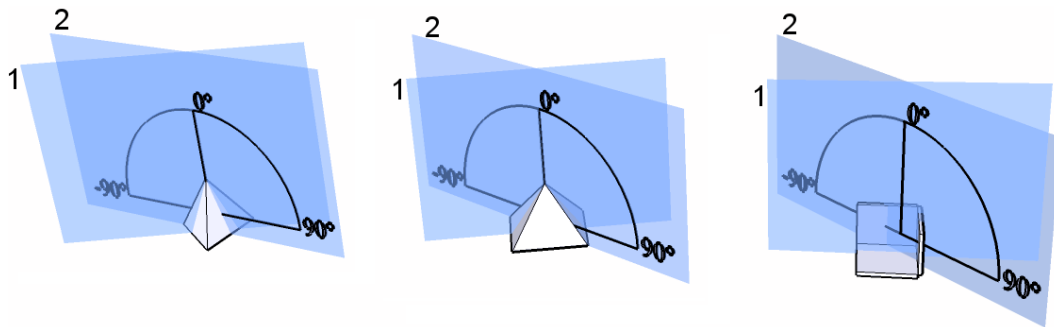


Figure 4.36: The two planes where the neutron source was placed to calculate the angular response.

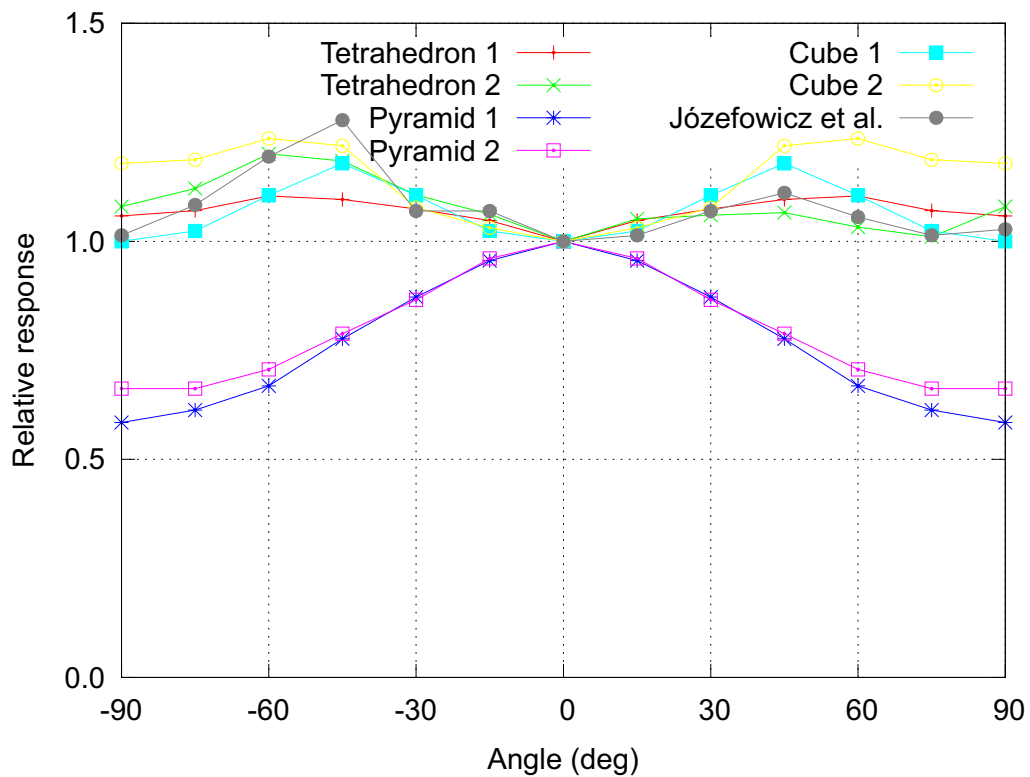


Figure 4.37: Relative responses of detectors of different shapes for the neutron sources on the circles of two different planes (see Figure 4.36). The experimental result of Józefowicz et al. is taken from ref. (Józefowicz *et al.*, 1997).

Chapter 5

Conclusions and Perspectives

5.1 Presentation of Problems

For inhomogeneous mixed neutron-gamma fields, such as the field in an interim storage facility, Monte Carlo simulations are useful to estimate the dose distribution. As a results of the complex geometry, namely the thick CASTOR wall and the large number of CASTORs, it is very time-consuming to obtain reliable results. Sometimes several days or even weeks are needed to finish one calculation. Therefore, a better calculation method is needed to reduce the calculation time and to improve the calculation efficiency. To get a knowledge of the radiation field in the storage facility, the dose distribution of neutrons and gammas in the facility, which could provide a reference for radiation protection purposes, is of interest.

Albedo neutron dosimeters are frequently used to measure personnel neutron doses. In different areas of applications the neutron spectra could differ mainly due to scattering, therefore the albedo dosimeter needs to be calibrated for each neutron field. A proper calibration of the albedo dosimeter is expected to be performed for the field of an interim storage facility with the help of Monte Carlo codes. The calibration should provide an accurate neutron dose estimation.

One good feature of SSNTDs is that they are insensitive to photons at personnel dose level. This feature makes SSNTDs a useful tool to detect fast neutrons in mixed neutron-gamma fields. However, the response of SSNTDs depends on the incident angle and the energy distribution of neutrons. For different neutron fields the corresponding response is supposed to be different. Therefore, a simulation method is needed to calculate the angular response of SSNTDs. The simulation is helpful to understand the mechanism of the track formation and the dose dependent number of tracks, including the angular response, which could help to design optimized dosimeters.

5.2 Solutions

MCNP5 version 1.51, which has a better performance for surface sources than previous versions, has been used for the calculations of CASTORs and an interim storage facility. In order to improve the calculation efficiency for CASTORs, weight windows have been used. The weight windows can change the space distribution of particles during the transport and favor more particles going through the CASTOR wall with the aim to contribute mainly to the detector score. When a large number of CASTORs are placed in the interim storage facility, surface sources have been used. Copying and translating the surface source from one position to another, instead of calculating the source for each CASTOR, can save calculation time. Parallel computing on a Linux cluster system, which allows to use multi-processors, has been also applied to speed up the calculation.

An Alnor type albedo neutron dosimeter was modelled and simulated with the MCNP code. Using the field calibration technique (Burgkhardt and Piesch, 1988), the Alnor albedo dosimeter was calibrated for the field in the interim storage facility with the MCNP code. Based on calculation results, the calibration factor for reactors and accelerators with heavy shielding was found to be suitable for the neutron field in the facility. Hence in this case staffs could wear the same dosimeter in the storage facility and in reactor or accelerator buildings.

The interaction of neutrons and Makrofol detectors has been simulated with the Monte Carlo codes MCNPX and Geant4. Based on the data obtained with the Geant4 code, the energy threshold and the critical angle, which is a function of two constant factor α , β (see Section 3.5.2.3) and the restricted energy loss of different particles in the detector material, the relative response of Makrofol detectors to Cf-252 neutrons can be calculated. With the energy thresholds of 0.24 MeV for carbon and 0.32 MeV for oxygen, and the values of $\alpha = 0.0029$ and $\beta = 3.5$ the calculated angular response agrees well with the experimental results. A Monte Carlo based algorithm has been developed to simulate the behaviour of track overlapping, which can be used to correct for track densities. A code called SSNTDKIT has been developed to process the simulation data and to calculate track densities. This code can analyze the data from Monte Carlo codes, calculate critical angles for different recoils, count tracks, implement the algorithm for the correction of overlapping tracks and so on. To get a less angular dependent response, different shapes of dosimeters were tested. Compared to the others, the tetrahedron dosimeter shows a better response.

5.3 Summary

A comprehensive study was performed in this work to contribute to field calibration methods of radiation protection dosimeters in which Monte Carlo simulations have been employed. The mixed neutron-gamma radiation field of a representative interim storage facility was chosen as example. It was shown that the simulations are a useful tool to determine an accurate correlation between the response of specific dosimeters to a given mixed neutron-gamma

radiation field. With the combination of the high computing power together with variance reduction techniques, nowadays results can be obtained with reasonable effort, even for complex radiation fields. Although an increased effort and time may be needed to simulate a more complex problem (e.g. all important details of the geometry and the radiation source, the shielding material and scattering material), the advantage of a full characterization of the workplace field in all necessary terms (e.g. energy distribution) of all radiation components can be achieved. Based on the simulated results, quantities such as personal or ambient dose equivalents can be achieved straightforward using relevant conversion coefficients.

The method of simulating the response of Makrofol as SSNTDs to fast neutrons has been investigated. With the method the response of Makrofol detectors to Cf-252 neutrons can be calculated. This work provides a good starting point for future investigations. For example, the application of Makrofol detectors could be optimised for a better dose estimation, and dosimeters with a better response to different neutron fields could be designed.

5.4 Perspectives

The methods of simulating the radiation field of the interim storage facility loaded with CASTORs, calibrating albedo dosimeters in the mixed neutron-gamma field, simulating the response of Makrofol detectors to fast neutrons are presented in this work. On the basis of the methods, tools and experiences in this work, further calculations and measurements could be done in the future.

Source data of CASTORs are difficult to get in detail because they are usually confidential. If new or more accurate source data are available calculations can be performed straight forward with the methods discussed in this thesis. For example, measurements in different interim storage facilities can be carried out, e.g. with Bonner spheres, and verified by calculations when the CASTOR source information is available. The information from different facilities would help to determine, if in general the radiation field in interim storage places are similar or not, and which dosimeters are well suited.

An Alnor albedo dosimeter was simulated with Monte Carlo codes. Since the neutron scattering in the interim storage facility influences the response of albedo dosimeters, the dosimeter could be used to perform measurements in the different sites to verify simulation results.

Since the simulation results of Makrofol detectors were verified with the experiments of Cf-252 sources, it is expected to perform extended investigations with Am-Be sources or in neutron fields such as in reactors, fuel processing plants and storage facilities.

The density correction algorithm of this work is applicable for an Am-Be source. In order to verify if it is applicable for Cf-252 source, new experiments with a strong Cf-252 source should be performed to get the distribution of track diameters and the density per dose for different doses. The algorithm can also be extended to tracks induced by other particles.

To get insight into the effect of backscattering, experiments with Makrofol detectors right

behind the ICRU sphere are suggested.

Long term perspectives with respect to this work: concerning the $H_p(10)$ response of different personnel dosimeters a strong variation is observed (Schuhmacher *et al.*, 2006). The over- and under responses of up to one order of magnitude is still a challenge for dosimetry. A strong under response could result in a transgression of radiation dose limits, while a strong over response has the economic aspect that workers reaching their annual dose limit have to stop their work earlier and are supposed to be replaced by extra personnel.

The investigation of this work, so far is limited to selected passive dosimeters, could be extended to active dosimeters too. The evaluation of dosimeter specific correction factors to be applied in particular types of mixed radiation fields is still a prerequisite to achieve sufficient accuracy for neutron dosimeters in workplace fields.

Appendix A

MCNP Input Files for CASTOR V/19 and Mesh Geometry

A.1 CASTOR V/19 Input File

```
c *****Start*****
c MCNP5 - Philippsburg Interim Storage Facility (Zwischenlager) and CASTOR V/19
c *****
c Cell Cards
c *****
1 4 4.98507E-05 -14 fill=1
2 11 -2.4 -15 12 -13 u=1
24 5 -7.2 -8 15 12 -13 u=1
21 6 -0.93 -18 8 12 -13 u=1
3 5 -7.2 (-7 16 -17 ) (18: -12: 13) u=1
4 4 4.98507E-05 7:-10 :11 u=1
22 6 -0.93 -7 -16 10 u=1
23 6 -0.93 -7 -11 17 u=1
6 4 4.98507E-05 -31 14
20 1 -2.3 31 -30
8 0 30

c *****
c Surface Cards
c *****
30 RPP 0 1830 0 6080 0 1855
31 RPP 70 1800 70 6000 150 1800
c
7 c/z 1550 300 119.8
8 c/z 1550 300 84
15 c/z 1550 300 70.2
18 c/z 1550 300 95
c
10 pz 151
16 pz 160
12 pz 201
c
11 pz 736.2
13 pz 686.2
17 pz 727.2
c
14 RPP 1430 1670 180 420 150.5 737

c *****
c Data Cards
c *****
imp:n,p 1 1 1 1 1 1 1 1 1 1 0
c *****
c Concrete, density=2.3 g/cc
M1 1001.66c -0.022100
6000.66c -0.002484
```

```

8016.66c -0.574930
11023.66c -0.015208
12000.66c -0.001266
13027.66c -0.019953
14000.60c -0.304627
19000.66c -0.010045
20000.66c -0.042951
26000.50c -0.006435
plib=04p
c
M4 7014.66c 0.78 8016.66c 0.22          $ Air
    plib=04p
c
c *****
c   GGG40  Steel
M5   6000.66c  3.65E-02  $C
     14000.60c  2.5E-02  $Si
     25055.66c   4E-03  $Mn
     15031.66c  1E-03  $P
     16000.62c  1E-04  $$
     12000.66c  9E-04  $Mg
     26000.50c  9.325E-01  $Fe
     plib=04p
c
M6   1001.50c -0.143716  $polyethylene, density = 0.9300 g/cc
     6000.66c -0.856284
     plib=04p
c *****
c   Spent fuel
M11  6000.66c -0.000022  8016.66c -0.09403  13027.66c -0.000044
     14000.60c -0.000176  24000.50c -0.005066  25055.66c -0.000351
     26000.50c -0.01455  28000.50c -0.006527  40000.66c -0.197135
     41093.66c -0.000486  42000.66c -0.000265  50000.40c -0.002716
     56138.66c -0.019899  92235.66c -0.003642
     92236.66c -0.003772  92238.66c -0.641826  94238.66c -0.00026
     94239.66c -0.004292  94240.66c -0.002341  94241.66c -0.002601
     plib=04p
c
mode n p
c
c *****
c   source
sdef  pos=1550 300 400 erg=d1 par=1 axs=0 0 1 rad=d2
      wgt=1 ext=d3
SI1  H
     1.0000E-08
     1.0000E-07  4.1400E-07  5.3158E-07  6.8256E-07  8.7642E-07
     1.2500E-06  1.4450E-06  1.8554E-06  2.3824E-06  3.0590E-06
     3.9279E-06  5.0435E-06  6.4760E-06  8.3153E-06  1.0677E-05
     1.3710E-05  1.7602E-05  2.2603E-05  2.9023E-05  3.7267E-05
     4.7851E-05  6.1442E-05  7.8893E-05  1.0130E-04  1.3007E-04
     1.6702E-04  2.1445E-04  2.7536E-04  3.5358E-04  4.5400E-04
     5.8295E-04  7.4852E-04  9.6112E-04  1.2341E-03  1.5846E-03
     2.0347E-03  2.2487E-03  2.4852E-03  2.6126E-03  2.7465E-03
     3.0354E-03  3.3546E-03  3.7074E-03  4.3074E-03  5.5308E-03
     7.1017E-03  9.1188E-03  1.0595E-02  1.1709E-02  1.5034E-02
     1.9305E-02  2.1875E-02  2.3579E-02  2.4176E-02  2.4788E-02
     2.6058E-02  2.7000E-02  2.8502E-02  3.1828E-02  3.4307E-02
     4.0568E-02  4.6309E-02  5.2475E-02  6.6562E-02  6.7379E-02
     7.2000E-02  7.9500E-02  8.2503E-02  8.6517E-02  9.8037E-02
     1.1109E-01  1.1679E-01  1.2277E-01  1.2907E-01  1.3589E-01
     1.4264E-01  1.4996E-01  1.5764E-01  1.6573E-01  1.7422E-01
     1.8316E-01  1.9255E-01  2.0242E-01  2.1280E-01  2.2371E-01
     2.3518E-01  2.4724E-01  2.7324E-01  2.8725E-01  2.9452E-01
     2.9720E-01  2.9850E-01  3.0197E-01  3.3373E-01  3.6883E-01
     3.8774E-01  4.0762E-01  4.5049E-01  4.9787E-01  5.2340E-01
     5.5023E-01  5.7844E-01  6.0810E-01  6.3928E-01  6.7206E-01
     7.0651E-01  7.4274E-01  7.8082E-01  8.2085E-01  8.6294E-01
     9.0718E-01  9.6164E-01  1.0026E+00  1.1080E+00  1.1648E+00
     1.2245E+00  1.2873E+00  1.3534E+00  1.4227E+00  1.4957E+00

```

```

1.5724E+00 1.6530E+00 1.7377E+00 1.8268E+00 1.9205E+00
2.0190E+00 2.1225E+00 2.2313E+00 2.3069E+00 2.3457E+00
2.3653E+00 2.4652E+00 2.4660E+00 2.5924E+00 2.7253E+00
2.8650E+00 3.0119E+00 3.1664E+00 3.3287E+00 3.6788E+00
4.0657E+00 4.4933E+00 4.7237E+00 4.9659E+00 5.2205E+00
5.4881E+00 5.7695E+00 6.0653E+00 6.3763E+00 6.5924E+00
6.7032E+00 7.0469E+00 7.4082E+00 7.7880E+00 8.1373E+00
8.6071E+00 9.0484E+00 9.5123E+00 1.0000E+01 1.0513E+01
1.1052E+01 1.1618E+01 1.2214E+01 1.2523E+01 1.2840E+01
1.3499E+01 1.3840E+01 1.4191E+01 1.4550E+01 1.4918E+01
SP1 D
0.0000E+00
0.0000E+00 0.0000E+00 0.0000E+00 0.0000E+00 0.0000E+00
0.0000E+00 0.0000E+00 8.5684E-06 1.2744E-05 0.0000E+00
1.2854E-05 1.7267E-05 0.0000E+00 0.0000E+00 0.0000E+00
2.3644E-05 1.3222E-05 0.0000E+00 4.2542E-05 5.6558E-05
8.1457E-05 1.0893E-04 1.0024E-04 1.2744E-04 2.3019E-04
3.2017E-04 2.6019E-04 1.6040E-04 1.2676E-04 4.7157E-05
1.0888E-04 1.2269E-04 2.0716E-04 2.9919E-04 4.4632E-04
6.6211E-04 8.0677E-04 1.1840E-03 1.3984E-03 7.9856E-04
7.7587E-04 1.0186E-03 7.7143E-04 1.0818E-03 1.9528E-03
2.1902E-03 1.6364E-03 1.2592E-03 1.4614E-03 1.4505E-03
1.6051E-03 1.7409E-03 1.8806E-03 1.9821E-03 2.0792E-03
2.2891E-03 2.4634E-03 2.6327E-03 2.8178E-03 3.0117E-03
3.1584E-03 4.4149E-03 5.6932E-03 4.5639E-03 2.5179E-03
1.1005E-03 3.0422E-04 3.1446E-03 8.0268E-03 9.5948E-03
7.5498E-03 8.3305E-03 1.2841E-02 1.3862E-02 1.0804E-02
9.3551E-03 9.8472E-03 1.0481E-02 1.0994E-02 1.1648E-02
1.2243E-02 1.2844E-02 1.3513E-02 1.4190E-02 1.4926E-02
1.6218E-02 1.6924E-02 2.0841E-02 2.6288E-02 2.3258E-02
1.9645E-02 2.0272E-02 2.0846E-02 2.1360E-02 2.1946E-02
2.2460E-02 2.2832E-02 2.3236E-02 2.3506E-02 2.3786E-02
2.3903E-02 2.3959E-02 2.1846E-02 1.6038E-02 9.5898E-03
7.2075E-03 1.2652E-02 8.7138E-03 1.8509E-02 2.2782E-02
2.2216E-02 2.1478E-02 2.0711E-02 2.4724E-02 3.1615E-02
3.1325E-02 2.3121E-02 1.4144E-02 1.0044E-02 8.8790E-03
7.7690E-03 6.7265E-03 5.7376E-03 4.4671E-03 2.8538E-03
2.1070E-03 2.7349E-03 2.6613E-03 2.0560E-03 1.6173E-03
1.3206E-03 9.8697E-04 7.0299E-04 5.0792E-04 3.5926E-04
2.4779E-04 1.6689E-04 9.8668E-05 5.0231E-05 3.7526E-05
3.2410E-05 1.9087E-05 1.1324E-05 8.6506E-06 7.7621E-06
SI2 0 70
SP2 -21 1
SI3 -195 280
nps 4E8
c ***** End *****

```

A.2 Mesh Input

Mesh input for photons:

```

mesh geom=cyl origin=1550 300 -1 ref=1550 300 400 axs=0 0 1 vec=0 1 0
imesh 50 70 125 200 1000 6250
iints 1 1 5 1 1 1
jmesh 1 150 200 686 736 1000 2000
jints 1 1 5 1 5 1 1
kmesh 1
kints 1

```

Mesh input for neutrons:

```
mesh geom=cyl origin=1550 300 -1 ref=1550 300 400 axs=0 0 1 vec=0 1 0
imesh 50 70 125 200 1000 6250
iints 1 1 14 1 1 1
jmesh 1 150 200 686 736 1000 2000
jints 1 1 14 1 14 1 1
kmesh 1
kints 1
```

Appendix B

Instruction on Using the SCC Cluster

The SCC Cluster consists of worker nodes and login nodes. Worker nodes are in charge of calculations while login nodes are used for submitting and manipulating tasks. In order to perform a parallel computing, please follow the following steps¹:

1. Log into one of the login nodes over port 24:

```
ssh -p 24 iwrcgvor1.fzk.de -X
```

or

```
ssh -p 24 iwrcgvor2.fzk.de -X
```

2. Edit a script for your calculation to assign the job type, task class, number of processors, name of output, hardware architecture and environment variables etc. as needed (for details please see Appendix C).

3. Submit your script:

```
llsubmit script.sh
```

4. Check the status of the running tasks:

```
llq taskID
```

```
llstatus taskID
```

or to get a graphic view (see Figure B.1):

```
llview
```

¹Tested on May 20, 2011

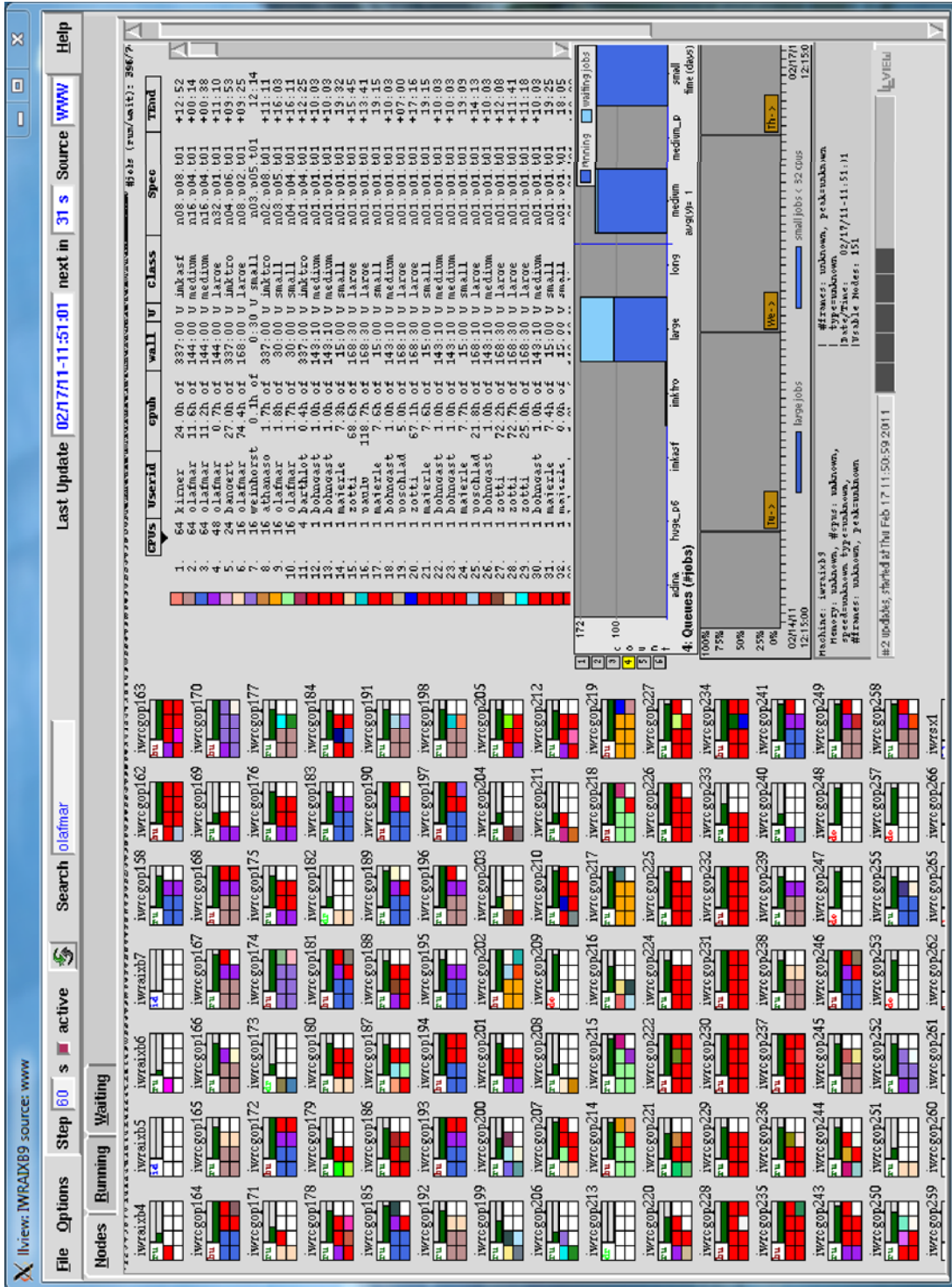


Figure B.1: Interface of ilview command.

Appendix C

Scripts for MCNP5/MCNPX

Script for compiling MCNP5 1.5.1 on the SCC cluster with MPI:

```
#!/bin/bash -l
module load pgi/7.0.7
module load mvapich/1.0.0
module switch pgi/7.2.2

make clean build CONFIG="plot mpi portland cheap" FC="pgf90" MPIFC="mpif90" CC="pgcc" MPICC="mpicc"
FOPT="-O3 -tp core2-64 -fast -fastsse " COPT="-noswitcherror -O3 -tp core2-64 -fast -fastsse " MPIFOPT="-
O3 -tp core2-64 -fast -fastsse " MPICOPT="-O3 -tp core2-64 -fast -fastsse -ldotcomm -lm -lmpich" PLOTLIBS="-
L/usr/X11R6/lib64 -lX11"
```

Script for running MCNP5 1.5.1 on the SCC cluster:

```
#!/bin/bash -l
# @ job_type = parallel
# @ output = $(executable).$(jobid).$(stepid).out
# @ error = $(executable).$(jobid).$(stepid).err
# @ notify_user = guoqing.zhang@kit.edu
# @ class = small
# @ checkpoint = no
# @ wall_clock_limit = 10:00:00,10:00:00
# @ group = local
# @ environment = TMP=/tmp;DATAPATH=/fzk/hs/localhome/olafmar/cgwork/v260_DATA
# @ restart = no
# @ requirements = (Arch == "x86_64")&&(OpSys == "SL") && (Feature=="penryn")
# @ node = 1
# @ tasks_per_node = 8
# @ queue

export MCNP5PATH=/work/olafmar/MCNP5
export DATAPATH=/fzk/hs/localhome/olafmar/cgwork/v260_DATA
module load pgi/7.0.7
module load mvapich/1.0.0

do_parallel $MCNP5PATH/mcnp5.mpi.penryn2 x=$DATAPATH/xsdir i=cas.inp
```

Script for compiling MCNPX 2.6.0 on the SCC cluster with MPI:

```
#!/bin/bash -l
module load pgi/7.0.7
module load mvapich/1.0.0
module list

../v260/configure \
  -prefix=/fzk/hs/localhome/olafmar/cgwork/MCNPX \
  -with-FC=mpif90 \
  -with-CC=mpicc \
  -with-FOPT="-fastsse -O3 -tp core2-64 -DUNIX=1 -DLINUX=1 -DG95=1" \
  -with-COPT="-fastsse -O3 -tp core2-64 -DUNIX=1 -DLINUX=1" \
  -with-MPILIB="-L/opt/mvapich-1.0.0-vapi.ics4.1.0.0.1_pgi7.0.7/lib -lmpich" \
  -with-MPIINC="/opt/mvapich-1.0.0-vapi.ics4.1.0.0.1_pgi7.0.7/include"

make
make install
```

Script for running MCNPX 2.6.0 on the SCC cluster:

```
# @ job_type = parallel
# @ output = $(executable).$(jobid).$(stepid).out
# @ error = $(executable).$(jobid).$(stepid).err
# @ step_name = Step_one
# @ notify_user = guoqing.zhang@kit.edu
# @ class = medium
# @ wall_clock_limit = 144:00:00,144:00:00
# @ checkpoint = no
# @ group = local
# @ environment = TMP=/tmp
# @ restart = no
# @ requirements = (Arch == "x86_64")&&(OpSys == "SL") && (Feature=="penryn")
# @ blocking = unlimited
# @ total_tasks = 8
# @ queue

module unload mcnp5
export DATAPATH=/fzk/hs/localhome/olafmar/cgwork/MCNPX/data
export MCNPX_DIR=/fzk/cgwork/olafmar/MCNPX
module load pgi/7.0.7
module load mvapich/1.0.0
module list

do_parallel $MCNPX_DIR/bin/mcnpx inp=inputfile xs=$MCNPX_DIR/data/xsdir
```

Appendix D

MCNP Input File for an Alnor Albedo Dosimeter

```
C *****Start*****
C ALNOR ALBEDO dosimeter
C Cell cards
61 63 -1.59 62 -61 64 66 u=66 $dosimeter capsule
62 65 -1.0 62 -61 -64 65 u=66 $transparent window
63 65 -1.0 -63 611 612 613 614 65 66 u=66 $detector capsule
65 66 -0.001205 -65 -64 62 -61 u=66 $beta window
651 66 -0.001205 -65 -63 u=66 $pit in front detectors
66 65 -1.0 -66 62 -61 u=66 $albedo neutron window
661 66 -0.001205 -66 -63 u=66 $pit in front detectors
69 66 -0.001205 63 -62 u=66 $gap
611 61 -2.6 -611 u=66 $TLD600
612 62 -2.6 -612 u=66 $TLD700
613 62 -2.6 -613 u=66 $TLD700
614 61 -2.6 -614 u=66 $TLD600
699 66 -0.001205 61 u=66 $outside the dosimeter
666 60 -0.93 -620 u=666 $ICRU Sphere
6660 66 -0.001205 60 61 620 u=666 $Air part
C dosimeters at two positions
6661 66 -0.001205 -60 u=666 *fill=66(31.12 0 2 180 90 90 90 0 90 270 90 180)
6662 66 -0.001205 -61 u=666 fill=66
C space filled with dosimeters and ICRU sphere
99 66 -0.001205 -630 *fill=666
C outer space
9999 0 630

C Surface cards
60 RPP 30.57 31.67 -1.70 1.70 -1.75 3.75 $dosimeter outer surface at position 1
61 RPP -0.55 0.55 -1.70 1.70 -1.75 3.75 $dosimeter outer surface at position 2
62 RPP -0.25 0.25 -1.54 1.54 -1.59 3.59 $inner surface of dosimeter capsule
63 RPP -0.23 0.13 -1.54 0.46 -0.50 3.20 $outer surface of detector capsule
64 RPP -0.65 -0.00 -1.80 1.80 1.30 3.20 $transparent window
65 RPP -0.65 -0.14 -0.60 0.40 1.30 2.60 $beta window
66 RPP 0.04 0.60 -0.40 0.20 0.10 1.30 $albedo window
611 RPP -0.095 -0.005 -0.24 0.06 2.05 2.35 $TLD-600 a
612 RPP -0.095 -0.005 -0.24 0.06 1.45 1.75 $TLD-700 a
613 RPP -0.095 -0.005 -0.24 0.06 0.85 1.15 $TLD-700 i
614 RPP -0.095 -0.005 -0.24 0.06 0.25 0.55 $TLD-600 i
620 SPH 15.56 0 1 15 $ICRU Sphere
630 RPP -250 250 -200 200 -200 200

mode n p
imp:n,p 1 17r 0
M60 1001.66c 2 6000.66c 1 plib=04p $polyethylene 0.93 g/cm3
M61 3006.66c 0.9562 3007.66c 0.0438 9019.66c 1.0 $TLD600 2.6 g/cm3
plib=04p
M62 3006.66c 0.00007 3007.66c 0.99993 9019.66c 1.0 $TLD700 2.6 g/cm3
plib=04p
C M63 Boron loaded plastic 1.59 g/cm3
```

```
C (50% B4C, 50% by weight Polystyrol and Makrolon plastic
M63 5010.66c -0.0721 5011.66c -0.3192 6000.66c -0.5700 1001.66c -0.0387
    plib=04p
C M64 ICRU Material density 1 g/cm3, diameter of 30 cm
M64 8016.66c -76.2 1001.66c -10.1 6000.66c -11.1 7014.66c -2.6
    plib=04p
M65 6000.66c 0.5 1001.66c 0.5 $Plastic density 1.0 g/cm3
M66  7014.66c -0.755636 $air (US S. Atm at sea level) 0.001205 g/cm3
    8016.66c -0.231475
    18000.59c -0.012889
    plib=04p
M67  1001.66c -0.022100 $concrete 2.300 g/cm3
    6000.66c -0.002484
    8016.66c -0.574930
    11023.66c -0.015208
    12000.66c -0.001266
    13027.62c -0.019953
    14000.60c -0.304627
    19000.66c -0.010045
    20000.66c -0.042951
    26000.55c -0.006435
    plib=04p
M6 3006.66c 1 plib=04p $Li-6
M7 3007.66c 1 plib=04p $Li-7
C Source
sdef par=n erg=D1 pos=-234.44 0 1 VEC=1 0 0 DIR=d2
SP1 -3 1.180000 1.03419
SI2 0.998198 1 $cone
SP2 0 1
F14:n  (611<6661) (612<6661) (613<6661) (614<6661)
        (611<6662) (612<6662) (613<6662) (614<6662)
FM14  (1 6 105) $get number of (n,alpha) reactions
NPS 2e6
C *****End*****
```

Appendix E

MCNPX Patch for SSNTD

MCNPX patch for SSTND simulations:

=====

```
diff -Nur v260/src/htape3x/opt16.F v260.ssntd/src/htape3x/opt16.F
--- v260/src/htape3x/opt16.F 2008-05-02 20:45:14.000000000 +0200
+++ v260.ssntd/src/htape3x/opt16.F 2009-08-16 13:21:17.437500000 +0200
@@ -32,6 +32,9 @@
     a1=aprr(i)                                /*op      32*/
     z1=zprrr(i)                               /*op      33*/
     e1=erecr(i)                               /*op      34*/
+   zgqu=ur(i)
+   zgqv=vr(i)
+   zgqw=wr(i)
     temp(3,i)=erecr(i)*flin(a1,z1,e1)         /*op      35*/
     ielstc=0                                  /*op      36*/
     if (mnuc.eq.1) call recels (ielstc)       /*op      37*/
@@ -39,6 +42,8 @@
     temp(2,1)=temp(1,1)                      /*op      39*/
     temp(4,1)=temp(3,1)                      /*op      40*/
     endif                                     /*op      41*/
+   Write(818,'(f4.0,1x,f4.0,e14.7,i5,i5,4f12.7,3e13.5)')
+   1   z1,a1,e1,ielstc,blz,wt,zgqu,zgqv,zgqw,xc,yc,zc
     60 continue                               /*op      42*/
     do 90 l=1,mnuc                            /*op      43*/
     do 90 it=1,4                              /*op      44*/
diff -Nur v260/src/include/htape3x/label.h v260.ssntd/src/include/htape3x/label.h
--- v260/src/include/htape3x/label.h 2008-05-02 20:45:16.000000000 +0200
+++ v260.ssntd/src/include/htape3x/label.h 2009-08-11 21:05:31.937500000 +0200
@@ -28,7 +28,7 @@
     & ub(102), va(102), vb(102), wa(102), wb(102), wta(102), wtb(102), /**1a    20*/
     & tca(102), tcb(102), wtsum(lpt,8), aprr(3), zprrr(3), erecr(3), uur /**1a    21*/
     & (3), ur(3), vr(3), wr(3), ecvr(3), namea(102), nel(lmt), mel(lmt) /**1a    22*/
-   & , jtipa(102), jtipb(102), nosum(lpt,8) /**1a    23*/
+   & , jtipa(102), jtipb(102), nosum(lpt,8), uoo(3) /**1a    23*/
!
!   use integer kind - these are equivalenced to variables above. /**1a5e   13*/
!   real(kind) :: dc, cx, fmu /**1a5e   14*/
!   real(kind) :: dc, cx, fmu /**1a5e   15*/
diff -Nur v260/src/include/lcs/rucom.h v260.ssntd/src/include/lcs/rucom.h
--- v260/src/include/lcs/rucom.h 2008-05-02 20:45:15.000000000 +0200
+++ v260.ssntd/src/include/lcs/rucom.h 2009-08-11 20:53:32.656250000 +0200
@@ -11,4 +11,4 @@
     & nocas, nopart, npart(6), nexite, negex, lowaz, negaz, nrnorm(4), /**ru    11*/
     & ihie, mnuc, nobalc, ifisct, ipht, irejpi, iexisa, instab(lpt), /**ru    12*/
     & nph, icc, iccem, ielas, iexp, isprd, ielast, ityp1, ktalres, /**ru6e   1*/
-   & iclaq,ihiona, ihionz /**ru6e   2*/
+   & iclaq,ihiona, ihionz, uoo(3) /**ru6e   2*/
diff -Nur v260/src/mcnp/histp/wrt_histp.F v260.ssntd/src/mcnp/histp/wrt_histp.F
--- v260/src/mcnp/histp/wrt_histp.F 2008-05-02 20:45:18.000000000 +0200
+++ v260.ssntd/src/mcnp/histp/wrt_histp.F 2009-08-11 22:55:36.281250000 +0200
@@ -174,8 +174,24 @@
```

```

!
! residual nucleus records
do 160 i=1,mnuc
+! write (nhstp) real(aprr(i)),real(zpr(i)),real(erecr(i)),
+! & real(uur(i)),real(ecvr(i)),real(ur(i)),real(vr(i)),real(wr(i))
+ zqur=ur(i)
+ zqvvr=vr(i)
+ zqwr=wr(i)
+ svn=sqrt(uoo(1)**2+uoo(2)**2)
+ if(svn.gt.1e-10) then
+ zqcb=uoo(3)
+ zqsb=svn
+ zqcr=uoo(1)/svn
+ zqsr=uoo(2)/svn
+ zqur=ur(i)*zqcb*zqcr-vr(i)*zqsr+wr(i)*zqsb*zqcr
+ zqvvr=ur(i)*zqcb*zqsr+vr(i)*zqcr+wr(i)*zqsb*zqsr
+ zqwr=-ur(i)*zqsb+wr(i)*zqcb
+ endif
+! write(*,'(3e23.5)') wr(i)*zqsb*zqsr
write (nhstp) real(aprr(i)),real(zpr(i)),real(erecr(i)),
- & real(uur(i)),real(ecvr(i)),real(ur(i)),real(vr(i)),real(wr(i))
+ & real(uur(i)),real(ecvr(i)),real(zqur),real(zqvvr),real(zqwr)
160 continue
nwrds=1+nwrds+8*mnuc
!
diff -Nur v260/src/mcnp/lcs/interact.F v260.ssntd/src/mcnp/lcs/interact.F
--- v260/src/mcnp/lcs/interact.F 2008-05-02 20:45:19.000000000 +0200
+++ v260.ssntd/src/mcnp/lcs/interact.F 2009-08-11 20:52:31.906250000 +0200
@@ -97,6 +97,9 @@
w7=w
mtl=med
nmed7=med
+ uoo(1)=u
+ uoo(2)=v
+ uoo(3)=w
#endif
call set_i
lter = 0

```

=====

Appendix F

MCNPX and HTAPE3X Input Files for SSNTD

F.1 MCNPX Input File

```
C *****Start*****
C Angle Response of Makrofol
C ----- Cell Cards -----
666 666 -1.2 -666
2 0 666 -1
3 0 1

C ----- Surface Cards -----
1 rpp -100 100 -100 150 -100 100
666 rpp -1 1 -0.05 0.05 -1 1

*TR1 0 0 0 15 -75 90 105 15 90 90 90 0 $ rotate 15 degrees
*TR2 0 0 0 30 -60 90 120 30 90 90 90 0 $ rotate 30 degrees
*TR3 0 0 0 45 -45 90 135 45 90 90 90 0 $ rotate 45 degrees
*TR4 0 0 0 60 -30 90 150 60 90 90 90 0 $ rotate 60 degrees
*TR5 0 0 0 75 -15 90 165 75 90 90 90 0 $ rotate 80 degrees
*TR6 0 0 0 90 0 90 180 90 90 90 90 0 $ rotate 90 degrees
mode N
cut:n 2j 0 0
m666 1001.66C 14 6012.50C 16 8016.66C 3 $Makrofol, density = 1.2 g/cm3
mx666:N j model model
imp:n 1 1 0
sdef ERG D1 POS 0 100 0 PAR 1 VEC 0 -1 0 DIR D2
SP7 -3 1.180000 1.03419
SI2 0.999 1
SP2 0 1
nps 1637559971 $10 mSv
histp 666
C *****End*****
```

F.2 HTAPE3X Input File

```
read histp file
$ damage production
16,1,,,1,,1.0/
90000/
666/
```

Appendix G

Neutron Physics in Geant4

```
G4ProcessManager* pManager = 0;
pManager = G4Neutron::Neutron() ->GetProcessManager();

G4HadronElasticProcess* neutronElasticProcess
    = new G4HadronElasticProcess("elastic-neutron");

G4LElastic* neutronElasticModel = new G4LElastic();
neutronElasticModel ->SetMinEnergy(19.8 * MeV);

G4NeutronHPElastic* neutronHPElasticModel
    = new G4NeutronHPElastic();

G4NeutronHPElasticData* neutronHPElasticCrossSection
    = new G4NeutronHPElasticData();

neutronElasticProcess ->RegisterMe(neutronElasticModel);
neutronElasticProcess ->RegisterMe(neutronHPElasticModel);
neutronElasticProcess ->AddDataSet(neutronHPElasticCrossSection);

pManager ->AddDiscreteProcess(neutronElasticProcess);

G4NeutronInelasticProcess* neutronInelasticProcess
    = new G4NeutronInelasticProcess("inelastic-neutron");

G4BinaryCascade* neutronBinaryCascadeModel
    = new G4BinaryCascade();
neutronBinaryCascadeModel ->SetMinEnergy(19.80 * MeV);
neutronBinaryCascadeModel ->SetMaxEnergy(10. * GeV);

G4NeutronHPInelastic* neutronHPInelasticModel
    = new G4NeutronHPInelastic();

G4NeutronHPInelasticData* neutronHPInelasticCrossSection
    = new G4NeutronHPInelasticData();

neutronInelasticProcess ->RegisterMe(neutronBinaryCascadeModel);
neutronInelasticProcess ->RegisterMe(neutronHPInelasticModel);
neutronInelasticProcess ->AddDataSet(neutronHPInelasticCrossSection);
```

```
pManager ->AddDiscreteProcess(neutronInelasticProcess);

G4HadronCaptureProcess* neutronCaptureProcess
    = new G4HadronCaptureProcess("capture-neutron");

G4LCapture* neutronLCaptureModel = new G4LCapture();
neutronLCaptureModel ->SetMinEnergy(19.8 * MeV);
neutronLCaptureModel ->SetMaxEnergy(100. * TeV);

G4NeutronHPCapture* neutronHPCaptureModel
    = new G4NeutronHPCapture();

G4NeutronHPCaptureData* neutronHPCaptureCrossSection
    = new G4NeutronHPCaptureData();

neutronCaptureProcess ->RegisterMe(neutronLCaptureModel);
neutronCaptureProcess ->RegisterMe(neutronHPCaptureModel);
neutronCaptureProcess ->AddDataSet(neutronHPCaptureCrossSection);

pManager ->AddDiscreteProcess(neutronCaptureProcess);

G4HadronFissionProcess* neutronFissionProcess
    = new G4HadronFissionProcess("fission-neutron");

G4LFission* neutronLFissionModel = new G4LFission();
neutronLFissionModel ->SetMinEnergy(19.8 * MeV);
neutronLFissionModel ->SetMaxEnergy(100. * TeV);

G4NeutronHPFission* neutronHPFissionModel
    = new G4NeutronHPFission();

G4NeutronHPFissionData* neutronHPFissionCrossSection
    = new G4NeutronHPFissionData();

neutronFissionProcess ->RegisterMe(neutronLFissionModel);
neutronFissionProcess ->RegisterMe(neutronHPFissionModel);
neutronFissionProcess ->AddDataSet(neutronHPFissionCrossSection);

pManager ->AddDiscreteProcess(neutronFissionProcess);
```

Appendix H

Algorithm for Track Density Correction

```
double calFactor(double density) //Calculate density factor for the density
{
    if(density <= 0) return 1.0;

    double Nmin=10000; //Maximum track number for the calculation
    double SK=1; //Size factor
    double NN=density; //Number of tracks in 1 cm^2
    if(NN<Nmin)
    {
        SK=sqrt(Nmin/NN);
        NN=Nmin;
    }

    x=new double[int(NN)]; //X coordinate
    y=new double[int(NN)]; //Y coordinate
    r=new double[int(NN)]; //radius
    o=new double[int(NN)]; //Flag, which indicates if the track is removed

    double nr=0; //Number of used random numbers

    double rand=0;

    //Set random number seed for Mersenne Twister random number generator
    init_genrand(19820520L);

    for(int i=0;i<int(NN);i++)
    {
        //Tracks uniformly distributes in the counting region.
        x[i] = genrand_real1()*SK;
        y[i] = genrand_real1()*SK;
        o[i] = 1;

        rand = genrand_real1();
        if(constDiameter)
            r[i]=constantDiameter/2; //Constant Diameter
        else
        {
            for(int j=0;j<p.size();j++)
            {
                if(rand<p[j])
                {
                    //Simple the radius in different ways.
                    if(discrete) //Discrete energies
                        r[i]=v[j]/2.0;
                    else //Histogram
                    {
                        if(j>0) r[i]=(v[j-1] + genrand_real1()*(v[j]-v[j-1]))/2.0;
                        else r[i]=genrand_real1()*v[j]/2.0;
                    }
                }
            }
        }
    }
}
```

```
        }
        break;
    }
}
nr = nr+3;
}

double NNn=NN;
for(int i=0;i<int(NN)-1;i++)
{
    for(int j=i+1;j<int(NN);j++)
    {
        double rt=min(r[i],r[j]);
        //Removing the track with smaller radius when two tracks are too close.
        //olFactor is overlapping factor for the calculation.
        if( o[i]!=0 && o[j]!=0 &&
            (pow(y[i]-y[j],2.0) + pow(x[i]-x[j],2.0))
            < pow(k*(r[i]+r[j] - olFactor*rt),2.0) )
        {
            NNn=NNn-1.0;
            if(r[i]<r[j])
                o[i]=0;
            else
                o[j]=0;
        }
    }
}

return NNn/NN; //Return the density correction factor
}
```

Appendix I

SSNTDKIT Manual

SSNTDKIT, Solid State Nuclear Track Detector toolKIT, has been developed to analyze the recoil data generated by Monte Carlo codes and to count tracks in detectors.

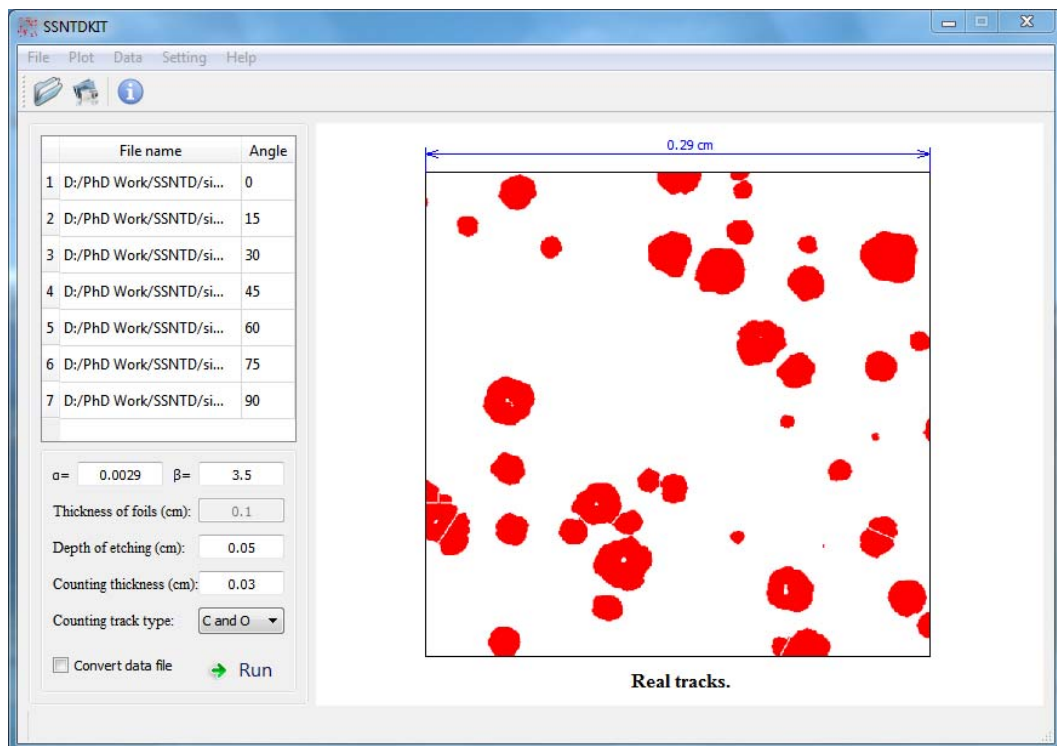


Figure I.1: SSNTDKIT User Interface.

I.1 User Interface

SSNTDKIT based on Qt libraries uses a graphical user interface (GUI). Like other GUI programs, it comprises a menu bar, a tool bar, a status bar and a working area (see Figure I.1). The menu bar integrates all functions of the programs while the tool bar only has a few buttons for quickly performing functions. The working area is divided into two parts. The left part is used to input parameters of track counting while the right part is for plotting results.

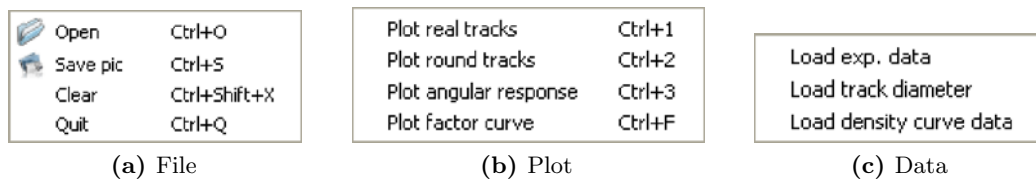


Figure I.2: Contents of menus.

I.1.1 Menus

There are five menus on the menu bar. Each menu is responsible for a set of tasks (see Figure I.2).

File is in charge of file operation including quitting the program, opening, closing and saving data.

Plot launches different plotting functions.

Data loads data for calculating and plotting.

Setting sets necessary parameters for calculating and plotting.

Help shows program and help information.

	File name	Angle
1	D:/PhD Work/SSNTD/si...	0
2	D:/PhD Work/SSNTD/si...	15
3	D:/PhD Work/SSNTD/si...	30
4	D:/PhD Work/SSNTD/si...	45
5	D:/PhD Work/SSNTD/si...	60
6	D:/PhD Work/SSNTD/si...	75
7	D:/PhD Work/SSNTD/si...	90

Figure I.3: Files of recoil data.

Figure I.4: Counting parameters.

I.1.2 Working Area

The left part of Figure I.1 shows the names of files which include the information of recoils and sets parameters for the track counting (see Figure I.3 and I.4).

α and β are the constant factors in Equation 3.9.

”**Thickness of foils**” sets the thickness of the detector pair, which is only used to process the original recoil data.

”**Depth of etching**” indicates the start position of etchings in the detector pair, which is respected to the front surface of the detector pair.

”**Counting thickness**” is the thickness of the counting layer, which is recommended to use a relatively large value to reduce errors.

”**Counting track type**” assigns which type of recoils should be taken into account in the counting.

”**Convert data file**” tells the program whether to process the original input files and produce a new file. If it is not chosen, data files will be used for counting directly.

The right part of Figure I.1 shows the pictures of tracks, response curve, density correction factor curve and help information. Those plotting functions can be switched for one to another by clicking in the plot menu or using hot keys.

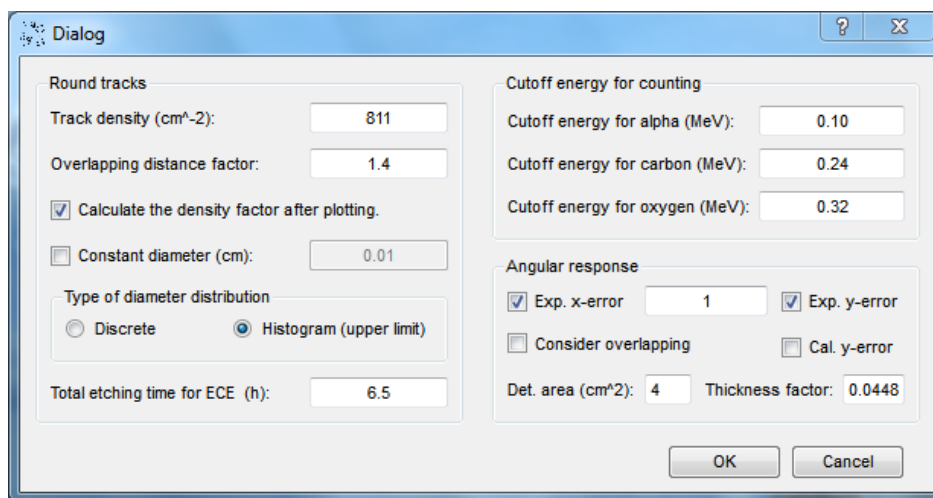


Figure I.5: Setting dialog.

I.1.3 Setting Dialog

The setting dialog (see Figure I.5) can be shown by clicking ”Setting” – ”Settings” on the menu bar. In this dialog, parameters which are relevant to track counting, plotting and density correction can be set. Some of important parameters are listed below:

”**Track density**” gives the track density for plotting round tracks.

”**Calculate the density factor after plotting**” tells the program whether to calculate the density correction factor after plotting.

”**Constant diameter**” means that a constant diameter is used for simulated round tracks.

”**Type of diameter distribution**” tells the program that the diameter data represent discrete energies or a histogram spectrum (upper limit of the energy).

”**Total etching time for ECE**” is not used in this work.

”**Cutoff energy for counting**” sets the energy thresholds of track counting for different recoils.

”**Exp. x-error**” decides if the experimental x-axis error bars (error of angles) are plotted. ”Exp. y-error” and ”Cal. y-error” options have similar functions.

”Consider overlapping” sets if track overlapping effect is taken into account. If it is chosen, SSNTDKIT will calculate the density correction factor for each track density and the track densities will be multiplied by the factor.

”Det. area” is the detector area, which is used to calculate the track density.

”Thickness correction factor” is a constant, which can be used to correct the thickness of the counting layer and to convert the number of tracks into track density. The results will be multiplied by this factor after the counting.

I.2 Functions

I.2.1 Track Counting

SSNTDKIT can read the recoil data generated by Monte Carlo codes with a specific format and process the data for track counting.

First open the recoil data files by clicking **”File” – ”Open”** and set the neutron incident angle for each file by clicking in the table next to the cell where the file name is shown. If the data files are originally generated by Monte Carlo codes, choose the **”Convert data file”** check box. New files, which include track path information, will be named by the original file name plus a **”.out”** suffix. If the files are already processed, do not choose the check box. Then set other parameters for track counting and click the **”Run”** button to start track counting.

Based on the REL value calculated with SRIM, the critical angle for different recoils is calculated. SSNTDKIT counts the number of tracks, using the critical angle and energy threshold rule.

When the counting is finished the relative angular response curve will be given in the plotting area together with the experimental results (see Figure I.6), the default name of which is **”exp.txt”** in the **”data”** sub-folder of the SSNTDKIT program directory. Experimental results can also be loaded by clicking **”Data” – ”Load exp. data”**.

A file called **”SSNTDOut.txt”** in the working directory will be generated after the track counting, containing the number of tracks for different angles of incident neutrons, relative errors and density correction factors (if they were calculated).

I.2.2 Plotting Round Tracks

Using the Monte Carlo method, SSNTDKIT samples track positions and diameters, and plot tracks (see Figure I.7). The sampling of positions is based on uniform distribution, and the diameters are based on experiments. The default file name of experimental results is **”trackdiameter.txt”** in the **”data”** sub-folder. The data can also be loaded by clicking **”Data” – ”Load track diameter”**. The shape of tracks is considered as round.

If **”Calculate the density factor after plotting”** check box is chosen, SSNTDKIT will calculate the density correction factor and show it below the picture.

I.2.3 Calculation of Density Factors

Density correction factors for different track densities can be calculated with SSNTDKIT using the Monte Carlo method. Density factor curves can be plotted (see Figure I.8).

The default file name of experimental results is **”expfac.txt”** in the **”data”** sub-folder. The data can also be opened by clicking **”Data” – ”Load density curve data”**.

The calculation for different track densities needs rather long time, so it will be only performed once every time after launching SSNTDKIT if no parameter is changed.

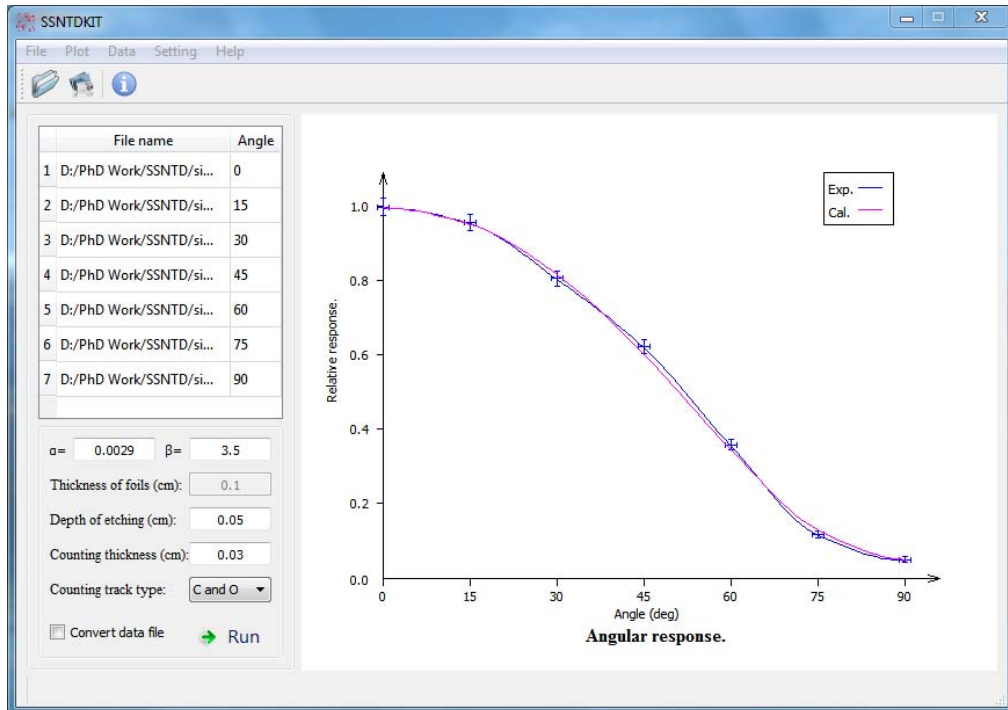


Figure I.6: Angular response.

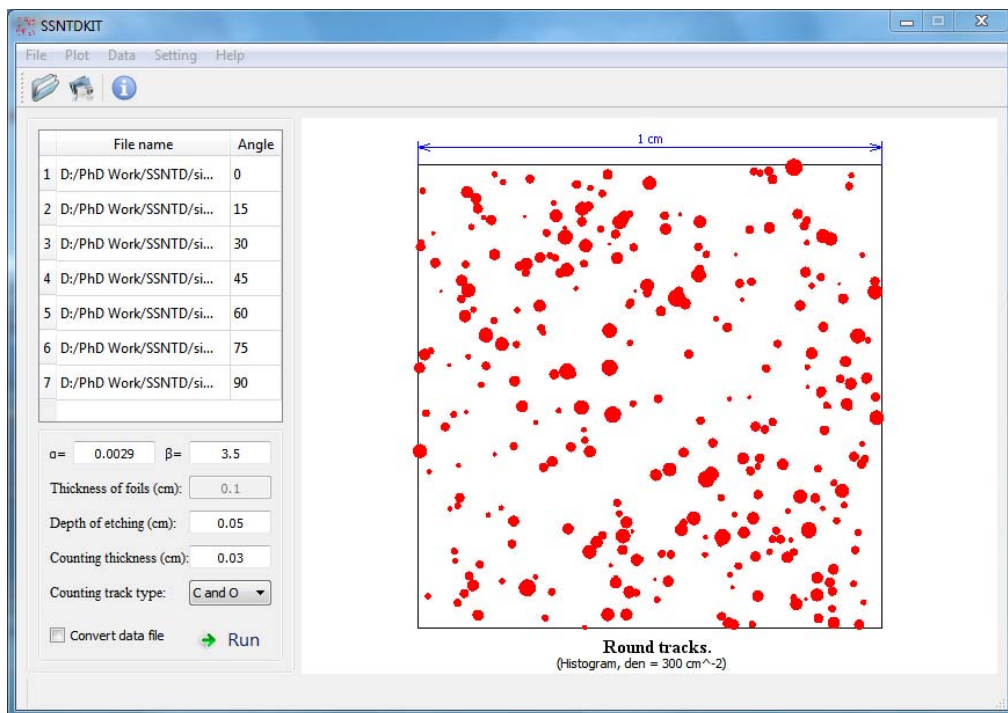


Figure I.7: Round tracks.

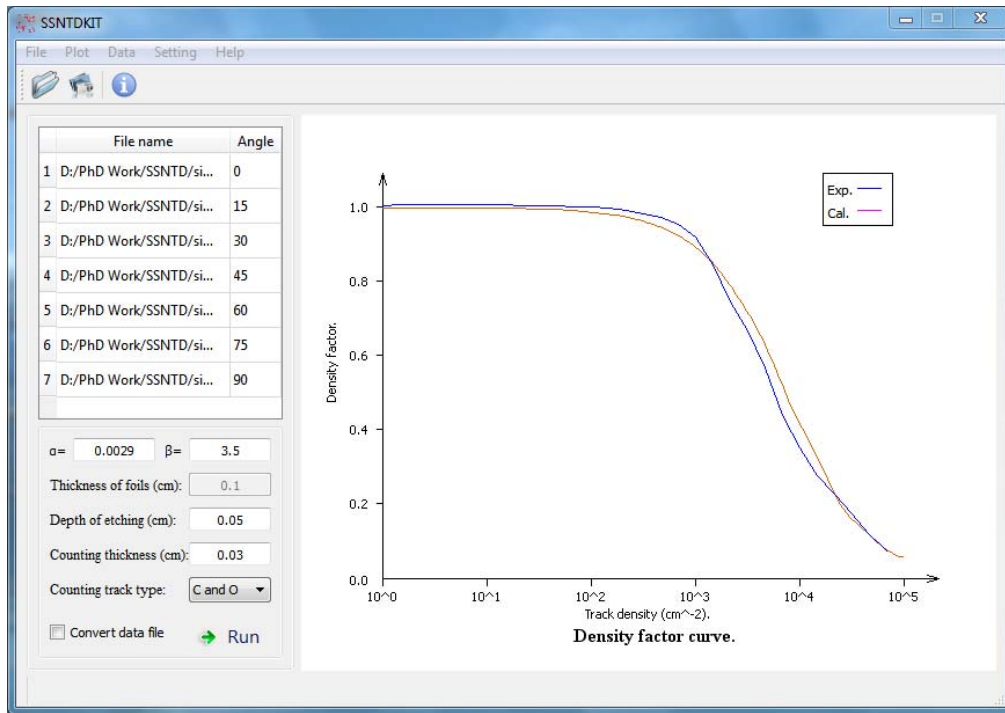


Figure I.8: SSNTDKIT density factors.

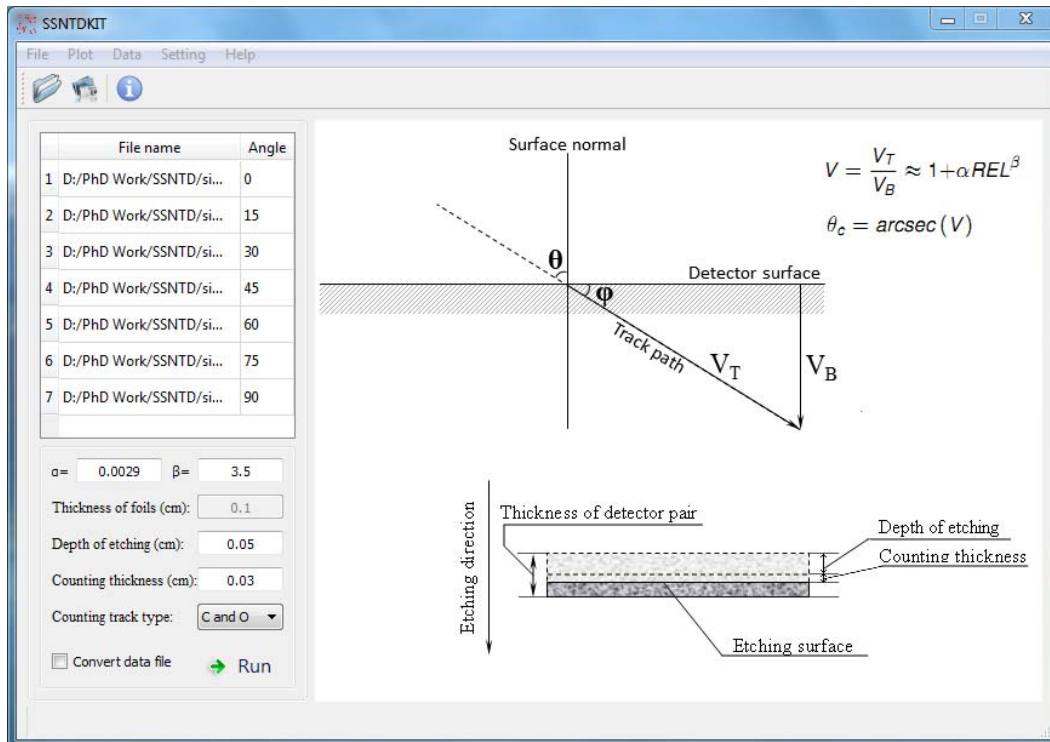


Figure I.9: Help information.

I.3 Help Information

Clicking "Help" – "Help" or using the "F1" hot key shows the sketch of critical angle and track etching (see Figure I.9). The meaning of some parameters are described here in detail.

Clicking "Help" – "Manual" opens this manual in a default pdf viewer for your operating system.

In the plotting area, right-clicking shows a pop-up menu which helps to copy and save the current picture in the area in PNG format.

Some often used functions have a hot key. Using hot keys instead of clicking on the menu bar can save time.

The setup of Makrofol detectors and the neutron source in Monte Carlo simulations can be found in Figure I.10. The center of the detector pair locates at the origin. The surfaces of the detectors are perpendicular to the y-axis and parallel to the x-axis. The neutron source is positioned on the positive side of the y-axis. For different incident angles, detectors rather than the source are rotated around the z-axis counter-clockwise.

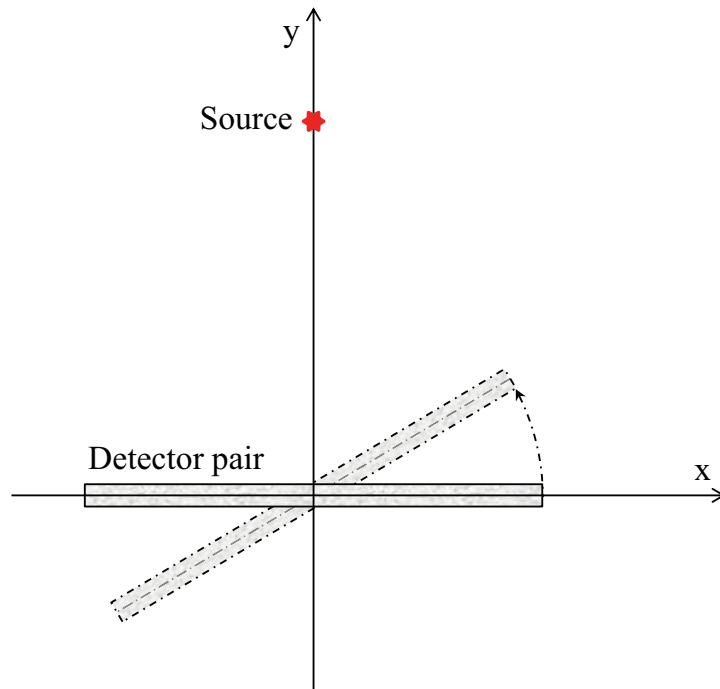


Figure I.10: Setup of Makrofol a detector pair and a neutron source in the simulations. The z-axis, which is not plotted, points out the plane of the paper.

Appendix J

Experimental Data and Two-Step ECE Protocol

The data in table J.1 were obtained with the detectors irradiated at KIT. The activity of Cf-252 source was 2.06×10^6 Bq. The total dose was 2.762 mSv. The distance between the neutron source and detectors is 70 cm.

The data in table J.2 were obtained with the detectors irradiated at PSI. The activity of Cf-252 source was 2.258×10^9 Bq. The total dose was 10 mSv. The distance between the neutron source and detectors was 1 m.

All irradiated detectors were etched in the KIT solid state dosimetry laboratory with the standard two-step ECE procedure (see Section 3.5.2.5). The number of tracks is counted with an auto-analyzing system.

Table J.1: Experimental Results at KIT.

Det. No.	Angle (deg)	Number of tracks in different regions of detector surface																Area per region (cm^2)
		1	2	3	4	5	6	7	8	9	10	11	12	13	14	15	16	
1B ¹	0	30	24	26	25	36	31	33	25	38	26	27	36	31	20	30	24	0.079845614
2B	15	29	26	30	26	27	26	28	24	32	33	31	31	27	31	29	20	0.079845614
3B	30	27	23	26	18	31	19	22	26	24	21	32	28	29	31	26	18	0.079845614
4B	45	17	12	14	15	21	21	20	13	15	22	17	20	22	31	24	20	0.079845614
5B	60	16	10	8	15	13	7	13	10	11	7	8	10	6	9	13	12	0.079845614
6B	75	3	6	5	2	5	3	4	5	4	6	4	4	6	7	7	9	0.079845614
7B	90	1	6	5	6	3	2	6	5	4	3	3	4	9	7	6	7	0.079845614
8B	N/A	2	2	2	1	4	4	1	3	2	2	8	5	1	4	3	5	0.079845614
9B	N/A	2	0	1	3	2	2	2	2	1	3	2	2	3	6	5	3	0.079845614
10B	N/A	2	2	2	4	2	3	5	4	0	1	3	3	2	0	3	3	0.079845614
11B	N/A	5	1	2	1	2	5	2	2	5	0	3	2	7	0	1	1	0.079845614
12B	N/A	1	5	3	2	3	3	3	1	0	2	3	5	0	1	3	3	0.079845614
13B	N/A	1	2	0	4	3	2	4	2	8	3	2	2	2	2	0	2	0.079845614
1F ²	0	25	31	22	22	15	20	24	26	26	28	32	33	22	24	24	21	0.079845614
2F	15	28	23	28	20	15	25	20	15	30	26	30	29	22	25	33	24	0.079845614
3F	30	19	17	24	18	18	29	23	27	30	20	22	21	13	19	25	12	0.079845614
4F	45	11	11	18	17	3	16	20	18	16	12	16	15	12	21	11	24	0.079845614
5F	60	10	9	6	6	12	12	9	7	9	6	9	9	7	4	6	11	0.079845614
6F	75	4	3	2	5	4	2	2	6	4	3	6	2	1	3	7	5	0.079845614
7F	90	5	3	10	2	5	2	5	5	2	2	0	5	2	2	5	3	0.079845614
8F	N/A	3	4	1	3	1	3	2	2	1	2	3	3	1	3	2	3	0.079845614
9F	N/A	2	3	1	2	4	2	2	2	4	4	2	3	5	1	0	2	0.079845614
10F	N/A	1	1	3	5	1	2	0	2	3	4	1	4	3	1	2	3	0.079845614
11F	N/A	4	1	1	2	0	2	4	5	4	2	5	3	3	3	5	4	0.079845614
12F	N/A	2	1	1	1	2	2	3	1	1	2	2	4	1	1	2	3	0.079845614

¹B: Detector on the rear side²F: Detector on the front side

Table J.1: (continued).

Det. No.	Angle (deg)	Number of tracks in different regions of detector surface																Area per region (cm^2)
		1	2	3	4	5	6	7	8	9	10	11	12	13	14	15	16	
13F	N/A	3	4	1	2	1	2	1	3	2	1	3	2	2	3	4	1	0.079845614

Table J.2: Experimental Results at PSI.

Det. No.	Angle (deg)	Number of tracks in different regions of detector surface																Area per region (cm^2)
		1	2	3	4	5	6	7	8	9	10	11	12	13	14	15	16	
1B	0	61	65	66	71	77	62	60	71	64	63	64	68	61	57	73	68	0.079845614
2B	0	64	53	70	75	70	63	77	78	58	86	73	62	63	64	81	57	0.079845614
3B	15	67	59	54	64	69	62	63	72	65	68	59	64	60	66	68	72	0.079845614
4B	15	60	64	67	74	71	61	59	63	61	65	62	73	59	63	60	64	0.079845614
5B	30	57	53	47	47	58	57	50	45	42	52	59	48	52	64	55	57	0.079845614
6B	30	55	58	60	52	63	59	52	60	48	56	52	51	57	70	60	49	0.079845614
7B	45	37	41	55	47	46	38	45	45	34	45	35	44	41	47	47	48	0.079845614
8B	45	40	48	46	44	38	45	39	44	34	39	44	38	44	48	36	42	0.079845614
9B	60	18	28	24	29	26	24	22	21	28	24	24	31	31	38	21	28	0.079845614
10B	60	28	29	16	19	29	29	28	22	30	17	27	22	28	25	28	22	0.079845614
11B	75	7	7	11	12	10	11	14	13	12	14	7	7	10	9	8	11	0.079845614
12B	75	17	6	8	9	19	7	7	5	12	7	6	14	11	11	7	8	0.079845614
13B	90	4	6	11	6	7	3	3	5	5	5	4	5	2	3	7	12	0.079845614
14B	90	6	4	5	9	3	5	4	6	8	5	5	6	7	5	3	7	0.079845614
15B	N/A	0	2	3	3	3	2	1	2	2	2	2	5	1	3	2	4	0.079845614
16B	N/A	3	1	0	2	1	0	0	3	5	1	3	5	0	1	4	4	0.079845614
17B	N/A	1	2	2	3	1	1	3	3	2	3	1	3	2	2	4	2	0.079845614
18B	N/A	3	0	4	3	2	5	5	1	3	0	2	2	3	2	4	3	0.079845614
19B	N/A	1	2	2	2	5	2	1	3	2	2	3	0	2	1	2	4	0.079845614
20B	N/A	4	2	3	4	0	2	2	1	4	2	5	1	6	3	4	0	0.079845614
1F	0	52	57	64	62	57	62	68	65	57	54	67	57	56	62	62	63	0.079845614
2F	0	64	72	69	54	58	52	56	68	57	56	56	61	61	64	72	61	0.079845614
3F	15	71	69	57	58	79	62	58	53	60	62	67	49	67	52	63	64	0.079845614
4F	15	47	53	61	62	54	64	66	66	56	64	59	55	48	57	48	55	0.079845614
5F	30	52	53	46	48	38	55	50	44	56	58	41	40	51	50	48	47	0.079845614
6F	30	46	54	48	48	47	41	50	52	42	56	44	57	53	59	49	46	0.079845614
7F	45	37	39	34	30	37	42	36	43	36	45	37	32	39	45	45	40	0.079845614

Table J.2: (continued).

Det. No.	Angle (deg)	Number of tracks in different regions of detector surface																Area per region (cm^2)
		1	2	3	4	5	6	7	8	9	10	11	12	13	14	15	16	
8F	45	29	28	31	25	44	36	36	32	40	33	26	26	34	31	42	35	0.079845614
9F	60	20	19	21	22	18	21	23	21	30	26	35	18	23	22	28	21	0.079845614
10F	60	17	20	16	12	22	24	16	18	21	28	12	23	19	22	31	28	0.079845614
11F	75	7	5	4	9	13	7	9	9	11	8	9	6	18	16	8	12	0.079845614
12F	75	15	10	10	11	9	8	11	12	10	10	13	12	16	9	7	13	0.079845614
13F	90	3	5	6	1	3	6	9	6	3	3	6	3	5	3	4	7	0.079845614
14F	90	8	7	1	2	5	4	5	3	4	6	6	6	7	6	7	4	0.079845614
15F	N/A	2	3	1	2	1	0	3	1	3	0	2	4	1	3	3	3	0.079845614
16F	N/A	1	2	1	2	4	4	5	3	3	1	1	0	4	3	3	3	0.079845614
17F	N/A	3	2	3	2	2	3	3	3	2	0	1	0	2	1	5	3	0.079845614
18F	N/A	2	1	2	3	2	3	1	2	5	1	5	4	3	5	2	3	0.079845614
19F	N/A	4	2	1	1	3	0	3	1	1	3	2	1	5	0	3	3	0.079845614
20F	N/A	2	0	1	1	1	2	1	1	5	4	2	2	3	1	0	3	0.079845614

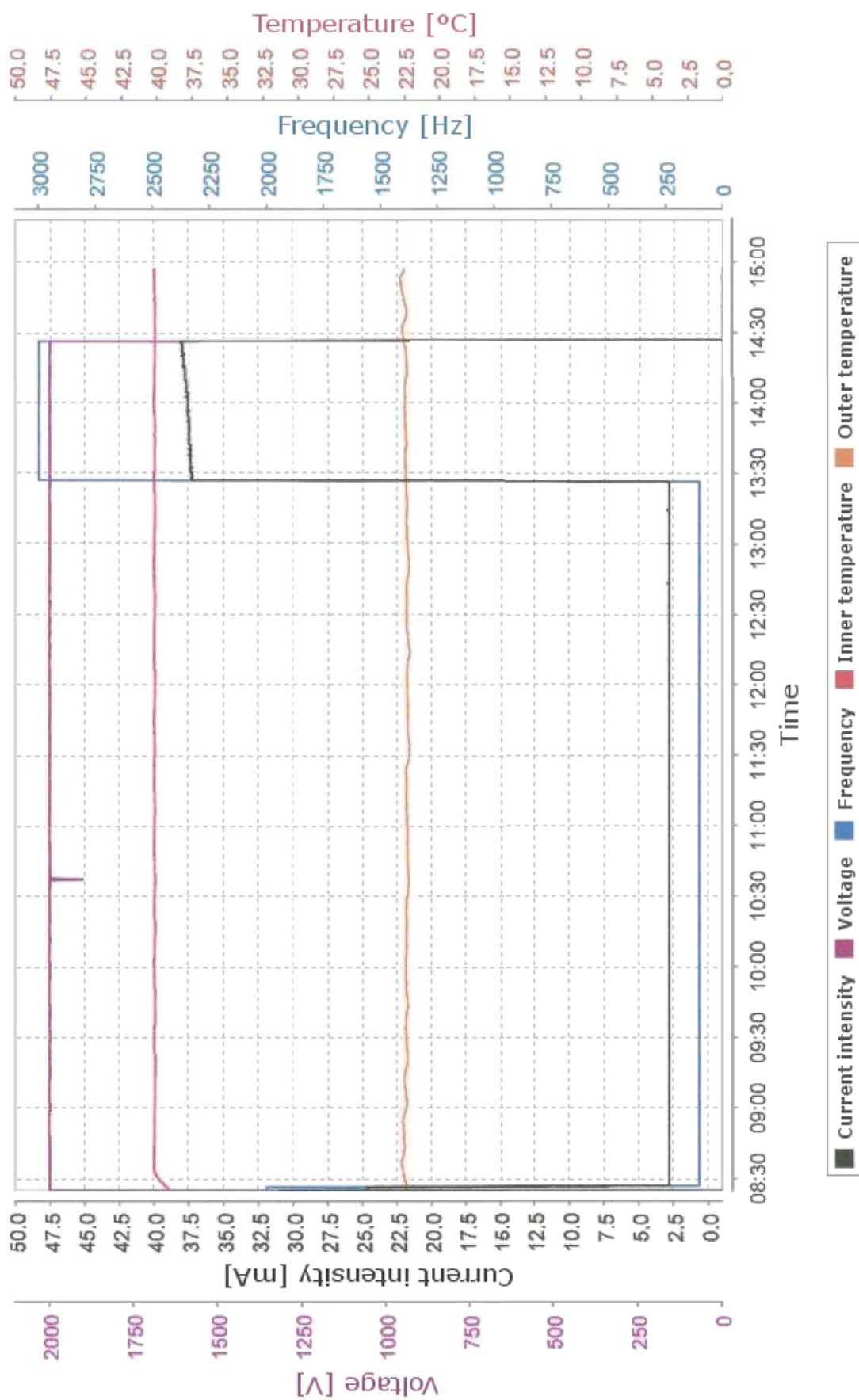


Figure J.1: The protocol of the standard two-step ECE at KIT.

Bibliography

- Agostinelli, S., Allison, J., Amako, K., Apostolakis, J., Araujo, H., Arce, P., Asai, M., Axen, D., *et al.* GEANT4: A simulation toolkit. *Nuclear Instruments and Methods*, A506:250–303, 2003.
- Badash, L. Manhattan Project. Grolier Multimedia Encyclopedia. 2011. URL <http://gme.grolier.com/article?assetid=0183730-0> (March 2011).
- Bayer Films Americas. Product Data: Makrofol DE 1-4. 2011. URL http://www.bayerfilms.com/pc/web_docs/Makrofol_DE_1-4.pdf (March 2011).
- Beton, E. V. and Nix, W. D. The restricted energy loss criterion for registration of charged particles in plastics. *Nuclear Instruments and Methods*, 67:343–347, 1969.
- Bichsel, H., Groom, D. E., and Klein, S. R. Passage of particles through matter. *Jouranal of Physics G*, 33(1), 2006.
- Booth, T. E. A Sample Problem for Variance Reduction in MCNP. Tech. Rep. LA-10363-MS, Los Alamos National Laboratory, 1985.
- Booth, T. E. MCNP Variance Reduction Examples. 2004. URL <http://mcnp-green.lanl.gov/documentation/vrexamples2.pdf> (March 2011).
- Booth, T. E., Brown, F. B., Bull, J. S., Forster, R. A., Goorley, J. T., Hughes, H. G., Martz, R. L., Prael, R. E., *et al.* MCNP5 1.50 Release Notes. Tech. Rep. LA-UR-08-2300, Los Alamos National Laboratory, 2008.
- Börst, F.-M., Rimpler, A., and Scheib, H. Strahlungsmessungen an Transport- und Lagerbehältern zur Beförderung von hochaktiven Glaskokillen aus der Wiederaufarbeitung und von bestrahlten Brennelementen. Tech. Rep. BfS-ET-32/00, Bundesamt für Strahlenschutz, 2000.
- Bramblett, R. L., Ewing, R. I., and Bonner, T. W. A new type of neutron spectrometer. *Nuclear Instruments and Methods*, 9:1–12, 1960.
- Burgkhardt, B., Ambrosi, P., and Rimpler, A. Einsatz von Albedodosimetern zur Messung kleiner Dosen in gemischten Photonen-Neutronen-Strahlungsfeldern an Transportbehältern für hochradioaktiven Abfall. Tech. Rep. FZKA 6217, Forschungszentrum Karlsruhe, 2000.
- Burgkhardt, B. and Piesch, E. Field calibration technique for albedo neutron dosimeters. *Radiation Protection Dosimetry*, 23(1/4):121–126, 1988.

- Cecchini, S., Cozzi, M., Ferdinando, D. D., Errico, M., Fabbri, F., Giacomelli, G., Giacomelli, R., Giorgini, M., *et al.* Results of the search for strange quark matter and Q-balls with the SLIM experiment. *The European Physical Journal C - Particles and Fields*, 57:525–533, 2008.
- Cullen, D. E. Sampling ENDL watt fission spectra. Tech. Rep. UCRL-TR-203351, Lawrence Livermore National Laboratory, 2004.
- Dörschel, B., Fülle, D., Hartmann, H., Hermsdorf, D., Kadner, K., and Radlach, C. Dependence of the etch rate ratio on the energy loss in proton irradiated CR-39 detectors and recalculation of etch pit parameters. *Radiation Protection Dosimetry*, 71(2):99–106, 1997.
- Durrani, S. A. and Bull, R. K. *Solid State Nuclear Track Detection*. Pergamon Press, Headington Hill Hall, Oxford OX3 0BW, England, 1987.
- El-Fiki, M. A., Fadel, M. A., Sharaf, M. A., Rabie, N., and Hassib, G. M. Optimization of ECE of CR-39 and Makrofol-E at frequencies up to 1 MHz. *Nuclear Tracks*, 12(1-6):189–192, 1986.
- EnBW Kraftwerke AG. Kurzbeschreibung Zwischenlager für das Kernkraftwerk Philippsburg. 2001.
- EnBW Kraftwerke AG. Uranium is energy. 2011. URL http://www.enbw.com/content/en/group/_media/_pdf/kernenergiebrosch__re_englisch.pdf (March 2011).
- E.ON Kernkraft. Brokdorf - Information on the Power Plant. 2011. URL http://www.eon-kernkraft.com/pages/ekk_de/Standorte/_documents/Info_Standort_KBR_eng.pdf (March 2011).
- Everett, C. J. and Cashwell, E. D. A third monte carlo sampler. Tech. Rep. LA-9721-MS, LosAlamos National Laboratory, 1983.
- Fleischer, R. L., Price, P. B., and Walker, R. M. *Nuclear Tracks in Solids: Principles & Applications*. University of California Press, California, USA, 2008.
- Fritschek, R. Hochschule Furtwangen University, personal communication, 2009.
- Geant4 Collaboration. Introduction to Geant4. 2011. URL <http://geant4.web.cern.ch/geant4/UserDocumentation/Welcome/IntroductionToGeant4/html/introductionToGeant4.html#1>. (March 2011).
- Hassib, G. M. A pre-electrochemical etching treatment to improve neutron recoil track detection. *Nuclear Tracks*, 3:45–52, 1978.
- Hassib, G. M., Kasim, S. A., and Piesch, E. Neutron energy dependence of different track etch detectors. *Radiation Effects and Defects in Solids*, 45:57–60, 1979.
- Hendricks, J. S. MCNPX Model/Table Comparison. Tech. Rep. LA-14030, Pacific Northwest National Laboratory, 2003.
- Hermsdorf, D., Bretschneider, R., Dörschel, B., and Henniger, J. Neutron response calculation on the basis of variable track etch rates along the secondary particle trajectories in CR-39. *Radiation Measurements*, 31:431–436, 1999.
- Herzbach, L., Schenk, C., and Thiel, S. Werkzeug zur Heißformgebung von Glas oder Kunststoff. 2011. URL <http://www.patent-de.com/20011122/DE10022114A1.html> (March 2011).

- Horowitz, Y. S., Freeman, S., and Dubi, A. Limitations of the paired LiF TLD-600, 700 technique for the estimation of gamma ray dose in mixed n- γ radiation fields: The effect of thermal neutrons. *Nuclear Instruments and Methods*, 160:317–320, 1979.
- Hummelsheim, K. and Hesse, U. GRS Garching, personal communication, 2009.
- ICRP. *Recommendations of the ICRP*. No. 26 in ICRP Publication. ICRP, 1971.
- ICRP. *1990 Recommendations of the International Commission on Radiological Protection*. No. 60 in ICRP Publication. ICRP, 1991.
- ICRP. *Conversion Coefficients for use in Radiological Protection against External Radiation*. No. 74 in ICRP Publication. ICRP, 1997.
- ICRP. *The 2007 Recommendations of the International Commission on Radiological Protection*. No. 103 in ICRP Publication. ICRP, 2007.
- ICRU. *Quantities and Units in Radiation Protection Dosimetry*. No. 51 in ICRU Report. ICRU, Bethesda, MD, 1993.
- ICRU. *Fundamental Quantities and Units for Ionizing Radiation*. No. 60 in ICRU Report. ICRU, Bethesda, MD, 1998.
- ICRU. *Determination of operational dose equivalent quantities for neutrons*. No. 66 in ICRU Report. ICRU, Bethesda, MD, 2001.
- Józefowicz, K. Energy threshold for neutron detection in a makrofol dielectric track detector. *Nuclear Instruments and Methods*, 93:369–370, 1971.
- Józefowicz, K., Burgkhardt, B., Vilgis, M., and Piesch, E. Polycarbonate track detectors with a flat energy response for the measurement of high energy neutrons at accelerators and airflight altitudes. *Radiation Protection Dosimetry*, 70(1-4):143–148, 1997.
- Józefowicz, K. and Piesch, E. Electrochemically etched Makrofol de as a tetector for neutron induced recoils and alpha particles. *Radiation Protection Dosimetry*, 34(1/4):25–28, 1990.
- Kalsi, P. C., Ramaswami, A., and Manchanda, V. K. Solid state nuclear track detectors and their applications. 2011. URL <http://www.barc.ernet.in/publications/nl/2005/200506-2.pdf> (March 2011).
- Katz, R. and Kobetich, E. J. Formation of etchable tracks in dielectrics. *Physical Review*, 170(2):401–405, 1968.
- Khan, R. F. H., Ahmad, N., Aslam, and Matiullah. Studying the response of CR-39 detectors using the Monte Carlo technique. *Radiation Measurements*, 33:129–137, 2001.
- LANL. MCNP - A General Monte Carlo N-Particle Transport Code - Version 5. 2011. URL <http://mcnp-green.lanl.gov/> (March 2011).
- Matsumoto, M. and Nishimura, T. Mersenne twister: a 623-dimensionally equidistributed uniform pseudo-random number generator. *ACM Transactions on Modeling and Computer Simulation*, 8:3–30, 1998.
- Pang, T. *An Introduction to Computational Physics*. Cambridge University Press, 2nd edition, The Edinburgh Building, Cambridge CB2 2RU, UK, 2006.

- Pelowitz, D. B. MCNPX User's Manual Version 2.6.0. Tech. Rep. LA-CP-07-1473, Los Alamos National Laboratory, 2008.
- Piesch, E., Al-Najjarb, S. A. R., and Józefowicz, K. The two-step electrochemical etching technique applied for polycarbonate track etched detectors. *International Journal of Radiation Applications and Instrumentation. Part D. Nuclear Tracks and Radiation Measurements*, 19(1-4):205–210, 1991.
- Piesch, E. and Burgkhardt, B. Albedo neutron dosimetry. *Radiation Protection Dosimetry*, 10(1-4):175–188, 1985.
- Piesch, E. and Burgkhardt, B. Albedo dosimetry system for routine personnel monitoring. *Radiation Protection Dosimetry*, 23(1/4):117–120, 1988a.
- Piesch, E. and Burgkhardt, B. Erprobung eines Albedoneutronendosimetrie-system:TLD-Kalibrier- und Meßverfahren, Neutronenkalibrierung, dosimetrische Eigenschaften, Routineanwendung. Tech. Rep. KfK 4303, Hauptabteilung Sicherheit, 1988b.
- Piesch, E., Jasiak, J., and Urban, M. Makrofol and CR 39 Recoil Track Etch Detectors as a Supplement of a Universal Albedo Neutron Dosemeter. *Nuclear Tracks and Radiation Measurements*, 8(1-4):323–326, 1984.
- Prael, R. E. and Lichtenstein, H. *The LAHET Code System*. Los Alamos National Laboratory, 1989.
- Qashua, N., Ibrahim, A., and Waker, A. J. Dose rate effects on mixed field neutron-gamma dosimetry using a tissue equivalent proportional counter. In *Proceedings of International Workshop on Real Time Measurement, Instrumentation & Control*. Oshawa, ON, Canada, 2010.
- Rathbone, B. A. Hanford External Dosimetry Technical Basis Manual. Tech. Rep. PNL-MA-842, Pacific Northwest National Laboratory, 2011.
- Reese, G. Buffon's Needle - An Analysis and Simulation. 2011. URL <http://mste.illinois.edu/reese/buffon/buffon.html> (May 2011).
- Saint-Martin, G., Vernaola, O. A., Nemirovsky, I., and Filevich, A. Track detection threshold in makrofol e. new experimental data. *Radiation Measurements*, 26:733–735, 1996.
- Salvat, F., Fernández-Varea, J. M., and Sempau, J. *PENELOPE-2008 - A Code System for Monte Carlo Simulation of Electron and Photon Transport*, 2008.
- Schuhmacher, H., Bartlett, D., Bolognese-Milsztajn, T., Boschung, M., Coeck, M., Curzio, G., d'Errico, F., Fiechtner, A., *et al.* Evaluation of individual dosimetry in mixed neutron and photon radiation fields. Tech. Rep. PTB-N-49, PTB, 2006.
- Shultis, J. K. and Faw, R. E. An MCNP Primer. 2010. URL <http://www.mne.ksu.edu/~jks/MCNPprmr.pdf> (March 2011).
- Singh, S. and Prasher, S. A comparison of modifications induced by Li^{3+} and O^{6+} ion beam to Makrofol-KG and CR-39 polymeric track detectors. *Nuclear Instruments and Methods in Physics Research B*, 244:252–256, 2006.
- Somogyi, G., Grabisch, K., Scherzer, R., and Enge, W. Revision of the concept of registration threshold in plastic track detectors. *Nuclear Instruments and Methods*, 134:129–141, 1976.

- Sternheimer, R. M., Berger, M. J., and Seltzer, S. M. Density effect for the ionization loss of charged particles in various substances. *Atomic Data and Nuclear Data Tables*, 30:261–271, 1984.
- Straubing, A. Karlsruhe Institute of Technology, personal communication, 2009.
- Thomauske, B. R. Interim storage of spent nuclear fuel in Germany. In *Proceedings of Waste Management Conference*. Tucson, AZ, USA, 2002.
- Tommasino, L. Electrochemical etching of damage track detectors by h.v. pulse and sinusoidal wave forms. In *Proceedings of 7th Int. Coll. Corpuscular Phot. and Visual Solid Detectors*. Barcelona, Spain, 1970.
- Tommasino, L., Zapparoli, G., Spiezia, P., Griffith, R. V., and Espinosa, G. Different etching processes of damage track detectors for personnel neutron dosimetry. *Nuclear Tracks and Radiation Measurements*, 8(1-4):335–339, 1984.
- Urban, M. Passive One-Element Track Etch Dosimeter for Simultaneous Measurement of Radon, Thoron and Decay Products in Air. *Nuclear Tracks*, 12(1-6):685–688, 1986.
- Wagner, R. Mersenne Twister Random Number Generator. 2011. URL <http://www-personal.umich.edu/~wagnerr/MersenneTwister.html> (March 2011).
- Weisstein, E. W. Rotation Matrix. From MathWorld—A Wolfram Web Resource. 2011. URL <http://mathworld.wolfram.com/RotationMatrix.html> (March 2011).
- Williams III, R. G., Gesh, C. J., and Pagh, R. T. Compendium of material composition data for radiation transport modeling. Tech. Rep. PNNL-15870, Pacific Northwest National Laboratory, 2006.
- Young, D. A. Etching of radiation damage in lithium fluoride. *Nature*, 182:375–377, 1998.
- Zaki-Dizaji, H., Shahriariband, M., and Etaati, G. Calculation of CR-39 efficiency for fast neutrons using the MCNP and SRIM codes. *Radiation Measurements*, 43:283–285, 2008.
- Zhang, G., Becker, F., Urban, M., and Xuan, Y. Simulating Makrofol as a detector for neutron induced recoils. *Radiation Protection Dosimetry*, 144(1-4):218–221, 2011a.
- Zhang, G., Becker, F., Urban, M., Xuan, Y., Fürstner, M., and Mayer, S. Simulating the angular response of Makrofol as a detector for neutron induced recoils. *Radiation Measurements*, pp. 405–408, 2011b.
- Ziegler, J. F. The stopping and range of ions in matter. 2011. URL <http://www.srim.org/#SRIM> (March 2011).
- Ziegler, J. F., Biersack, J. P., and Ziegler, M. D. *SRIM - The Stopping and Range of Ions in Matter*. Ion Implantation Press, Annapolis, USA, 2008.

Publications During my PhD Study at KIT

1. G. Zhang, F. Becker, M. Urban, G. Cai, Shielding Calculation for a transport Tank for Intermediate Level Liquid wastes, in Proceedings of Annual Meeting on Nuclear Technology, Dresden, Germany, May 12-14, 2009
2. G. Zhang, R. Fritschek, F. Becker, M. Urban S. Prys, Shielding Calculations of a CASTOR with MCNP5, in Proceedings of Annual Meeting on Nuclear Technology, Berlin, Germany, May 4-6, 2010
3. G. Zhang, F. Becker, M. Urban, Y. Xuan, Simulating Makrofol as a Detector for Neutron Induced recoils, Radiation Protection Dosimetry, doi: 10.1093/rpd/ncq551, first published online: January 24, 2011
4. G. Zhang, F. Becker, M. Urban, MCNP Surface Source and CASTOR Simulations, in Proceedings of Annual Meeting on Nuclear Technology, Berlin, May, Germany, 17-19, 2011
5. G. Zhang, F. Becker, M. Urban, Y. Xuan, M. Fürstnerd, S. Mayer, Simulating The Angular Response of Makrofol as a Detector for Neutron Induced Recoils, Radiation Measurements, 46: 405-408, 2011

List of Abbreviations

AMD	Advanced Micro Devices, Inc
ANL	Argonne National Laboratory
ASF	Abteilung Strahlenschutzforschung - Division of Radiation Protection
BfS	Bundesamt für Strahlenschutz - Federal Office for Radiation Protection
CASTOR	CAsk for Storage and Transport Of Radioactive material - containers used to transport highly radioactive nuclear waste
CE	Chemical Etching
CENDL	Chinese Evaluated Nuclear Data Library
CERN	Conseil Européen pour la Recherche Nucléaire - European Organization for Nuclear Research
CIRP	China Institute for Radiation Protection
CSC	China Scholarship Council
ECE	Electro-chemical Etching
EGS	Electron Gamma Shower
EnBW	Energie Barden-Württemberg AG - A German energy company
ENDF	Evaluated Nuclear Data File
FLUKA	FLUktuierende KAskade
Geant4	Geometry and Tracking 4 - a Monte Carlo radiation transport code
GRS	Gesellschaft für Anlagen- und Reaktorsicherheit mbH - Society for Plant Safety and Reactor Safety
GUI	Graphical User Interface
HDB	Hauptabteilung Dekontaminationsbetriebe
HFU	Hochschule Furtwangen University
HS	Hauptabteilung Sicherheit - Central Safety Department
IBM	International Business Machines

ICRP	International Commission on Radiological Protection
ICRU	International Commission on Radiation Units and Measurements
INE	Institut für Nukleare Entsorgung - Institute for Nuclear Waste Disposal
INFN	Istituto Nazionale di Fisica Nucleare - National Institute for Nuclear Physics
ISF	Institut für Strahlenforschung - Institute for Radiation Research
KEK	Kō Enerugi Kasokuki Kenkyū Kikō - High Energy Accelerator Research Organization
KES	Kompetenzerhalt im Strahlenschutz - Maintenance of Radiation Protection Competence
KIT	Karlsruher Institut für Technologie - Karlsruhe Institute of Technology
KSM	KIT-Sicherheitsmanagement - KIT Safety Management
LANL	Los Alamos National Laboratory
MATLAB	Matrix Laboratory - a numerical computing environment and fourth-generation programming language
MCNP	Monte Carlo N-Particle
MCNPX	Monte Carlo N-Particle eXtended
MCU	Monte Carlo Universal
MPI	Message Passing Interface
NRC	National Research Council Canada
OO	Object-Oriented
ORNL	Oak Ridge National Laboratory
PENELOPE	PENetrating and Energy LOss of Positrons and Electrons
PSI	Paul Scherrer Institute
PTB	Physikalisch-Technische Bundesanstalt
REL	Restricted Energy Loss
SCC	Steinbuch Centre for Computing
SLAC	Stanford Linear Accelerator Center
SRIM	Stopping and Range of Ions in Matter
SSNTD	Solid State Nuclear Tracks Detector
SSNTDKIT	Solid State Nuclear Track Detector toolKIT
TLD	Thermoluminescent dosimeter
TRIM	Transport of Ions in Matter
WAK	Wiederaufarbeitungsanlage Karlsruhe - Karlsruhe Reprocessing Plant